Modeling the formation, evolution, and observation of first stars

Mihir Sanjay Kulkarni

Submitted in partial fulfillment of the
requirements for the degree of
Doctor of Philosophy
under the Executive Committee
of the Graduate School of Arts and Sciences

COLUMBIA UNIVERSITY

2021

Abstract

Modeling the formation, evolution, and observation of first stars

Mihir Sanjay Kulkarni

Population III (Pop III) stars are the first generation stars forming after the big bang from primordial gas. This dissertation is focused on the various processes that suppress and delay the formation of Pop III stars in the universe and their implications for the observations. We studied the impacts of the Lyman-Werner (LW) radiation that dissociates molecular hydrogen, baryon-dark matter streaming velocity introduced at recombination, ionizing radiation from nearby galaxies, and a model for the composition of dark matter known as the fuzzy dark matter on the formation of Pop III stars.

Firstly, we take a closer look at the critical halo mass ($M_{\rm crit}$) that is the typical minimum dark matter halo mass needed to host cold dense gas to form the first stars using cosmological hydrodynamical simulations. LW radiation that dissociates molecular hydrogen and the baryon-dark matter streaming velocity both delay the formation of Pop III stars by increasing the critical halo mass. We describe our simulation suite with varying levels of LW radiation and streaming velocity to provide a fit for $M_{\rm crit}$ as a function of LW radiation, streaming velocity, and redshift which can be used in semi-analytic models of early galaxy formation to make predictions for observations.

Secondly, we explore a possible mechanism for the formation of large clusters of Pop III stars: a nearby ionizing source that ionizes a late forming halo, delaying its collapse until the halo is sufficiently large enough that the core can self-shield and suffer runaway collapse.

We use numerical simulations to examine the fragmentation of the gas near the runaway collapse using the simple estimates and sink particles to show that the number of fragments is generally small, at most a handful, and that the mass accretion rate on the fragments is of order $10^{-3}\,\mathrm{M_\odot yr^{-1}}$. This rate is sufficiently high enough that the descent on the main sequence (and hence the suppression of accretion) is delayed until the stellar masses are of order 100-1000 $\mathrm{M_\odot}$, but not high enough to produce direct collapse black holes of mass $\sim 10^5\,\mathrm{M_\odot}$. The resulting clusters are larger than those produced in minihalos but are still likely to fall short of being easily detectable in *James Webb Space Telescope* blind fields.

Finally, we investigate the formation of the first stars and galaxies in a fuzzy dark matter cosmology. Fuzzy dark matter, made up of ultra-light axions of mass $\sim 10^{-22}\,\mathrm{eV}$, is a proposed alternative to the standard cold dark matter to solve its apparent small-scale problems. Its large de Broglie wavelength, of the order of kpc, results in the suppression of small-scale matter power, thus delaying the formation of the first stars and galaxies to lower redshift in much more massive halos. Therefore, first stars can be used to put very strong constraints on the mass of the fuzzy dark matter. We describe our cosmological simulations that accurately evolve the fuzzy dark matter distribution to study the formation of the first stars and galaxies.

Table of Contents

List of Tables

List of Figures

Acknowledgements

The past six years in my life have been a truly transformative experience, both academically and personally, and I am thankful to everyone who has been a part of it. First and foremost, I would like to thank my advisor Greg Bryan for the wonderful opportunity to work with him on a fascinating topic. His constant encouragement, support, willingness to discuss anything from the fundamental questions to the bugs in my code has made it a wonderful experience to work with him. Thank you to my collaborator Eli Visbal for his constant support and encouragement. Thank you to my committee members Zoltán Haiman and David Schiminovich for their regular feedback and useful comments. I would also like to thank Jeremiah Ostriker for advising me for my first-year project and introducing me to many fascinating ideas including the fuzzy dark matter. Thanks to Mildred Garcia-Kramer and Ayoune Payne for making the administrative tasks a breeze.

I am thankful to the Columbia astronomy grad students for providing a friendly, joyful, and entertaining community that made me feel included. Thanks to Matthew Abruzzo, Jorge Cortés, Rose Gibson, Alex Teachey, Kirsten Blancato, Alejandro Núñez, Julia Blue Bird for the fun times. Thanks to my officemates over the years José Manuel Zorrilla Matilla, Maria Charisi, Aleksey Generozov, Emily Sandford, Sarah Pearson, Tomer Yavetz, Shifra Mandel for the lively discussions and arguments in the office about anything under the sun. Special thanks to José for his mentorship, guidance, and his willingness to indulge my questions and arguments. Thank you to Adam Wheeler for our endless discussions about philosophy, politics, linguistics, geography while enjoying the long walks in the city. Thanks to Nicole

Melso and Stephanie Brim, along with Adam for including me in the family and keeping me sane during an otherwise lonely time with the COVID-19 pandemic. Thank you to Daniel Defelippis for being a fantastic roommate and for all the time spent watching movies, concerts, and quizzes together. Thank you Sai Swaroop Sunku, Anthony Fort, and Trevor Brabyn for the enjoyable time in the city.

Moving from India to a country on the other side of the world for Ph.D. was a big decision for me. My time here was made easier by my friends from IISER who were also in the same boat, my family away from home. Special thanks to Abhijith Gandrakota, Krishna Anujan, Motlakunta Sainath, Neha Bora, Nishad Mandlik, Prathamesh Tamhane, Shiva Chidambaram, Sree Vani Jarugula, Utkarsh Giri, and Viraj Doddihal for visiting me in New York, hosting me in your homes, and providing a sense of familiarity in the foreign world at uncertain times.

I would like to thank all of my teachers throughout school and college, who encouraged me to ask questions and to study physics and astronomy. Thank you to Niruj Mohan Ramanujam, my first advisor on an astronomy project, and Tirthankar Roy Choudhury, my Master's thesis advisor, for introducing me to astronomy research and for supporting me to pursue a Ph.D. in astronomy.

Thank you to Marcel Agüeros, Summer Ash, Jana Grcevich, Carl Anthony Finney, and everyone else involved in the Columbia astronomy outreach events and the Rooftop Variables group for a wonderful time.

I owe a great deal to my family. Thank you to Sunilmama, Anumawshi, Saritamawshi, Vishakhamawshi, Mami, Kaka, Kaku, Ajji for their constant encouragement. Thank you to my sister Manasi and my mother Sharayu for their support and love, without which this would not have been possible. Finally, I am thankful to my late father Sanjay for everything.

Chapter 1: Introduction

1.1 Motivation

Over the years, a standard model of cosmology has evolved based on the observations of the expanding universe and the cosmic microwave background radiation. In this standard model of cosmology, the universe started with a hot big bang about 13.7 Gyr ago. As the universe cooled down because of its expansion, it led to the formation of protons and neutrons, nuclei, and atoms. Before the formation of neutral atoms in an event known as "recombination", approximately 400,000 years after the big bang, baryons were coupled with radiation through Thomson scattering. As neutral atoms formed, the matter and radiation decoupled from each other, leaving out the radiation which we receive today as the cosmic microwave background radiation, also known as the big bang afterglow (Dodelson, 2003).

The epoch of recombination started an era known as the cosmic dark ages. During this period, the density perturbations in the universe continued to grow under the influence of gravity. After a few million years, when the gas in dark matter "minihalos" was able to cool and collapse to higher densities, the first stars in the universe formed (Haiman et al., 1996; Tegmark et al., 1997; Abel et al., 2002). The first stars started emitting radiation and started the cosmic dawn in the universe. They also started emitting radiation which started ionizing the neutral gas around them. With the formation of more stars and galaxies, this process eventually led to the reionization of the intergalactic medium. The first stars had primordial chemistry and were made up of hydrogen (75%) and helium (25%), with traces of lithium. Depending on their mass, some of them exploded as supernovae and started the metal enrichment in the universe. The first stars from primordial gas are typically called Population III (Pop III) stars, whereas metal-enriched stars in the early universe are called

Population II (Pop II) stars.

Studying the properties of the first stars is important for several reasons. First and foremost, they represent the beginning of the collapsed baryonic structure formation in the universe. Understanding the properties of the first stars is a gap in our knowledge between the early universe including big bang nucleosynthesis, cosmic microwave background, and the observations of the low-redshift universe with metal-enriched gas, stars, and galaxies. The properties of the first stars such as their stellar masses, effects of the radiative feedback processes, supernovae explosions, the growth of the metal-enriched regions all significantly impact the properties of the subsequent generations of star formation and in turn affect the properties of the first galaxies in the universe (Bromm & Yoshida, 2011; Loeb & Furlanetto, 2013). The elemental abundances in the extremely metal-poor stars in the galactic halo and the satellite dwarf galaxies can be used to infer the properties of Pop III stars responsible for the metal enrichment (Frebel & Norris, 2015). The signatures of the first stars are predicted to be imprinted in the fluctuations of H I 21-cm signal at high redshift (Fialkov et al., 2013). With upcoming observations of high-redshift galaxies using telescopes like the *James Webb Space Telescope*, as well as H I 21-cm surveys, it is crucially important to have theoretical models to understand the properties of the first stars and their formation channels.

When and where first stars form also depends significantly on the models of cosmology and thus can be used as a test for cosmology. In particular, it strongly depends on the nature of the dark matter particle. Alternative models for the standard cold dark matter such as the warm dark matter and the fuzzy dark matter have structure formation at small scales suppressed (Bode et al., 2001; Schneider et al., 2013; Hu et al., 2000; Marsh, 2016; Hui et al., 2017). Pop III stars form at much lower redshifts and in much more massive halos in these cosmologies. Therefore, predictive models of the first stars can be used to distinguish these models from the standard cold dark matter. In particular, we focus on the properties of first stars in the fuzzy dark matter cosmology in Chapter 4. Fuzzy dark matter is proposed to be made up of ultra-light axions that have a mass of the order of 10^{-22} eV. This results in

a de Broglie wavelength of astrophysical (∼kpc) scale and results in a quantum pressure for dark matter. We study the properties of first stars in fuzzy dark matter cosmology with an accurate treatment for the evolution of fuzzy dark matter structure.

The formation of Pop III stars is also a relatively simple theoretical problem. In the absence of metals, and the presence of mainly hydrogen and helium, we can explore various formation scenarios in much more detail while making a minimum number of assumptions. Because of this relative simplicity of the problem, it is also easier to provide analytical models to explain our results from the numerical simulations, as we attempt to do in subsequent chapters.

In this thesis, we studied various processes that delay the formation of Pop III stars, given the possibility of their direct or indirect detection with the upcoming observing facilities. In particular, we studied the delay in the formation of Pop III stars caused by the Lyman-Werner radiation that dissociates molecular hydrogen, the streaming velocity between baryon and dark matter, the ionizing radiation, and the presence of fuzzy dark matter as the primary candidate of dark matter. We studied if and how these processes affect the possibility of direct or indirect detection of Pop III stars with upcoming observing facilities. In Section 1.2, we describe some preliminary properties of Pop III stars about the gas cooling needed for their formation, properties of dark matter halos they form in, and their end states. In Section 1.3, we describe some of the observational signatures and prospects for the detection of Pop III stars that motivate the work in this thesis. In Section 1.4, we describe some of the previous simulations and their results to set a background for the numerical simulations performed in this thesis. Finally, in Section 1.5, we provide an outline of the structure of this thesis and the work performed in it.

1.2 Preliminary properties of Pop III stars

1.2.1 Gas cooling

Primordial gas formed in the big-bang nucleosynthesis consists of isotopes of hydrogen, helium, and lithium. In the absence of metals, cooling primarily occurs through hydrogen and its isotopes. For atomic hydrogen and helium, the cooling curve peaks near $10^4\,\mathrm{K}$ with the Lyman-α transition and drops sharply at lower temperatures. If molecular hydrogen is formed, it can get excited to its rotational and vibrational transitions and cool down to a temperature of $\sim 200\,\mathrm{K}$ via radiative cooling (Loeb & Furlanetto, 2013). Figure 1.1 shows a cooling function as a function of temperature in the presence of molecular hydrogen. Molecular hydrogen cooling is necessary to form Pop III stars in halos that are below the atomic cooling threshold ($T_{\mathrm{vir}} < 10^4\,\mathrm{K}$).

The dominant mechanism to form molecular hydrogen is through H^- formation as

$$\mathrm{H} + \mathrm{e}^- \longrightarrow \mathrm{H}^- + \gamma, \tag{1.1}$$

$$\mathrm{H} + \mathrm{H}^- \longrightarrow \mathrm{H}_2 + \mathrm{e}^-. \tag{1.2}$$

The protostellar core cools at the temperature $\sim 200\,\mathrm{K}$ until it gets denser than $n_{\mathrm{H}} > 10^8\,\mathrm{cm}^{-3}$. At this point, further molecular hydrogen can be formed via three-body formation channel as

$$\mathrm{H} + \mathrm{H} + \mathrm{H} \longrightarrow \mathrm{H}_2 + \mathrm{H}, \tag{1.3}$$

$$\mathrm{H} + \mathrm{H} + \mathrm{H}_2 \longrightarrow \mathrm{H}_2 + \mathrm{H}_2. \tag{1.4}$$

Molecular hydrogen can be dissociated by Lyman-Werner photons with energy $11.2 - 13.6\,\mathrm{eV}$. This happens with a two-step dissociation process known as the Solomon process

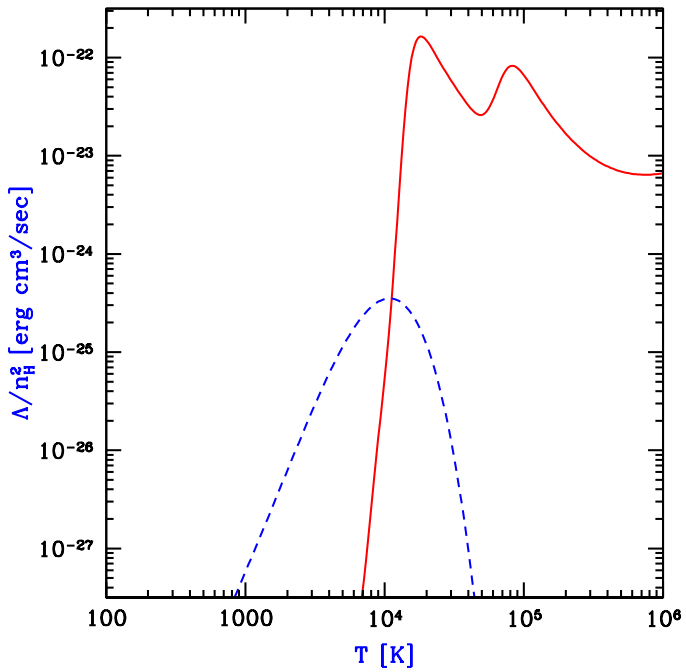

Figure 1.1: Cooling rate for the primordial gas made up of atomic hydrogen and helium, and molecular hydrogen as a function of temperature. It assumes an atomic hydrogen density $n_H = 0.045\,\mathrm{cm}^{-3}$ with the molecular hydrogen fraction of 10^{-3}. The solid red curve represents cooling from atomic gas, with peaks representing collisional excitation of H I and He I. The dashed blue curve represents cooling because of molecular hydrogen which extends to much lower temperatures. Reprinted from Figure 12 of Barkana & Loeb (2001).

as

$$H_2 + \gamma \longrightarrow H_2^* \longrightarrow 2\,H. \tag{1.5}$$

The fragmentation scale of the gas and in turn the typically expected mass of the stars primarily depends on the temperature of the gas. The simplest formulation of this phenomenon is the Jeans instability. A gas cloud is Jeans unstable if its sound crossing time is larger than the free-fall time. If the sound-crossing time is shorter than the free-fall time, the gas densities can redistribute because of the pressure waves to avoid gas collapse. The timescales are given as

$$t_s = \frac{R}{c_s} = R\sqrt{\frac{m}{\gamma k_B T}}, \quad t_{\rm ff} = \frac{1}{\sqrt{G\rho}}, \tag{1.6}$$

where R is the radius of the cloud, c_s is the speed of sound, T is the gas temperature, and ρ is the gas density. We can define the Jeans length and consequently the Jeans mass by equating these two timescales. The Jeans mass is the typical fragmentation scale and depends on the temperature and density of the gas and is given as

$$M_{\rm J} \approx 700 \left(\frac{T}{200\,{\rm K}}\right)^{3/2} \left(\frac{n_{\rm H}}{10^4\,{\rm cm}^{-3}}\right)^{-1/2} {\rm M}_\odot \tag{1.7}$$

(Loeb & Furlanetto, 2013). Therefore, the fragmentation scale and the typical Pop III stellar mass depends on the gas cooling properties. The atomic cooling halos ($T_{\rm vir} \sim 10^4\,{\rm K}$) that have molecular hydrogen in them dissociated completely can only cool to the temperature of $10^4\,{\rm K}$ via atomic cooling and can lead to the formation of supermassive star of mass $10^5\,{\rm M}_\odot$ acting as a massive seed for the formation of the supermassive black holes (Inayoshi et al., 2020).

1.2.2 Relation to halo mass

In ΛCDM, first stars are expected to form in minihalos of mass $10^5 - 10^7 M_\odot$. This minimum halo mass for formation of Pop III stars can be understood using the following analytic argument (Haiman et al., 1996; Tegmark et al., 1997; Machacek et al., 2001; Trenti

& Stiavelli, 2009). In a halo with pristine gas, the gas will cool and collapse to form first stars when its cooling time is shorter than the Hubble time ($t_{\rm cool} < t_{\rm H}$). The Hubble time approximately represents the age of the universe at a given redshift and is also closely related to the dynamical time of the halo. The cooling time, $t_{\rm cool}$ can be written as

$$t_{\rm cool} = \frac{u}{\dot{u}_{\rm cool}} = \frac{1.5 n k_{\rm B} T_{\rm gas}}{\Lambda(T_{\rm gas}) n_{\rm H} n_{\rm H_2}}, \tag{1.8}$$

where n is the gas number density, $k_{\rm B}$ is the Boltzmann constant, $T_{\rm gas}$ is the gas temperature, which can be assumed to be the virial temperature of the halo, Λ is the cooling function, $n_{\rm H}$ is the hydrongen number density, $n_{\rm H_2}$ is the number density of molecular hydrogen. We can express n, $n_{\rm H_2}$, and $T_{\rm gas}$ as a function of $M_{\rm vir}$, and z. We can equate the cooling time as a function of the virial mass of the halo and redshift with the Hubble time, given as

$$t_{\rm H} = \frac{1}{H(z)} = \frac{1}{H_0 \sqrt{\Omega_\gamma (1+z)^{-4} + \Omega_m (1+z)^{-3} + \Omega_\Lambda}} \tag{1.9}$$

for a flat ΛCDM universe. This process results in a minimum halo mass of a few times $10^5\,{\rm M}_\odot$ for the formation of the first stars in them. We provide a detailed account of this calculation in Section 2.4.2.

In the presence of Lyman-Werner radiation, molecular hydrogen is dissociated and thus the gas collapse is delayed to later times in more massive halos. For very strong LW radiation, most of the molecular hydrogen is dissociated and star formation is suppressed until the halo becomes atomic cooling ($T_{\rm vir} \sim 10^4\,{\rm K}$). For halos exposed to strong ionizing radiation, the gas collapse can be delayed even further than the atomic cooling threshold leading to gas collapse when the gas can self-shield itself from the ionizing radiation. Such halos would form a cluster of Pop III stars at lower redshifts and thus would be more likely to be detected with upcoming telescopes.

1.2.3 Fate of Pop III stars

The lifetime and the end states of Pop III stars depend on their stellar mass. The stars of mass $10 - 40\,M_\odot$ can undergo Type II supernovae and would be responsible for the enrichment of heavy elements in the nearby universe. For the stellar mass in the range of $130 - 250\,M_\odot$, stars are likely to explode as pair-instability supernovae (PISN) (Loeb & Furlanetto, 2013). Here, the thermal energy in the core is used to generate electron-positron pairs, which leads to a pressure drop leading to partial collapse and accelerated burning in a runaway thermonuclear explosion, which blows up the star without leaving a remnant. The pair-instability supernovae are expected to be very bright and have been suggested as a way to detect the signatures of Pop III stars (Whalen et al., 2013; Hartwig et al., 2018b). For the other mass ranges, stars generally collapse to form a black hole without an explosion. The growth of black holes from Pop III stars has been suggested as a pathway to form the high redshift supermassive black holes.

1.3 Obervational overview

Based on their masses, Pop III stars can explode as core-collapse supernovae or as pair-instability supernovae (PISN). By modeling the supernovae explosions, we can estimate the abundances of various elements in the supernovae explosions. When the next generation of stars forms in the metal-enriched gas, their elemental abundances can be used to infer the properties of stars that formed before them. In recent years, observations of extremely metal-poor stars have been used to constrain properties of the first stars (Frebel & Norris, 2015). The elemental abundances of the extremely metal-poor stars are reported to be predominantly best fit with the supernovae yields from stars of mass $M < 40\,M_\odot$ (Tumlinson et al., 2004; Ishigaki et al., 2018).

The *James Webb Space Telescope (JWST)* is an infrared space telescope to be launched in 2021. Because of its large area and low noise, its deep field observations are predicted to

detect the signatures of first stars. The pair-instability supernovae (PISN) from massive Pop III stars are expected to be detected by *JWST* (Whalen et al., 2013; Hartwig et al., 2018b). Massive Pop III star clusters ($M_* \sim 10^5\,\mathrm{M}_\odot$) can be detected with *JWST* using photometry (Zackrisson et al., 2011). Caustic transits behind lensing clusters for Pop III stars have been suggested as a way to detect them directly with the *JWST* (Windhorst et al., 2018).

The cosmological 21-cm signal from the hyperfine transition of neutral hydrogen is an important probe for the signatures of first stars. The first stars and galaxies start emitting Lyman-α photons that indirectly couple the spin temperature of the 21-cm line with the kinetic temperature of the gas through the effect known as Wouthuysen-Field effect, after Wouthuysen (1952) and Field (1958). With the kinetic temperature of the gas being smaller than the cosmic microwave background radiation, we should observe an absorption at the wavelength of $21/(1+z)$ cm (Barkana & Loeb, 2005; Hirata, 2006). The large-scale spatial fluctuations of the 21-cm signal would have imprints of the inhomogeneous density field and the Lyman-α and X-ray radiative sources. Detection of the power spectrum of 21-cm signal with the *Square Kilometer Array (SKA)* and the *Hydrogen Epoch of Reionization Array (HERA)* can be used to put very strong constraints on the properties of first stars (Fialkov et al., 2013, 2014).

The recent merger event GW190521 observed by the *Laser Interferometer Gravitational-wave Observatory (LIGO)* had two inspiraling black holes of masses 85 and $66\,\mathrm{M}_\odot$ resulting in a black hole remnant of mass $142\,\mathrm{M}_\odot$. These black holes fall in the theoretical forbidden mass range ($55 - 130\,\mathrm{M}_\odot$) predicted by the standard pulsational pair-instability supernova models and have been proposed to have formed from the massive Pop III star remnants (Safarzadeh & Haiman, 2020; Kinugawa et al., 2020; Liu & Bromm, 2020). This creates a new way of detecting the observational signatures of Pop III stars, particularly those forming in Pop III clusters.

1.4 Simulations overview

The first simulations of the formation of first stars with cosmological context became possible near the turn of the century with the use of novel techniques such as adaptive mesh refinement (AMR) and smooth particle hydrodynamics (SPH). A crucial breakthrough in the field was the simulations performed by Abel et al. (2002). Abel et al. (2002) followed the runaway collapse of gas in a halo of mass $10^6\,\mathrm{M}_\odot$ in a cosmological simulation using AMR and followed it to densities as high as $10^9\,\mathrm{cm}^{-3}$ and concluded that the central dense core does not fragment and only forms a single star ($M >> 1\,\mathrm{M}_\odot$) in the halo.

Many numerical simulations with high resolution have studied the fragmentation of the primordial gas cloud suggesting that the minihalos form multiple star systems instead of single star systems (Stacy et al., 2010; Clark et al., 2011; Greif et al., 2011b, 2012). The fragmentation and the initial mass function (IMF) of the first stars depend on the turbulence (Wollenberg et al., 2020), as well as on the magnetic fields (Sharda et al., 2020).

Machacek et al. (2001) studied the statistical sample of dark matter halos in a cosmological simulation and identified a threshold halo mass, also known as the critical halo mass, above which the halos contain cold and dense gas ($T < 0.5T_{\mathrm{vir}}$ and $n > 330\,\mathrm{cm}^{-3}$) that can lead to the formation of first stars. It is particularly important to study Pop III star formation in halos with different properties and evolution histories, as opposed to the most massive halo in the simulation like Abel et al. (2002). Machacek et al. (2001) also included two cases with Lyman-Werner background radiation that dissociates molecular hydrogen ($F_{\mathrm{LW}} = 10^{-22}\,\mathrm{ergs}^{-1}\mathrm{cm}^{-2}\mathrm{Hz}^{-1}$ and $F_{\mathrm{LW}} = 10^{-21}\,\mathrm{ergs}^{-1}\mathrm{cm}^{-2}\mathrm{Hz}^{-1}$). Using these results, Machacek et al. (2001) provided a fitting formula for M_{crit} as a function of LW background as

$$M_{\mathrm{TH}}(M_\odot) = 2.5 \times 10^5 + 8.7 \times 10^5 \left(\frac{F_{\mathrm{LW}}}{10^{-21}}\right)^{0.47}. \tag{1.10}$$

This work did not include the self-shielding of molecular hydrogen and also did not have sufficiently large samples to probe the redshift evolution of M_{TH}. Machacek et al. (2001)

divided the halos in two bins $z > 22$ and $z < 22$, and did not find a statistically significant difference in the constrained threshold mass, although the redshift-evolution of $M_{\rm crit}$ has been predicted in many analytic models. Accurately identifying $M_{\rm crit}$ allows us to connect the underlying dark matter halo distribution with the sites of Pop III star formation. This is particularly useful for semi-analytic models of early galaxy formation that use dark matter only simulations, where dark matter halos can be populated with Pop III stars based on the halo mass and the threshold mass for the given LW radiation. The effect of LW radiation on Pop III stars has been explored in many subsequent works (e.g., O'Shea & Norman, 2007; Wise & Abel, 2007).

Tseliakhovich & Hirata (2010) pointed out that there is a net supersonic streaming velocity between baryons and dark matter arising from a quadratic term in the cosmological perturbation theory equations. This arises from the fact that prior to recombination, baryons were coupled with radiation, whereas dark matter substructure was not and was already growing under the influence of gravity. This results in a net streaming velocity between the two which varies over the scale of the baryon acoustic oscillations ($\sim 100\,$Mpc comoving). At the recombination, root-mean-squared streaming velocity is $30\,$km/s, and remains coherent over Silk damping scale (several comoving Mpc) (Tseliakhovich & Hirata, 2010). This streaming velocity decreases with time as $\propto (1+z)$, therefore its effects are particularly important to high-redshift phenomena such as the formation of Pop III stars. In the regions with high streaming velocity, Pop III stars can form only in massive halos with deeper potential wells to overcome the net streaming between baryons and dark matter. Numerical simulations of Pop III formation in presence of streaming have been done by Greif et al. (2011a); Stacy et al. (2012); Schauer et al. (2019).

1.5 Thesis outline

With the possibility of direct or indirect detection of Pop III stars with the upcoming observing facilities including the *James Webb Space Telescope*, it is very important to study

various processes that delay the formation of Pop III stars leading to the formation of massive Pop III star clusters at lower redshift. In this thesis, we explore the effects of the Lyman-Werner radiation that dissociates molecular hydrogen, baryon-dark matter streaming velocity, strong ionizing radiation from nearby galaxies, and the nature of the dark matter - specifically the presence of fuzzy dark matter. We report the results of these processes on the formation of Pop III stars in different chapters as described below.

In Chapter 2, we study the impact of Lyman-Werner radiation and baryon-dark matter streaming velocity on the formation of Pop III stars. It had been nearly two decades since the publication of Machacek et al. (2001) and many aspects have improved since then such as increased computing power, modified reaction rates (Glover, 2015a,b), as well as available prescriptions for self-shielding from LW radiation (Wolcott-Green et al., 2011; Wolcott-Green & Haiman, 2019). In the past, the impacts of LW radiation and streaming velocity on $M_{\rm crit}$ were studied separately and assumed to be independent of each other. We performed cosmological simulations with various cases of LW background radiation and streaming velocity, identified a redshift dependent $M_{\rm crit}$, and provided an updated fit for its dependence on LW background and streaming velocity.

In Chapter 3, we explore a scenario of delayed Pop III galaxy formation. We considered a scenario where a dark matter halo with pristine gas has been exposed to strong ionizing radiation that ionizes neutral hydrogen. This suppresses the star formation in the absence of any cooling agent until the gas can self-shield itself from the ionizing radiation, undergoing a runway collapse to form a cluster of Pop III stars in a much more massive halo at low redshift. These would be some of the most massive structures made up of Pop III stars and thus more likely to be detected directly in emission. We studied how the runway gas collapse depends on the ionizing background radiation and the fragmentation processes in gas during the runaway collapse. We estimated the total stellar masses in Pop III stars in these clusters to be as high as a few times $10^3\,{\rm M}_\odot$ and concluded that direct detection of these Pop III galaxies would be unlikely in the blind fields with the *James Webb Space Telescope*.

In Chapter 4, we studied the formation of first stars in a fuzzy dark matter cosmology. The fuzzy dark matter, made up of ultra-light axions ($m \sim 10^{-22}\,\mathrm{eV}$), has been proposed as an alternative to the standard cold dark matter. It has a de Broglie length of the order of kpc which results in suppression of small-scale structure and results in a low-mass cut-off in the halo mass function. Thus, in a fuzzy dark matter cosmology, the formation of first stars would happen in massive halos ($M > 10^9\,\mathrm{M}_\odot$) at lower redshifts and can be used to put very strong constraints on the mass of fuzzy dark matter. In Chapter 4, we perform cosmological hydrodynamical simulations that accurately evolve the fuzzy dark matter distribution to study the properties of the first stars and galaxies in it. We found that the first stars form in the central region of the most massive halo in our simulation at $z = 10$.

We then conclude by summarizing our results from previous chapters and providing a few thoughts about the future directions.

Chapter 2: The critical dark matter halo mass for Population III star formation: dependence on Lyman-Werner radiation, baryon-dark matter streaming velocity, and redshift

2.1 Introduction

Population III (Pop III) stars, defined by their extremely low metallicities, are the first generation of stars to form after the big bang. In the context of the standard model of cosmology (ΛCDM), numerical simulations predict that the first Pop III stars formed in pristine dark matter "minihalos" with masses of $10^5 - 10^6 M_\odot$ (Haiman et al., 1996; Tegmark et al., 1997; Machacek et al., 2001; Abel et al., 2002; Bromm et al., 2002; Yoshida et al., 2003; Bromm et al., 2009; Bromm & Yoshida, 2011; Greif, 2015). Understanding when and where Pop III stars form is important given their role in early metal enrichment and the first stages of galaxy evolution. Observations of Pop III stars also have the potential to shed light on the particle nature of dark matter, since the abundance of minihalos is strongly reduced in certain models such as warm dark matter or fuzzy dark matter (O'Shea & Norman, 2006; Magg et al., 2016; Sullivan et al., 2018; Mocz et al., 2019).

A number of upcoming observations have the potential to either directly detect Pop III stars or constrain their properties indirectly (Rydberg et al., 2013; Windhorst et al., 2018). Halos where Pop III star formation is suppressed at early times because of strong UV radiation can form Pop III clusters that can be detected if they are gravitationally lensed by foreground galaxy clusters (Johnson, 2010; Visbal et al., 2016; Kulkarni et al., 2019). Pop

This section contains text from an article accepted for publication in the Astrophysical Journal (Kulkarni et al., 2020).

III stars in the mass range $140 - 250\,M_\odot$ may explode as pair-instability supernovae (PISN) which may be detected with the *James Webb Space Telescope (JWST)* (de Souza et al., 2013, 2014; Whalen et al., 2013; Hartwig et al., 2018b). Remnants of Pop III stars and extremely metal-poor stars can be studied using galactic archaeology to infer properties of Pop III stars and can be complemented by observations of high-redshift galaxies using upcoming thirty meter class telescopes such as the *Extremely Large Telescope (ELT)* and the *Thirty Meter Telescope (TMT)* (Joggerst et al., 2010; Frebel & Norris, 2015; Chen et al., 2017; Ishigaki et al., 2018; Hartwig et al., 2018a). Additionally, the 21-cm signal from cosmological neutral hydrogen as well as line intensity mapping of He II 1640 Å can be used to constrain the properties of Pop III stars (Fialkov et al., 2013; Visbal et al., 2015).

Detailed theoretical predictions are required to maximize the scientific return of these various observational probes of the first stars. Semi-analytic models of Pop III star formation provide a computationally inexpensive method to predict when and where they form (e.g., Magg et al., 2018; Visbal et al., 2018, 2020). These semi-analytic models start with dark matter halo merger trees generated with cosmological N-body simulations or Monte Carlo methods based on the extended Press-Schechter formalism. Star formation is then followed in these halos with analytic prescriptions. One of the most crucial parameters in semi-analytic models of the first stars is the minimum dark matter halo mass required for Pop III stars formation, $M_{\rm crit}$. To make accurate observational predictions with semi-analytical models, it is important to understand how $M_{\rm crit}$ evolves with various environmental effects.

$M_{\rm crit}$ corresponds to the typical halo mass where sufficient cold and dense gas is present to cause runaway collapse and star formation. The cooling of gas in pristine minihalos happens primarily through roto-vibrational transition lines of molecular hydrogen. As Pop III (and Pop II) stars form, they emit Lyman-Werner (LW) photons with energy in the $11.2 - 13.6$ eV range that can dissociate molecular hydrogen. The LW photon fractions from minihalos can be as high as 85% (Schauer et al., 2015, 2017). As the cosmic star formation rate density (SFRD) increases, a corresponding background of LW radiation builds

up. Halos in a region with a high LW background have their molecular hydrogen destroyed and are unable to cool efficiently. In such regions, the minimum critical halo mass required for cooling is increased (Haiman et al., 1996; Tegmark et al., 1997; Machacek et al., 2001; O'Shea & Norman, 2007; Wise & Abel, 2007). This effect of the LW background on $M_{\rm crit}$ was first studied in hydrodynamical cosmological simulations with a statistical sample of halos in Machacek et al. (2001). The minimum LW background radiation required to suppress the Pop III star formation in low-mass minihalos without a streaming velocity has been considered in a number of previous studies (Dijkstra et al., 2008; Yue et al., 2014; Latif et al., 2014; Agarwal et al., 2016).

The critical mass for halos also depends on a phenomenon known as the baryon-dark matter streaming velocity, which was first pointed out by Tseliakhovich & Hirata (2010). Prior to cosmic recombination, baryons were coupled to radiation via Thompson scattering, whereas the dark matter and radiation were uncoupled. This creates a relative velocity between baryons and dark matter involving a quadratic term in the cosmological perturbation theory (Tseliakhovich & Hirata, 2010). The streaming velocity is coherent over several comoving Mpc and follows a Maxwell-Boltzmann distribution with an RMS velocity of ~ 30 km/s at recombination. It decreases with time as $\propto (1+z)$. In the regions with high streaming velocities, dark matter halos need to be more massive with deeper potentials for gas to cool and form stars, which results in an increase of the critical mass (Greif et al., 2012; Stacy et al., 2012; Fialkov, 2014; Schauer et al., 2019).

Apart from its dependence on LW radiation and baryon-dark matter streaming, many analytic models predict a redshift dependence for $M_{\rm crit}$, such that it increases with decreasing redshift (Tegmark et al., 1997; Haiman et al., 2000; Trenti & Stiavelli, 2009), or assume a redshift dependence corresponding to a fixed virial temperature (Visbal et al., 2014b). Previous numerical works that estimate the critical mass using a statistical sample of halos have not seen a redshift evolution of $M_{\rm crit}$ or see a constant $M_{\rm crit}$ as a function of redshift. (Machacek et al., 2001; Schauer et al., 2019).

It has been nearly two decades since the publication of Machacek et al. (2001). Many things have improved since then such as increased computing power, modified reaction rates, as well as available prescriptions for self-shielding from LW radiation (Wolcott-Green et al., 2011; Wolcott-Green & Haiman, 2019). In the past, the impacts of LW radiation and streaming velocity on $M_{\rm crit}$ have been studied separately (although see Schauer et al., 2020) and the increase in $M_{\rm crit}$ when both effects are present has been assumed to be independent of each other and to be multiplicative (Fialkov et al., 2013; Visbal et al., 2020). With the improvement in computational capabilities, we aim to study the combined effects of LW radiation, dark matter baryons streaming and redshift on $M_{\rm crit}$ and provide an analytic fitting function that can be then used by semi-analytic models to make observational predictions.

This chapter is structured as follows. In Section 2.2, we describe our simulation setup, details on the self-shielding prescriptions used, criteria used for calculating $M_{\rm crit}$, and the parameter space probed in this work. In Section 2.3, we present our results about $M_{\rm crit}$ and its dependence on LW radiation, streaming velocity, and redshift. In Section 2.4, we provide a fit for $M_{\rm crit}(J_{\rm LW}, v_{\rm bc}, z)$ and discuss how our results compare with previous works. We summarize our main conclusions in Section 2.5.

2.2 Methodology

2.2.1 Simulation setup

We perform cosmological simulations using the adaptive mesh refinement (AMR) code ENZO (Bryan et al., 2014; Brummel-Smith et al., 2019). We use the energy conserving, spatially third-order accurate Piecewise Parabolic Method (PPM) for the hydro solver in all of our runs. ENZO follows the non-equilibrium evolution of nine species (H, H^+, He, He^+, He^{++}, e^-, H_2, H_2^+ and H^-) and includes radiative processes. We included a uniform LW background radiation with an updated self-shielding prescription based on Wolcott-Green & Haiman (2019). We updated the reaction rates in ENZO with Glover (2015a,b).

For all of our cosmological simulations, we assume a cosmology based on recent Planck

observations (Planck Collaboration et al., 2014): $\Omega_m = 0.32$, $\Omega_\Lambda = 0.68$, $\Omega_b = 0.049$, $h = 0.67$ and $n_s = 0.96$. In order to simulate a larger statistical sample of minihalos, we increased the Planck normalization of the matter power spectrum to $\sigma_8 = 1$ (from $\sigma_8 = 0.83$). We discuss this choice in more detail below. We run most of our simulations with a box size of 0.5 h^{-1} Mpc and initial resolution of 512^3 cells and dark matter particles (corresponding to a particle mass of $100\,M_\odot$). We refine cells into smaller cells based on their baryon mass, dark matter mass and Jeans length. We refine the cell if the baryon or dark matter density becomes higher than 4×2^{3l} times the corresponding densities on the root grid (512^3) in the simulation where l is the refinement level, meaning that cells with more mass than 4 times the initial dark matter particle mass or baryon equivalent will be refined. The Jeans length is resolved by at least 4 cells, and generally controls the refinement during the later parts of the baryonic collapse. We allow a maximum of six levels of refinement resulting in a minimum cell size of ~ 1 pc at z = 20. Once the maximum refinement level is reached, an artificial pressure is added to the smallest cells such that the Jeans length is always refined by 8 cells to avoid artificial fragmentation (Truelove et al., 1997; Machacek et al., 2001). We use artificial pressure to follow a statistical sample of halos and to avoid slowing simulations with dense runaway gas collapse. For cases with high LW backgrounds or high streaming velocities, in order to have a sufficient number of massive halos, we run simulations with a larger box size of 1 h^{-1} Mpc with a 512^3 base grid. This corresponds to a dark matter particle mass of $800\,M_\odot$. For these runs we use a maximum 7 AMR levels in order to maintain the same spatial resolution as our other simulations. See Section 2.4 for a further discussion on resolution tests.

We utilized the ROCKSTAR halo finder (Behroozi et al., 2013a) to identify halos and used M_{200c} (the mass enclosed within a sphere of mean density 200 times the critical density) for our definition of the halo mass. We generated the merger trees using CONSISTENT-TREES (Behroozi et al., 2013b) in order to trace the evolution of the halos. The analysis for this work was performed using YT (Turk et al., 2011) and YTREE (Smith & Lang, 2019).

2.2.2 Initial conditions

We generate the initial conditions for our simulations using CICASS (O'Leary & McQuinn, 2012; McQuinn & O'Leary, 2012). A number of previous works have simulated the streaming velocity by simply adding a uniform velocity to the baryon velocity field at the starting redshift (Stacy et al., 2012; Greif et al., 2012; Schauer et al., 2019). As pointed out by O'Leary & McQuinn (2012) and McQuinn & O'Leary (2012), this ignores the evolution of the gas density as a result of the streaming velocity from cosmic recombination to the redshift of the initial conditions. CICASS calculates the effect of streaming self-consistently using perturbation theory and displaces baryons with respect to dark matter particles appropriately in the initial conditions – an effect which was not considered in most previous works.

2.2.3 Criterion for $M_{\rm crit}$

Our aim is to understand when and where Pop III stars form. Following the gas collapse to high densities in halos requires very high resolution and is typically done in zoom-in simulations where a region around the halo of interest has higher resolution to follow the density evolution (O'Shea & Norman, 2007; Kulkarni et al., 2019). In a cosmological simulation suite like this, we cannot follow gas collapse in all halos because of limited computing resources. Hence, we use a criterion to identify halos that have cold and dense gas that would collapse soon and lead to star formation, but do not follow the process of runaway collapse to very high density.

We define a halo to have cold and dense gas if it has at least one cell on the highest refinement level with $T < 0.5T_{\rm vir}$ and $n > 100\,{\rm cm}^{-3}$. We find that most of the cells following this criterion have their cooling time shorter than the Hubble time and hence we expect them to undergo a runaway collapse even though it does not happen in our simulation because of artificial pressure. We then examine the halos in each simulation output (corresponding to a particular choice of LW background, streaming and redshift) and try to determine $M_{\rm crit}$ for

that output. As shown in Machacek et al. (2001), there is a general trend such that more massive halos are more likely to have cold-dense gas; however, this trend is not perfect and so there is no unique way to determine $M_{\rm crit}$. We tried various methods to define this quantity including the fitting function used in Machacek et al. (2001) which also takes into account the total mass of cold dense gas in the halo. However, this method becomes unreliable when the number of halos is small and does not provide a reliable estimate of the uncertainty on the value of $M_{\rm crit}$.

Instead we adopt the following approach, as illustrated in Figure 2.1, to account for the scatter. Figure 2.1 shows the halos with and without cold dense gas for $J_{\rm LW} = 0$ and $v_{\rm bc} = 0$ at $z = 15$. We bin halos into log-spaced mass bins and use the smallest bin size such that the fraction of halos that have cold-dense gas is monotonically increasing in the range of fractions from 0.25 to 0.75. This technique automatically adjusts for the number of halos since the bin sizes are naturally smaller for more halos (resulting in a more precise measurement of $M_{\rm crit}$) and larger for outputs with fewer halos (resulting in a less precise but more robust determination of $M_{\rm crit}$). As can be seen in Figure 2.1, we find a large scatter in halo masses for which a halo has cold-dense gas. We define the critical mass corresponding to the mass bin where half of the halos in that mass bin have cold-dense gas and we use the bin size as the uncertainty (error bar) on $M_{\rm crit}$. When we have fewer halos with cold dense gas at a given redshift, we need to use larger mass bins to satisfy the criterion, resulting in a larger uncertainty. Using slightly different cutoffs for the temperature and density does not change $M_{\rm crit}$ significantly. We also quantify the scatter around $M_{\rm crit}$ in Section 2.3.5.

To increase the number of halos while maintaining a high spatial resolution, we run our simulations with an increased amplitude of density fluctuations (by setting $\sigma_8 = 1$). This change leads to a larger number of star-forming minihalos at earlier redshifts without increasing the simulation box size (which would reduce spatial resolution). This modification enables us to study a large statistical sample of star-forming minihalos without significantly changing the halo properties. We carried out a simulation with the standard σ_8 value and

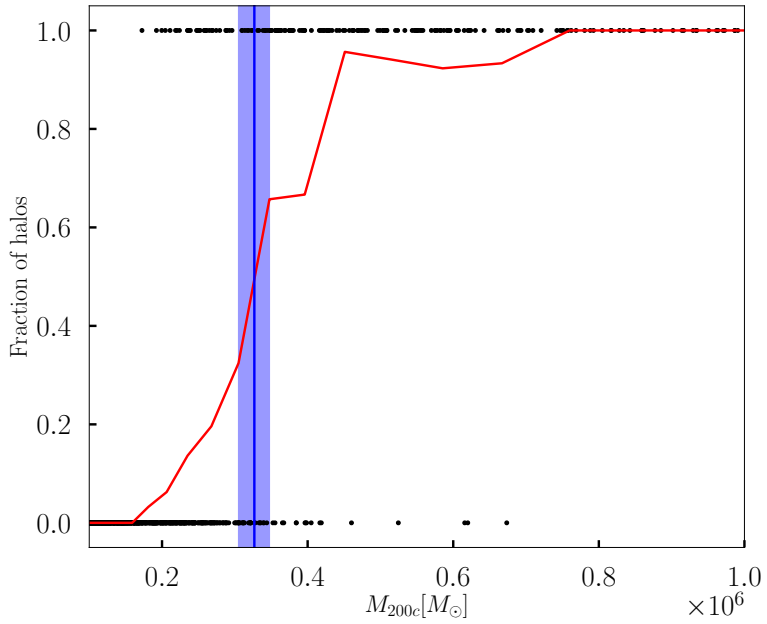

Figure 2.1: The scatter in halos that have cold dense gas. This demonstrates the method we used to identify $M_{\rm crit}$ for halos from a run with $J_{\rm LW} = 0$ and $v_{\rm bc} = 0$ at $z = 15$. The black dots denote individual halos and their position on the x-axis indicates halo masses and the y-axis indicates whether the halos have (1), or do not have (0) cold, dense ($T < 0.5T_{\rm vir}$, $n > 100\,{\rm cm}^{-3}$) gas. The red line shows the fraction of halos with cold-dense gas in each mass bin. The bin size corresponds to the smallest bin that can have a monotonically increasing red curve between $y = 0.25$ and $y = 0.75$. The critical mass corresponds to the mass bin where half of the halos in that bin have cold dense gas (shown in blue) and we use the bin size (shown as the shaded blue region) as an estimate of the uncertainty of this measurement.

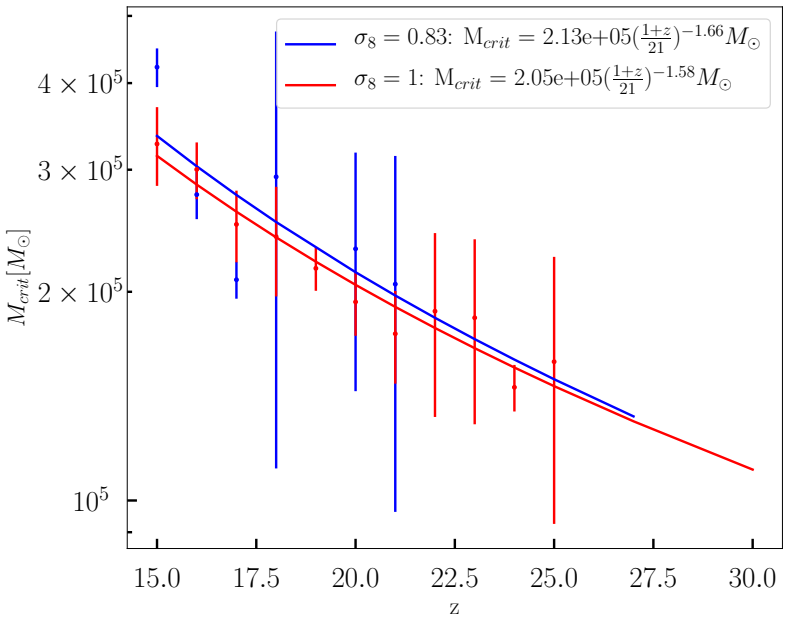

Figure 2.2: $M_{\rm crit}$ as a function of redshift with the default Planck15 σ_8 of 0.83 (blue) and with increased σ_8 of 1 (red). Increased σ_8 increases the number of halos in the simulation, resulting in smaller errors on $M_{\rm crit}$. The trends for $M_{\rm crit}$ look qualitatively similar in both cases and result in estimated $M_{\rm crit}$ and z-dependence parameters within 1σ error of each other, justifying the use of increased σ_8 throughout this chapter.

found that the cooling properties of individual halos closely matched those of the higher initial power spectrum. Figure 2.2 shows $M_{\rm crit}$ as a function of redshift for simulations with the default and increased σ_8. The simulation with increased σ_8 has a higher number of halos ($\sim$ 900 instead of $\sim$ 200 halos above the virial mass of $10^5\,{\rm M}_\odot$ at $z = 15$ in a 0.5 $\rm h^{-1}$ comoving Mpc box). Simulations with the box size of 1 $\rm h^{-1}$ comoving Mpc box have $\sim$ 6000 halos above the virial mass of $10^5\,{\rm M}_\odot$ at $z = 15$. This results in smaller estimated errors on $M_{\rm crit}$. As shown in Figure 2.2, the simulation with increased σ_8 results in $M_{\rm crit}$ and its z-dependence parameters differing by less than 1σ with the default σ_8 simulation.

We seek to characterize the simultaneous dependence of $M_{\rm crit}$ on redshift, LW flux, and magnitude of the baryon-dark matter streaming velocity. We accomplish this by taking simulation snapshots at $z = 30$, 27, 25, 24, 23, 22, 21, 20, 19, 18, 17, 16, and 15 for a number of different runs with various combinations of LW flux and streaming velocity. These include

	$J_{21} = 0$	$J_{21} = 1$	$J_{21} = 10$	$J_{21} = 30$
$v_{\rm bc} = 0$	✓	✓	✓	✓
$v_{\rm bc} = 1\sigma$	✓	✓	✓	
$v_{\rm bc} = 2\sigma$	✓	✓		

Table 2.1: The LW background and dark matter-baryon streaming parameters used in our simulation suite. A check indicates that we ran that combination of parameters.

4 LW backgrounds: 0, 1, 10 and 30, in units of J_{21} where $J_{21} = 10^{-21}\,{\rm erg\,s^{-1}cm^{-2}Hz^{-1}Sr^{-1}}$. LW backgrounds of up to J_{21} are expected to be common, however cases with 10 and 30 J_{21} would correspond to regions with high LW radiation, possibly from a nearby source; these high values are still smaller than $J_{\rm crit}$ (Shang et al., 2010; Wolcott-Green et al., 2017), the value required to dissociate molecular hydrogen to a sufficient extent that the gas stays warm ($T \sim 10^4$ K) throughout the collapse (e.g., Ahn et al., 2009a).

For baryon-dark matter streaming, we include three cases corresponding to 0 km/s, 30 km/s (1σ) and 60 km/s (2σ), at recombination. Table 2.1 shows a grid of parameters of LW backgrounds and dark matter-baryon streaming velocities used in our simulation suite. This grid is chosen to study the effect of the LW background and streaming independently, as well as to test the assumption of independence when both processes are present, something that has been assumed in previous works (e.g., Fialkov et al., 2013).

2.3 Results

In this section we describe our results for $M_{\rm crit}$ and its dependence on redshift, LW background intensity and the magnitude of the baryon-dark matter streaming velocity. In the following subsections, we describe the dependence of $M_{\rm crit}$ on redshift with LW radiation in the absence of streaming, and streaming in the absence of LW radiation. Finally, we present the effect on $M_{\rm crit}$ when a LW background and streaming are simultaneously included.

2.3.1 LW flux, no streaming velocities

Figure 2.3 shows $M_{\rm crit}$ as a function of redshift for four different LW backgrounds of $J_{\rm LW} = 0$, 1, 10 and 30 J_{21}. For each redshift, $M_{\rm crit}$ is measured, along with an estimate of the uncertainty, as described in Section 2.2. We will begin by discussing the case of $J_{21} = 0$ (blue curve at the bottom). We observe that $M_{\rm crit}$ increases with decreasing redshift. This can be fit as a power law with $M_{\rm crit} \propto (1+z)^{-1.58}$ as can be seen from the top row of Table 2.2. The redshift dependence of $M_{\rm crit}$ has been previously proposed in analytical models (Haiman et al., 1996; Tegmark et al., 1997; Trenti & Stiavelli, 2009), and has often been assumed to correspond to a fixed virial temperature and therefore vary as $M_{\rm crit} \propto (1+z)^{-1.5}$ (Visbal et al., 2014b) as $M_{\rm vir} \propto T_{\rm vir}^{3/2}(1+z)^{-3/2}$ (see Equation 26 in Barkana & Loeb, 2001); however this dependence has not been detected in previous simulations with a statistical sample of halos (Machacek et al., 2001; Schauer et al., 2019). Here we find a dependence consistent with this redshift evolution. This dependence is relatively simple to understand: if the gas temperature in the halo is approximately equal to the virial temperature before runaway cooling, then, since both the H_2 formation rate and the cooling rate depend most sensitively on temperature, efficient cooling should depend mostly on the virial temperature. Our results nicely confirm that picture. For further discussion on the redshift dependence of $M_{\rm crit}$, see Section 2.4.2.

Figure 2.3 shows that, as the LW background increases from $J_{\rm LW} = 0$ to $J_{\rm LW} = 1$, 10 and 30 J_{21}, then $M_{\rm crit}$ also increases. Boosting the LW radiation dissociates molecular hydrogen, hence halos need to be more massive to host cold-dense gas in the presence of a high LW radiative flux. This increase in $M_{\rm crit}$ with LW background can also be seen from Table 2.2. The third column ($M_{z=20}$) denotes $M_{\rm crit}$ at $z = 20$ for a fit assuming a power law for redshift dependence. $M_{z=20}$ increases from $2.04 \times 10^5 \pm 3.79 \times 10^3 {\rm M}_\odot$ for $J_{\rm LW} = 0$ to $3.73 \times 10^6 \pm 2.73 \times 10^5 {\rm M}_\odot$ for $J_{\rm LW} = 30 J_{21}$. At $z = 15$, we see an increase in $M_{\rm crit}$ by a factor of $2-3$ when going from $J_{\rm LW} = 0$ to $J_{\rm LW} = J_{21}$, whereas that increase was by a factor of $15-20$ in some previous works (e.g., Machacek et al., 2001; O'Shea & Norman, 2007; Visbal

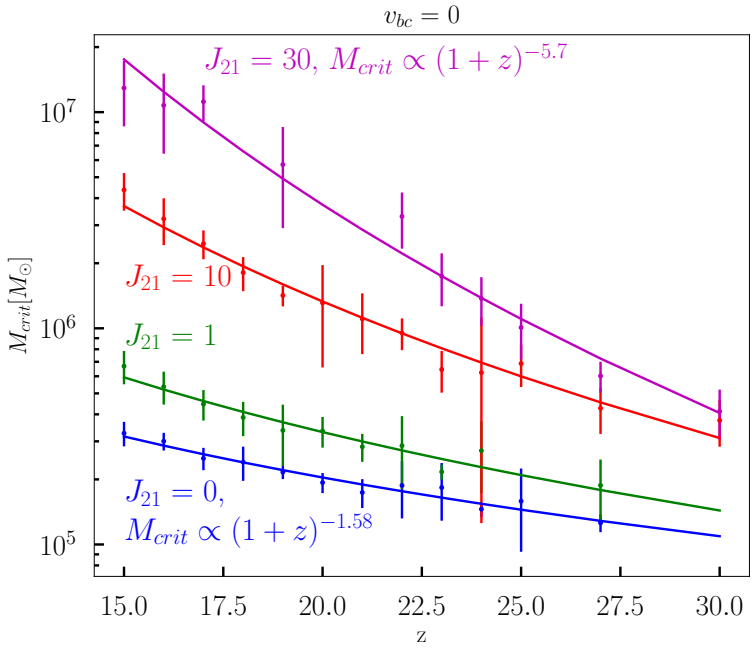

Figure 2.3: The value of $M_{\rm crit}$ as measured from a set of simulations with varying LW background as a function of redshift for a region with no dark matter-baryon streaming. The four lines correspond to LW backgrounds of 0, 1, 10 and 30 J_{21} respectively. $M_{\rm crit}$ increases with decreasing redshift. The exponent of $(1+z)$ changes from -1.6 to -2.1, -3.7 and -5.7 for LW backgrounds going from 0 to 1, 10 and 30 J_{21}.

et al., 2014b). The primary reason for this difference with those papers is the inclusion of the improved self-shielding prescription from Wolcott-Green & Haiman (2019); note that no self-shielding was included in Machacek et al. (2001) or O'Shea & Norman (2007). The effect of self-shielding will be discussed in more detail in Section 2.4. For the highest LW background considered here (30 J_{21}), we see an increase in $M_{\rm crit}$ by nearly two orders of magnitude, increasing from $3 \times 10^5\,{\rm M}_\odot$ to $2 \times 10^7\,{\rm M}_\odot$ at $z = 15$, as shown in Figure 2.3.

Apart from seeing a redshift dependence on $M_{\rm crit}$ for $J_{\rm LW} = 0$, we also find that the redshift dependence of $M_{\rm crit}$ gets steeper with increasing LW flux, as can be seen in Figure 2.3 and Table 2.2. The exponent of the z-dependence changes from -1.58 when $J_{\rm LW} = 0$ to -2.14, -3.74 and -5.70 for $J_{\rm LW}$ of 1, 10 and 30 J_{21}, respectively as can be seen from the first 4 rows of Table 2.2. This means that the increase in $M_{\rm crit}$ due to the LW background is more prominent at lower redshifts than at higher redshifts. $M_{\rm crit}$ for all the redshifts can be found in the accompanying file.

We can better understand this redshift dependence by examining the molecular hydrogen content in halos, which is discussed in more detail in Section 2.3.4. We describe a simple analytic model to understand the steeper z-dependence in presence of LW background in Section 2.4.2.

2.3.2 Streaming velocities, no LW flux

Next, we look at the effect of baryon-dark matter streaming on $M_{\rm crit}$ in the absence of a LW flux. Figure 2.4 shows $M_{\rm crit}$ as a function of redshift without any LW background present. The three lines show $M_{\rm crit}$ for 3 different dark matter-baryon streaming values at recombination, corresponding to no streaming, 30 km/s (1σ) and 60 km/s (2σ). In the regions with high streaming velocity, dark matter halos need to be more massive, with deeper potential wells, to have sufficient dense gas at their center, resulting in increased $M_{\rm crit}$. From Table 2.2, we can see that $M_{\rm crit}$ increases by nearly a factor of 3 for the case with 1σ streaming and by nearly a factor of 10 for the case with 2σ at $z = 20$.

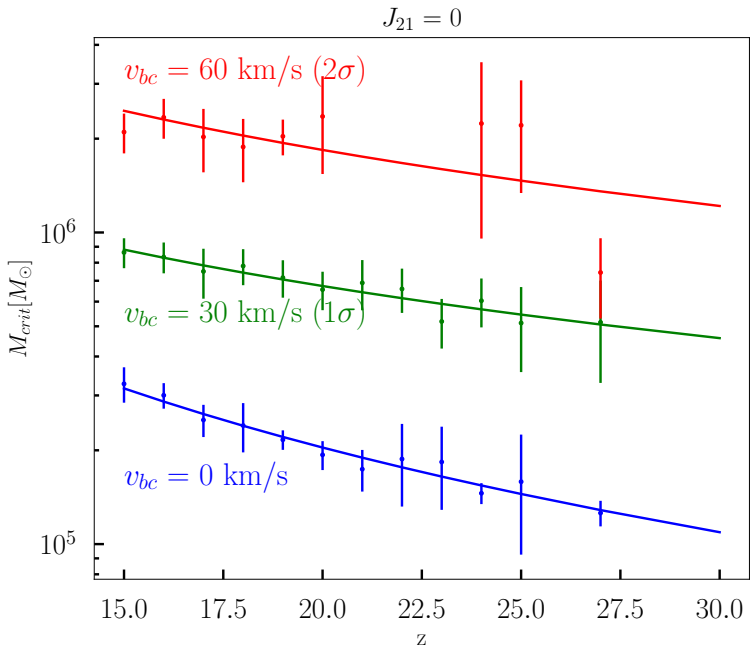

Figure 2.4: $M_{\rm crit}$ as a function of redshift without a LW background. The three lines show results from simulations with three different dark matter-baryon streaming velocities at recombination: 0, 30 km/s (1σ) and 60 km/s (2σ). Halos in regions with high streaming velocity need to be more massive in order to host cold dense gas and hence have higher $M_{\rm crit}$. The z-dependence becomes somewhat less steep with increasing streaming velocity, which can be explained by the fact that streaming velocity decreases with time as $(1+z)$.

$J_{\rm LW}(J_{21})$	$v_{\rm bc}$ (km/s)	$M_{z=20}(M_\odot)$	α	Q_1 ($M_{z=20}(M_\odot)$)	Q_3 ($M_{z=20}(M_\odot)$)
0	0	$2.05 \times 10^5 \pm 4.17 \times 10^3$	1.58 ± 0.13	1.76×10^5	2.81×10^5
1	0	$3.31 \times 10^5 \pm 9.78 \times 10^3$	2.14 ± 0.18	2.76×10^5	4.33×10^5
10	0	$1.33 \times 10^6 \pm 5.03 \times 10^4$	3.74 ± 0.19	9.80×10^5	1.90×10^6
30	0	$3.73 \times 10^6 \pm 2.73 \times 10^5$	5.70 ± 0.32	2.98×10^6	4.26×10^6
0	30 (1σ)	$6.71 \times 10^5 \pm 1.22 \times 10^4$	1.05 ± 0.09	5.28×10^5	8.80×10^5
1	30 (1σ)	$1.01 \times 10^6 \pm 2.11 \times 10^4$	2.00 ± 0.11	8.29×10^5	1.16×10^6
10	30 (1σ)	$2.90 \times 10^6 \pm 2.06 \times 10^5$	4.31 ± 0.41	1.94×10^6	3.74×10^6
0	60 (2σ)	$1.84 \times 10^6 \pm 2.05 \times 10^5$	1.06 ± 0.59	1.26×10^6	2.37×10^6
1	60 (2σ)	$2.81 \times 10^6 \pm 1.17 \times 10^5$	1.16 ± 0.24	2.39×10^6	3.26×10^6

Table 2.2: The fit parameters for redshift evolution fit as $M_{\rm crit} = M_{z=20}((1+z)/21)^{-\alpha}$ for all the combinations of LW background and streaming velocities used in the simulations. The fifth and sixth columns show the first and third quartiles respectively corresponding to masses where 25% and 75% of the halos at that mass have cold-dense gas. These quantities can be used to estimate the scatter around $M_{\rm crit}$.

Figure 2.4 shows that the z-dependence of $M_{\rm crit}$ does not change as prominently as for the case with a LW background. From Table 2.2, the exponent α characterizing the z-dependence decreases from 1.61 for no streaming to 0.99 for streaming of 30 km/s at recombination (1σ) and to 1.06 for streaming of 60 km/s at recombination (2σ). As can be seen from Figure 2.4, for 2σ streaming, $M_{\rm crit}$ becomes nearly z-independent if we exclude the point for $z = 27$. This is not surprising given the fact that the streaming velocity decreases as $\propto (1+z)$ and so is more effective at suppressing the build up of baryons at high redshifts. Hence, $M_{\rm crit}$ increases more at high redshifts as compared to low redshifts, resulting in a shallower slope.

2.3.3 Combined LW flux and streaming velocities

We now look at the most general case, when both a LW background and dark matter-baryon streaming are present. Fialkov et al. (2013) assumed that the effects of these processes are independent of each other and that the increase in $M_{\rm crit}$ from both processes would be multiplicative. As we have run simulations with multiple values of streaming and LW background present simultaneously, we can test this underlying assumption.

Figure 2.5 shows the increase in $M_{\rm crit}$ as a ratio when the LW background is increased

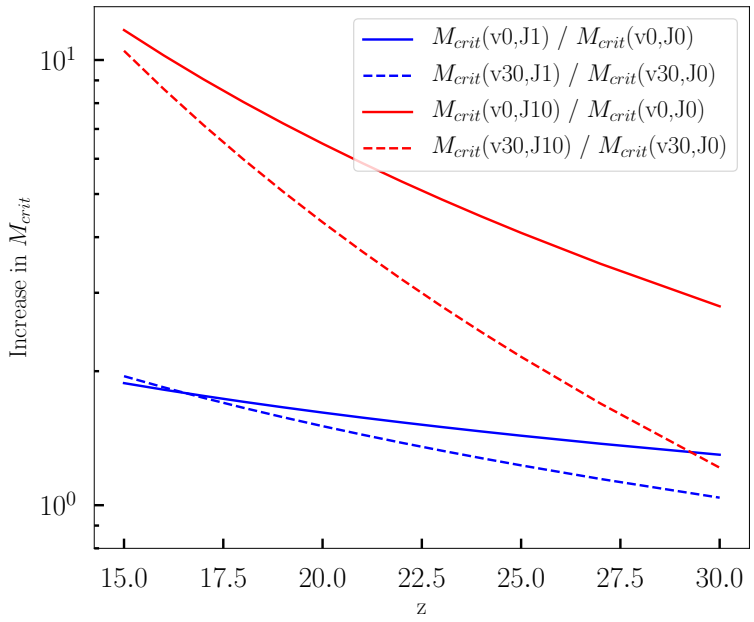

Figure 2.5: The increase in $M_{\rm crit}$ when a LW background is added (as a ratio), either in the presence or absence of dark matter-baryon streaming. The blue and red lines denote ratios of $M_{\rm crit}$ when $J_{\rm LW}$ is increased from $J_{\rm LW} = 0$ to 1 and from 0 to 10 J_{21}, respectively. The solid lines show the respective ratios when there is no streaming present, whereas dashed lines correspond to the case where the streaming velocity is 30 km/s (1σ) at recombination. If the effects of LW background and streaming on $M_{\rm crit}$ were independent and multiplicative, then the solid and dashed lines would overlap each other in both cases. Instead we see that the increase in $M_{\rm crit}$ because of a LW background radiation is less prominent in regions with high streaming velocity.

from $J_{\rm LW} = 0$ to J_{21} (blue) and from 0 to $10J_{21}$ (red), keeping the streaming the same. The solid lines show this increase for a region with no baryon-dark matter streaming, whereas dashed lines show the increase for a region corresponding to a streaming velocity of 30 km/s (1σ) at recombination. If the effects due to streaming and LW background were completely independent of each other and were multiplicative in nature, we would expect the solid and dashed lines to overlap. The fact that the dashed line is lower than the solid line for most of the redshift range suggests that the increase in $M_{\rm crit}$ because of LW flux is lower in regions with high streaming. In other words, the two effects are not entirely independent and the combined impact is not fully multiplicative – instead, the combination of both tends to be slightly less effective than if they were each operating independently.

As noted above, the z-dependence of $M_{\rm crit}$ becomes steeper with increasing LW background, as shown by the z-dependence of the ratios of $M_{\rm crit}$ in Figure 2.5. This phenomenon is stronger in the region with baryon-dark matter streaming, which can be seen from the fact that the z-dependence of the $M_{\rm crit}$ ratios is steeper for the region with streaming present (dashed line) than without (solid line).

2.3.4 Gas properties of the central regions of halos

Finally, we present the gas properties of the central regions of the halos. Figure 2.6 shows the number density, molecular hydrogen fraction, and gas temperature for the densest cell in each dark matter halo as a function of virial mass for three simulations at $z = 15$. The left column shows a simulation with neither LW flux nor baryon-dark matter streaming; the middle column represents a run with $J_{\rm LW} = J_{21}$ but no streaming, while the right column presents a case with a streaming velocity ($v_{\rm bc}$) of 30 km/s (1σ) (at recombination) in the absence of any LW flux. The blue dots represent halos that have at least one cell with cold dense gas and red dots represent halos without cold dense gas. The vertical blue lines and the shaded region around them indicate the critical mass for each run (and the uncertainty of that measurement, as described above). We can see that all of these properties show trends

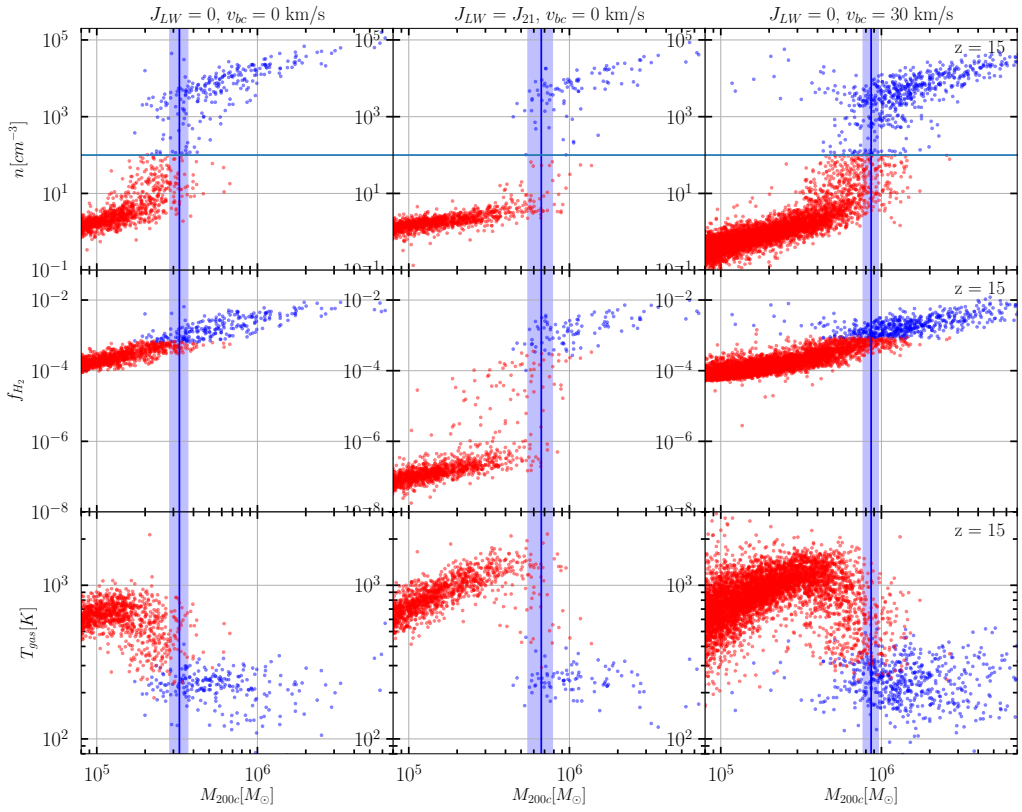

Figure 2.6: The gas number density (top panels), molecular hydrogen fraction (middle panels) and temperature (bottom panels) for the densest cell in each halo at $z = 15$. The three columns represent cases with no LW flux and no streaming (left), LW flux but no streaming (center) and streaming but no LW flux (right). The blue dots represent halos that have cold dense gas and red dots represent halos without cold dense gas. The vertical blue line and the shaded region around it denotes $M_{\rm crit}$ for each of the three runs, and our estimate of the uncertainty on it.

with the virial mass, but with a significant scatter.

The top row of Figure 2.6 shows that for warm halos (those without cold-dense gas, shown as red points), the gas density increases steadily with the virial mass (or temperature) of the halo. This is in contradiction with the common assumption (e.g., Trenti & Stiavelli, 2009) that the gas density in a halo is assumed to be only a function of redshift (this assumption is based on the idea that the central density is a fixed multiple of the mean density at that redshift). Instead, we find that the density increases nearly linearly with halo mass. Part of this increase is due to the entropy of the gas that arises due to heating at high redshift from the CMB background – this entropy ($K \propto T/n^{2/3}$) can be higher than the entropy due to shock heating from gas falling into the dark matter halo, and therefore results in an enhanced pressure which resists compression. If (as we see below) $T \sim T_{\rm vir} \sim M_{\rm vir}^{2/3}$, then, for fixed K, $n \propto M_{\rm vir}$, as observed in Visbal et al. (2014a).

This approximately linear scaling for the warm halos persists for different mass ranges in the three columns, depending on the cooling properties of the gas. In each case, near $M_{\rm crit}$, the cooling time of the central gas becomes shorter than the Hubble time and the gas starts to cool and increase in density up to nearly $1 \times 10^4\,{\rm cm}^{-3} (n_{crit})$ and then increases slowly with virial mass for more massive halos (although the central density for halos with cold-dense gas may depend on the artificial pressure support described above).

The gas temperature also shows a transition near $M_{\rm crit}$ in the bottom row of Figure 2.6. For warm halos, $T_{gas} \sim T_{\rm vir}$, as expected for gas which is in virial equilibrium; however as cooling becomes efficient, the gas temperature drops significantly and rapidly, from $T_{\rm vir}$ down to about 200 K for halos with cold-dense gas (below this temperature, the H_2 cooling becomes increasing inefficient).

The middle row of Figure 2.6 shows the molecular hydrogen fraction (f_{H_2}) as a function of virial mass. For the cases without LW flux (left and right columns), f_{H_2} show a very clear monotonic trend with virial mass – in particular, despite the rapid change in density and temperature, there is no break near $M_{\rm crit}$. The middle panel, with a LW background

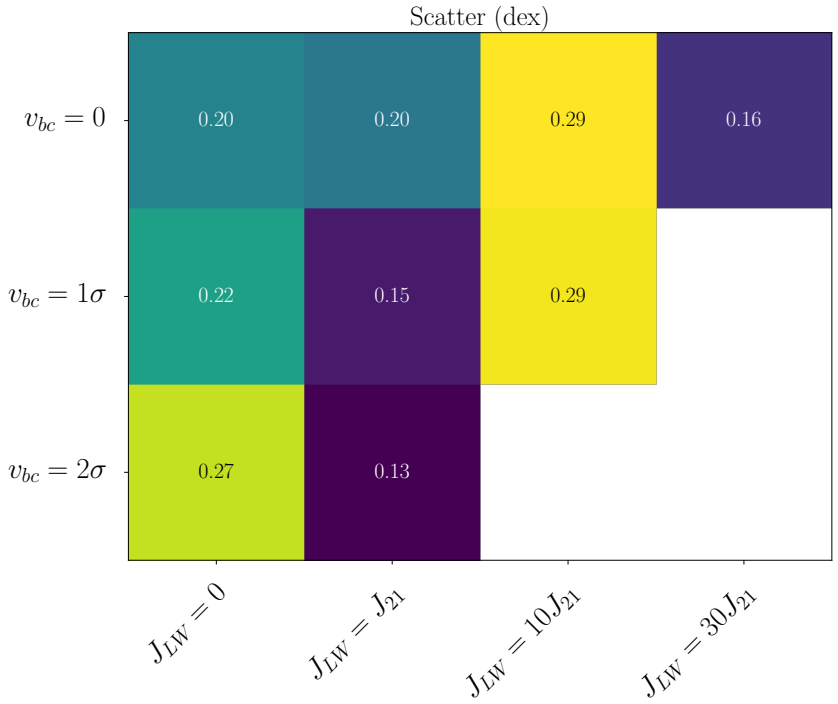

Figure 2.7: Relative scatter in dex (difference between Q_3 and Q_1) on $M_{\rm crit}$. We expect it to be converged for the cases with a large number of halos with cold dense gas (e.g., for $v_{\rm bc} = 0$, $J_{\rm LW} = 0, 1$; $v_{\rm bc} = 30$ km/s, $J_{\rm LW} = 0$ cases) and to be a lower limit of the underlying scatter for other cases.

of J_{21}, has a lower molecular hydrogen fraction for warm halos, as expected. This gas is in photo-dissociative equilibrium, and the slow increase in f_{H_2} arises from the temperature dependence of the formation rate. Self-shielding of gas from the LW background starts to become important near $M_{\rm crit}$ resulting in a rapid increase of f_{H_2}, essentially up to a fraction consistent with the other simulations (that have no LW background). The effect of self-shielding is discussed further in Section 2.4.

2.3.5 Scatter on $M_{\rm crit}$

The transition from warm halos to halos with cold dense gas does not happen abruptly at $M_{\rm crit}$ and there is a significant scatter around it. We try to quantify this scatter by finding the masses corresponding to bins where 25% and 75% of the halos have cold dense gas in Table 2.2 (denoted Q_1 and Q_3, respectively). Figure 2.7 shows the difference between Q_3

and Q_1 in log space. From this figure, we see the scatter is in the 0.2-0.3 dex range, with no clear trend with baryon-dark matter streaming or radiation strength.

The scatter is accurately measured when there is a large number of halos with cold dense gas. With fewer halos, the transition between halos with warm and cold dense gas is more likely to be abrupt, resulting in a smaller scatter, as is the case for e.g. $v_{\rm bc} = 0$; $J_{\rm LW} = 30 J_{21}$ or $v_{\rm bc} = 2\sigma$; $J_{\rm LW} = J_{21}$. To verify this claim, we split the halos for the $v_{\rm bc} = 0$; $J_{\rm LW} = 0$ case (which has many halos) into 6 samples of equal size and calculate the scatter on each of them. The values of the scatter on the split samples are ~ 0.1, which is smaller than the scatter of 0.2 when including all halos. For $v_{\rm bc} = 0$, the scatter increases from $J_{\rm LW} = J_{21}$ to $10 J_{21}$, as the number of cold dense halos increase as we shift from a box size of 0.5 $\rm h^{-1}$ Mpc to 1 $\rm h^{-1}$ Mpc. We conclude that the underlying scatter is equal to or larger than the scatter reported here. We believe that the estimated scatter is converged to the underlying scatter when the uncertainty on $M_{\rm crit}$ (i.e. the bin sizes used) is much smaller than the value of $M_{\rm crit}$ estimated (e.g., for $v_{\rm bc} = 0$, $J_{\rm LW} = 0, 1$; $v_{\rm bc} = 30$ km/s, $J_{\rm LW} = 0$ cases).

2.4 Discussion

2.4.1 An empirical fit for $M_{\rm crit}(J_{\rm LW}, v_{\rm bc}, z)$

One of the key aims of this work is to give a simple fit for $M_{\rm crit}(J_{\rm LW}, v_{\rm bc}, z)$ based on our simulation suite, which can then be used in various analytic models. In this section, we provide fits at a few different levels of accuracy and leave it to the reader to decide if they want to use the simple fit we provide or if they prefer to use a better fitting function based on the individual $M_{\rm crit}$ values we report.

Using the method described in Section 2.2, we calculate the critical mass for a given LW background, streaming velocity, and for a specific redshift. We fit for the redshift evolution with the following simple form:

$$M_{\rm crit}(z) = M_{z=20} \left(\frac{1+z}{21} \right)^{-\alpha} . \tag{2.1}$$

All of the fits are done using the Scipy function 'curve_fit'. This provides us with two fit parameters: $M_{\rm crit}$ for redshift 20 $M_{z=20}$ and the redshift exponent α, along with their uncertainties. 'curve_fit' uses χ^2 minimization for fitting and calculating the uncertainty using our measured values of $M_{\rm crit}$. We adopt $z = 20$ as our pivot point because it is the center of our range.

As mentioned in Section 2.3, when we vary the LW background and baryon-dark matter streaming, we find that this changes the normalization ($M_{z=20}$) as well as the slope (α). Hence we need to provide both of these parameters as a function of LW background and streaming:

$$M_{\rm crit}(J_{\rm LW}, v_{\rm bc}, z) = M_{z=20}(J_{\rm LW}, v_{\rm bc}) \left(\frac{1+z}{21}\right)^{-\alpha(J_{\rm LW}, v_{\rm bc})} . \tag{2.2}$$

We assume a simple functional form for $M_{z=20}$ and α as follows:

$$\begin{aligned} M_{z=20}(J_{\rm LW}, v_{\rm bc}) = (M_{z=20})_0 \, (1 + J_{\rm LW}/J_0)^{\beta_1} \\ (1 + v_{\rm bc}/v_0)^{\beta_2} \, (1 + J_{\rm LW} v_{\rm bc}/J v_0)^{\beta_3} \end{aligned} \tag{2.3}$$

and

$$\begin{aligned} \alpha(J_{\rm LW}, v_{\rm bc})) = \alpha_0 \, (1 + J_{\rm LW}/J_0)^{\gamma_1} \, (1 + v_{\rm bc}/v_0)^{\gamma_2} \\ (1 + J_{\rm LW} v_{\rm bc}/J v_0)^{\gamma_3} . \end{aligned} \tag{2.4}$$

We have assumed one term each for the LW background and streaming dependence and one term for the cross-dependence. However, if we simply fit these expressions with the constraints, we find there are too many parameters with too few data points, resulting in degeneracies between J_0 and β_1, v_0 and β_2. Therefore, we fix the pivot points J_0, v_0 and Jv_0 to be 1, 30 and 3 respectively and fit for the slopes β's. $M_{z=20}$ was fit in the log space, whereas α was fit in the linear space. The fitted β's and fit values for the overall amplitude,

$M_{z=20}$ are provided here:

$$(M_{z=20})_0 = 1.96 \times 10^5 \pm 1.33 \times 10^4 M_\odot, \tag{2.5}$$

$$\beta_1 = 0.80 \pm 0.06, \tag{2.6}$$

$$\beta_2 = 1.83 \pm 0.14, \tag{2.7}$$

$$\beta_3 = -0.06 \pm 0.04. \tag{2.8}$$

The fitted parameters for α are as follows:

$$\alpha_0 = 1.64 \pm 0.11, \tag{2.9}$$

$$\gamma_1 = 0.36 \pm 0.03, \tag{2.10}$$

$$\gamma_2 = -0.62 \pm 0.15, \tag{2.11}$$

$$\gamma_3 = 0.13 \pm 0.03. \tag{2.12}$$

In addition to this global fit, we also provide in Table 2.2 fits for the individual simulations (i.e. $M_{z=20}$ and α for all the combinations of LW background radiation and streaming velocities with the appropriate errors). We also provide $M_{\rm crit}$ with uncertainties for all redshifts for all cases in an accompanying file. Users can fit it with a different fitting function of their choice if they prefer.

The uncertainty in $M_{\rm crit}$ we provide depends on the number of halos with cold dense gas in the simulation. Therefore we have a smaller uncertainty on $M_{\rm crit}$ for lower LW flux and streaming. Apart from providing $M_{\rm crit}$ corresponding to a mass bin with half of the halos with cold dense gas, we also provide an estimate on the scatter on it. Columns 5 and 6 of Table 2.2 provide the halo masses corresponding to bins that have 25% and 75% of the halos with cold dense gas, respectively, for $z = 20$. The scatter estimate is useful for semi-analytic models that populate dark matter halos with first stars.

2.4.2 A simple model for explaining the z-dependence

A simple analytical model such as those described in Machacek et al. (2001) or Trenti & Stiavelli (2009) can be used to explain some of the redshift trends we see in terms of the quantities at the central regions of the halos.

The condition for collapse can be defined as the cooling time being shorter than the Hubble time at that redshift. The cooling time is given as

$$t_{\rm cool} = \frac{1.5 n k_B T_{\rm vir}}{\Lambda(T_{\rm vir}) n_H n_{H_2}}, \tag{2.13}$$

where we have assumed the gas temperature to be equal to the virial temperature of the halo. The cooling function behaves as $\Lambda(T) \propto T^{3.4}$ for the temperature between 120 K and 6400 K. Hence the cooling time of the gas varies as $t_{\rm cool} \propto T^{-2.4} n_{H_2}^{-1}$.

For the case with no LW flux and no streaming velocity, the central molecular hydrogen density can be fit as a power-law function of $T_{\rm vir}$ and z as

$$n_{H_2} \propto (1+z)^{1.62} T_{\rm vir}^{2.0}. \tag{2.14}$$

This is an approximate scaling relation from our simulations for halos without cold dense gas (e.g. red points in Figure 2.6). To get this relation, we first fit n_{H_2} as a function of $T_{\rm vir}$ at a given redshift and then fit for a z-dependence of n_{H_2} at $T_{\rm vir} = 1000$ K. Using this relation and the evolution of Hubble time as $t_H \propto (1+z)^{-1.5}$, we can find a redshift dependence of the critical virial temperature. As $M_{\rm vir} \propto T_{\rm vir}^{3/2}(1+z)^{-3/2}$, we get $M_{crit} \propto (1+z)^{-1.54}$ which is very close to our measured z-dependence of $(1+z)^{-1.58}$.

In the presence of LW flux, the molecular hydrogen density increases rapidly with increasing redshift. For $J_{\rm LW} = 10 J_{21}$,

$$n_{H_2} \propto (1+z)^{5.58} T_{\rm vir}^{2.2}. \tag{2.15}$$

Using this relation in equation 2.13 and equating it to the Hubble time gives a z-dependence of $M_{\rm crit} \propto (1+z)^{-2.83}$. This does not match exactly with the observed z-dependence of $\propto (1+z)^{-3.74}$, although it follows the qualitative trend of steeper z-dependence than the case without LW flux. Our simple analytic model does not precisely explain the steepening of the z-dependence with increasing LW flux. One possible reason for this discrepancy could be that the simple power-law fitting formula we used for n_{H_2} does not capture its dependence on $T_{\rm vir}$ and z accurately. The exponent for the relation between $n_{H_2} - T_{\rm vir}$ changes as a function of redshift as well, but we have not included it so as to keep the fitting formula relatively simple.

The steeping of the z- dependence of $M_{\rm crit}$ in the presence of LW flux can be primarily attributed to a steeper z-dependence of the central molecular hydrogen density. At high redshifts, gas densities are higher which results in more effective self-shielding. This explains why the molecular hydrogen density increases rapidly with redshift in the presence of LW flux. We find that the molecular hydrogen density is in equilibrium in presence of LW flux. We conclude this by comparing the self-shielding factor (f_{sh}) calculated by assuming an equilibrium for molecular hydrogen density and the self-shielding factor (f_{sh}) used in the simulation (see also the discussion in Section 2.4.5) and finding them nearly equal. This justifies the steeper slope of the molecular hydrogen with redshift in presence of LW flux.

2.4.3 Comparison with previous works

In this subsection, we compare our results with previous works. Tegmark et al. (1997) estimated a minimum mass for forming first stars using a simple analytic model. They compared the cooling time of the gas in a halo as a function of gas density, temperature and molecular hydrogen fraction, with the Hubble time in order to estimate its fate. Their estimated minimum mass depends more strongly on redshift than we find in our simulations and increases with decreasing redshift (see Figure 6 in Tegmark et al. (1997)). Tegmark et al. (1997) find an increase in $M_{\rm crit}$ from $1 \times 10^5\,{\rm M}_\odot$ to $1 \times 10^7\,{\rm M}_\odot$ approximately from

redshift of 80 to 15 in the absence of LW radiation. We, on the other hand, find $M_{\rm crit}$ to be below $3 \times 10^5\,{\rm M}_\odot$ until redshift $z = 15$.

Haiman et al. (2000) estimated the critical flux ($J_{\rm crit}$) above which the star formation in a halo is prevented as a function of $T_{\rm vir}$ and z (Figure 6). They report that halos cannot cool for a virial temperature below $10^{2.4}\,{\rm K}$. This corresponds to $M_{\rm crit}$ changing with redshift as $\propto (1+z)^{-1.5}$ which matches nicely with the z-dependence we see for the case without any LW flux ($\propto (1+z)^{-1.58}$), although $M_{\rm crit}$ corresponding to a virial temperature of $10^{2.4}\,{\rm K}$ at $z = 20$ is $9.7 \times 10^5\,{\rm M}_\odot$, which is significantly higher compared to our estimate of $2.05 \times 10^5\,{\rm M}_\odot$.

To estimate the redshift evolution of $M_{\rm crit}$ in the presence of LW flux in Haiman et al. (2000), we compare the virial temperatures corresponding to redshift 10 and 20 for $J_{\rm LW} = 10^{-2} J_{21}$. From $z = 10$ to $z = 20$, $T_{\rm vir,crit}$ changes from $1 \times 10^{3.6}\,{\rm K}$ to $1 \times 10^{2.8}\,{\rm K}$. This corresponds to a z-dependence of the critical virial temperature as $\propto (1+z)^{-2.8}$. Because $M_{\rm vir} \propto T_{\rm vir}^{3/2}(1+z)^{-3/2}$, this corresponds to $M_{\rm crit} \propto (1+z)^{-5.7}$ which is somewhat steeper than our results, although it does match our finding that the LW flux tends to steepen the dependence of $M_{\rm crit}$ on redshift. We note that their $M_{\rm crit}$ for $J_{\rm LW} = 0.1 J_{21}$ at $z = 20$ corresponds to $6.1 \times 10^6\,{\rm M}_\odot$, which is again higher than the value we find.

Machacek et al. (2001) used a statistical sample of halos to find a minimum mass for halos to form cold-dens gas. They divided halos into two redshift bins with $z > 24$ and $z < 24$ and found no evidence of epoch dependence in them. We find a strong redshift dependence in our results; however it is not clear if there is a significant difference due to the smaller number of halos they were able to analyze. Otherwise, their no LW background results agree well with what we find here; however, their LW dependence is much stronger than found in this chapter, which we ascribe to their neglect of H_2 self-shielding.

Trenti & Stiavelli (2009) used a similar analytic model to estimate the critical halo mass to form Pop III stars. They assume $T_{\rm gas} = T_{\rm vir}$, $n \propto (1+z)^3$ and a power-law relation between f_{H_2} and $T_{\rm vir}$. In the absence of LW radiation, a minimum mass can be derived by equating the cooling time of the gas to the Hubble time. This minimum mass is given

by $M_{t_H-cool} \approx 1.54 \times 10^5\,\mathrm{M}_\odot(\frac{1+z}{31})^{-2.074}$. In the presence of a LW background, a similar minimum mass can be found by assuming an equilibrium for the formation and dissociation of molecular hydrogen to estimate the molecular hydrogen fraction. This minimum mass is given by $M_{H_2-cool} \approx 6.44 \times 10^6\,\mathrm{M}_\odot J_{21}^{0.457}(\frac{1+z}{31})^{-3.557}$. Trenti & Stiavelli (2009) argue that for a dark matter halo to be able to cool via H_2, its mass must be above both of these limits.

The analytic model in Trenti & Stiavelli (2009) predicts a few properties of $M_{\rm crit}$ that we see in our simulations. It predicts a redshift evolution of $M_{\rm crit}$ in a qualitatively similar way for the case without LW radiation. It also predicts a steeper z-dependence when LW radiation is present; however it does not predict a z-dependence that changes with the background LW radiation as we see in our simulations. For the case without LW flux, Trenti & Stiavelli (2009) estimate $M_{\rm crit}$ of $\sim 3.3 \times 10^5\,\mathrm{M}_\odot$ at $z = 20$, which is close to our estimated value of $2.05 \times 10^5\,\mathrm{M}_\odot$. For the case with $J_{\rm LW} = J_{21}$, Trenti & Stiavelli (2009) estimate $M_{\rm crit}$ to be $\sim 2.57 \times 10^7\,\mathrm{M}_\odot$ at $z = 20$, which is much higher than our estimated value of $3.31 \times 10^5\,\mathrm{M}_\odot$. We speculate that this is in part due to their assumption of a central density that depends only on redshift and not halo mass, which differs significantly from what we saw in Section 2.3.4.

Schauer et al. (2019) studied the effect of the streaming velocity on $M_{\rm crit}$ of a large statistical sample using the moving mesh code AREPO (but without any LW background). We compare our results for $M_{\rm crit}$ with $M_{halo,50\%}$ quoted in Schauer et al. (2019) which is defined as the average halo mass above which 50% of the halos contain cold gas. This is similar in spirit to the criterion assumed in this work, but quantitatively distinct. Our results are in broad agreement, with streaming leading to a factor ~ 3 (~ 10) increase when a velocity of 1σ (2σ) was adopted. In detail, there are a few important differences. First, Schauer et al. (2019) found a constant $M_{halo,50\%}$ as a function of redshift (with or without baryon-dark matter streaming), whereas we find that $M_{\rm crit}$ tends to increase with decreasing redshift, consistent with a fixed virial temperature for the case without baryon-dark matter streaming. Second, we note that their $M_{halo,50\%}$ corresponding to the case without LW

background or streaming is about $1.6 \times 10^6\,\mathrm{M}_\odot$, significantly larger than our $M_{\rm crit}$, which we find to be close to $2 \times 10^5\,\mathrm{M}_\odot$. They also report the minimum halo mass to contain cold-dense gas, and this is lower, but still higher than our $M_{\rm crit}$ value, indicating that the differences cannot be solely due to different definitions. More work is required to understand these differences.

During the final stages of the completion of this chapter, a related study investigating the effect of LW flux and baryon-dark matter streaming velocity was released (Schauer et al., 2020), building on the results just discussed. Here we briefly compare our results. Again, the broad qualitative picture is in agreement, with a LW background leading to an increase in the minimum mass for cold-dense gas formation, but some important differences in the details. Schauer et al. (2020) probe a somewhat different parameter space than us, in particular lower LW backgrounds (0.01 J_{21} and 0.1 J_{21}), which makes a direct comparison difficult. If the fit from Schauer et al. (2020) for the $J_{\rm LW}$ dependence on $M_{\rm crit}$ is extrapolated to $J_{\rm LW} = J_{21}$, that corresponds to an increase in $M_{\rm crit}$ by nearly a factor of 10 when $J_{\rm LW}$ changes from 0 to J_{21}, whereas we find an increase by just a factor of two.

Skinner & Wise (2020) also model Pop III star forming in low mass halos including self-shielding. Although, it is difficult to do a one-to-one comparison with their results, Skinner & Wise (2020) find Pop III stars forming in halos of mass $3 \times 10^5\,\mathrm{M}_\odot$ (and larger) at $z = 20$ for a LW background of slightly less than J_{21} which is broadly consistent with our results.

2.4.4 Resolution tests

We have performed a number of tests to check for the convergence of our simulations, both with respect to the dark matter particle mass (which is set by the initial grid resolution in ENZO) as well as the number of AMR levels which determine the minimum size of the baryon cells at high densities.

Figure 2.8 shows the total mass of the cold dense gas ($T < 0.5T_{\rm vir}$, $n > 100\,\mathrm{cm}^{-3}$) as a function of halo mass at $z = 22$ for a 0.5 h^{-1} Mpc box. The symbols denote three different

resolutions. The black plus symbols represent a simulation with a 512^3 grid and 6 AMR levels, which corresponds to the dark matter particle mass of $\sim 100 M_\odot$ and smallest cell size of ~ 21.8 cpc. The red triangles correspond to a 256^3 grid with a dark matter particle mass of $\sim 800 M_\odot$ and the same cell size. Finally, the blue stars correspond to a 256^3 grid with only 5 AMR levels which corresponds to a minimum cell size of ~ 85 cpc.

We can see from Figure 2.8 that most of the blue stars and red triangles have overlap; in other words, they have similar amounts of cold dense gas, particularly for the more massive halos. In most of our simulations we use the higher spatial resolution of the two runs analyzed here. When we compare red triangles and black plus symbols, which have the same spatial resolution but different dark matter particle masses, we see more black plus symbols near the low mass end representing more halos with cold dense gas. This is not surprising as a 10^5 M$_\odot$ halo would be resolved by just over 100 dark matter particles for the lower resolution, whereas it needs to be resolved by at least 500 particles to have an accurate estimate of the gas content (Naoz et al., 2009). Hence, for the runs with low LW background and streaming, we use a resolution corresponding to a dark matter particle mass of 100 M$_\odot$ such that even a halo of mass 10^5 M$_\odot$ is resolved by 1000 particles. However for halos of mass 10^6 M$_\odot$ or more, we can see that black plus symbols and red triangles overlap, as they are well resolved by the low resolution simulation as well. Therefore, in order to have more large halos for runs with high LW background and streaming where $M_{\rm crit}$ would be higher, we use a larger 1 h^{-1} Mpc box with a 512^3 grid, corresponding to a dark matter particle mass of 800 $M_\odot$.

2.4.5 Self-shielding

Many previous works investigating the effect of LW radiation on $M_{\rm crit}$ have ignored the self-shielding of gas from LW radiation (Machacek et al., 2001; Wise & Abel, 2007; O'Shea & Norman, 2007). Wolcott-Green et al. (2011); Wolcott-Green & Haiman (2019) have emphasized the importance of self-shielding and provided a prescription for including it in simulations using a multiplicative factor f_{sh} which depends mainly on the column density

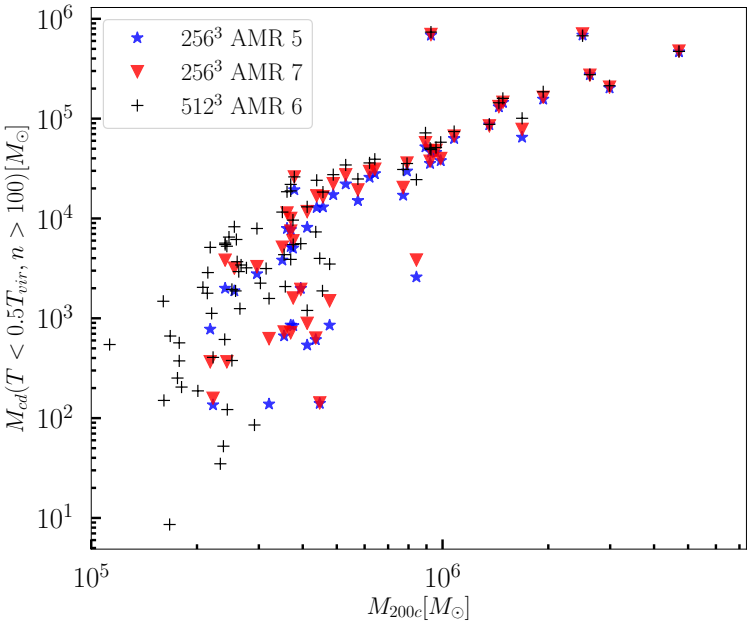

Figure 2.8: The effect of resolution on the total mass of cold dense gas in three simulations with the same initial conditions but different resolutions. We plot M_{200c} of each halo identified on the x-axis and the mass of the cold dense gas ($T < 0.5T_{\rm vir}$, $n > 100\,{\rm cm}^{-3}$) on y-axis for $z = 22$ for a box of size 0.5 h^{-1} Mpc. The blue stars and red triangles correspond to a 256^3 grid with two different AMR levels (see text for additional details). The black plus symbols correspond to 512^3 grid with the same cell resolution as the run with red triangles.

of molecular hydrogen and gas temperature. Because of self-shielding, the effective LW radiation penetrating the central dense region is lowered and the central region can have higher molecular hydrogen densities. In the presence of self-shielding, we expect $M_{\rm crit}$ to decrease for a fixed LW background, as lower mass halos would be able to have sufficient molecular hydrogen to cool.

Figure 2.9 compares two simulations with (blue) and without (red) self-shielding for $J_{\rm LW} = J_{21}$ at $z = 20$. The red and blue dots represent individual halos and have a y-value of 1 if they have cold dense gas and 0 if they do not. The solid lines denote the fraction of halos that have cold dense gas in each mass bin as explained in Section 2.3. The simulation with self-shielding has significantly smaller $M_{\rm crit}$ as can be seen by comparing the blue and red solid lines in this figure.

To explicitly demonstrate the importance of self-shielding, in Figure 2.10 we show the self-shielding parameter f_{sh} as a function of halo mass for a simulation with $J_{\rm LW} = J_{21}$ and no streaming at $z = 15$. Low mass halos have no self-shielding and have $f_{sh} = 1$. Halos with mass closer to $M_{\rm crit}$ have higher gas density, resulting in a reduced f_{sh} which further increases the molecular hydrogen density and enhances cooling. As shown in Figure 2.10, warm halos with masses slightly smaller than $M_{\rm crit}$ also have self-shielding factors which are significantly lower than 1. In the absence of self-shielding, molecular hydrogen densities would be sufficiently high only in more massive halos, resulting in an increased $M_{\rm crit}$.

2.5 Summary and conclusion

We performed a simulation suite of minihalos (halos with virial temperatures below the atomic cooling limit) using the cosmological hydrodynamics code ENZO in order to constrain the dependence of the critical dark matter halo mass for Pop III star formation on LW radiation, baryon-dark matter streaming, and redshift. We performed a set of simulations varying the LW background and the streaming velocity over the expected range for each candidate, using simulation volumes large enough to create a large sample of such halos with

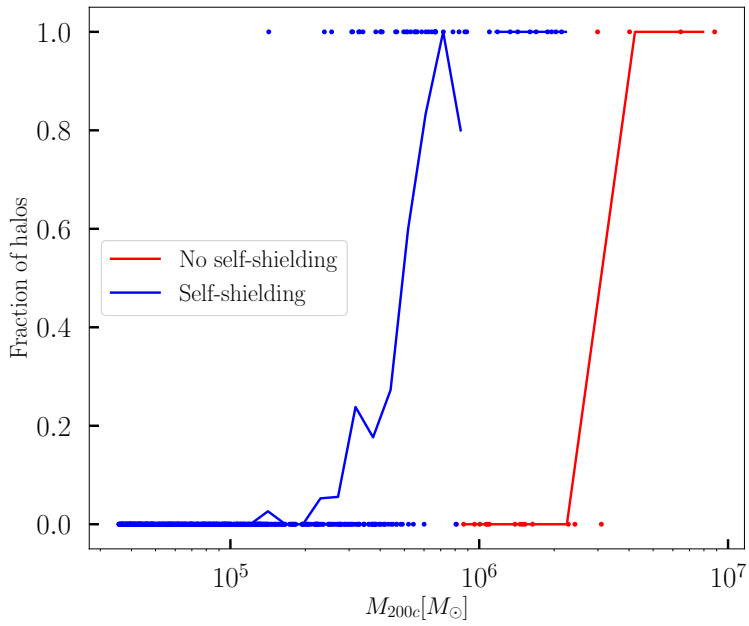

Figure 2.9: Comparison of two simulations, both with $J_{\rm LW} = J_{21}$ at $z = 20$, but one (red dots) without self-shielding from LW radiation, and the other (blue dots) with a self-shielding prescription based on Wolcott-Green & Haiman (2019). Each dot indicates a halo, with the x-axis indicating the halo mass and the y-axis showing the presence ($y = 1$) or absence ($y = 0$) of cold-dense gas. The solid lines show the fraction of halos that have cold dense gas at a given mass bin using the method described in Section 2.2. Inclusion of self-shielding decreases $M_{\rm crit}$ significantly.

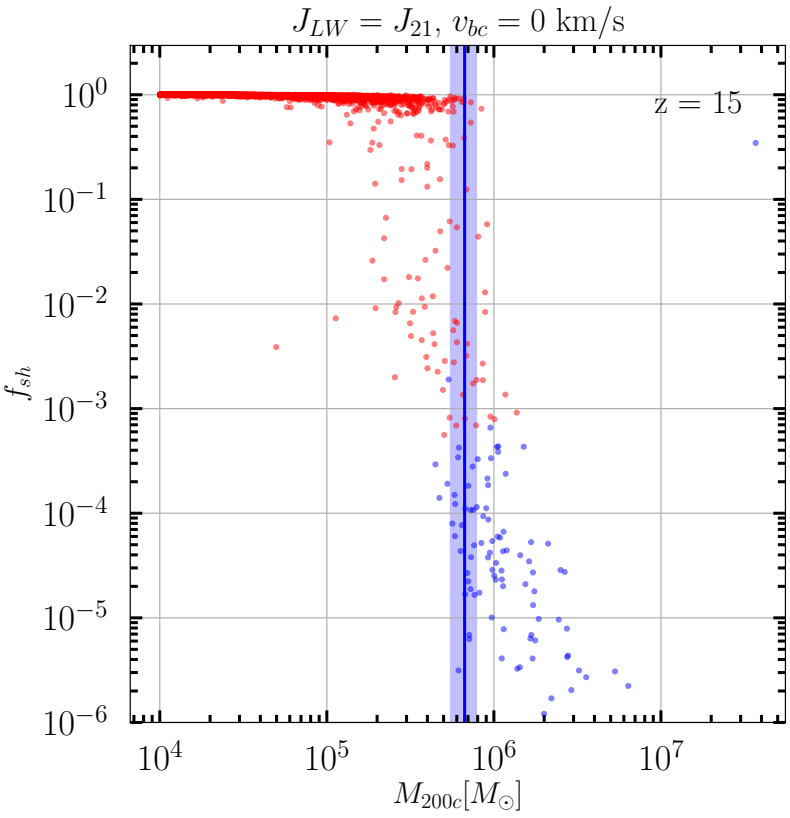

Figure 2.10: The self-shielding factor f_{sh} as defined in Wolcott-Green & Haiman (2019) for the densest cell of each halo for the simulation with no streaming and a LW background of J_{21}. The effective LW radiation is equal to the background LW flux multiplied by f_{sh}. The blue (red) dots represent halos that have at least one cell with (without) cold dense gas. The vertical blue line and the shaded region around it shows $M_{\rm crit}$ and its uncertainty. Halos with cold dense gas have effectively self-shielded themselves from the background LW radiation.

a resolution sufficient to accurately identify when cooling produces cool, dense gas. We then analyzed the simulations to determine $M_{\rm crit}$, the dark matter halo mass for which 50% of halos hosted cold-dense (potentially star-forming) gas. We also report the uncertainty on $M_{\rm crit}$ and the scatter (the mass range over which 25%-75% of the halos have cold-dense gas). Our conclusions can be summarized as follows.

1. We identify a clear redshift dependence of the critical mass, finding that $M_{\rm crit}$ increases with decreasing redshift as $\propto (1+z)^{-1.58}$ for the case with no LW flux and no streaming, consistent with a fixed virial temperature, a relation which has been predicted in analytic models but not previously seen in numerical works with a statistically significant sample of halos.

2. We find a LW background increases $M_{\rm crit}$ and that the redshift dependence of $M_{\rm crit}$ changes from a slope of -1.58 to -5.70 as the LW flux increases from 0 to $30J_{21}$ and becomes shallower with increasing dark matter-baryon streaming velocity.

3. We find that self-shielding of the gas from LW radiation is important and decreases $M_{\rm crit}$ for a given LW flux. $M_{\rm crit}$ increases by a factor of 2 when going from $J_{\rm LW}$ of 0 to J_{21} – nearly an order of magnitude smaller increase than previous results that did not incorporate self-shielding.

4. We performed simulations in which both LW flux and streaming are present in order to critically examine the idea that their impact on $M_{\rm crit}$ are independent of each other and act in a multiplicative way. We conclude that the two effects are not entirely independent and the combined impact is not fully multiplicative – instead, their impact in combination tends to be somewhat less effective than if they were each operating independently. The increase in $M_{\rm crit}$ can be smaller by nearly a factor of 2-3 at high redshifts when compared to an estimate based on the assumption of independence.

5. We provide a fit for $M_{\rm crit}$ as a function of LW flux, baryon-dark matter streaming and

redshift which can be used by semi-analytic models to make predictions for Pop III stars and their observable signatures.

Chapter 3: Fragmentation in Population III galaxies formed through ionizing radiation

3.1 Introduction

Population III (Pop III) stars are the first generation of stars forming from primordial gas. Numerical simulations of ΛCDM predict that Pop III stars typically form in minihalos of mass $10^5 - 10^6 M_\odot$ (Haiman et al., 1996; Tegmark et al., 1997; Machacek et al., 2001; Abel et al., 2002; Bromm et al., 2002; Yoshida et al., 2003; Greif, 2015). The typical virial temperature of these minihalos is below the atomic cooling threshold, so the gas cools via rotational-vibrational transition lines of H_2 in the absence of metals.

Lyman-Werner (LW) radiation, in the range 11.2-13.6 eV, can photo-dissociate molecular hydrogen. As the star formation density in the Universe increases, it creates a LW radiation background that can suppress Pop III star formation in small mihihalos (Haiman et al., 1997; Machacek et al., 2001; Wise & Abel, 2007; O'Shea & Norman, 2007; Wolcott-Green et al., 2011; Visbal et al., 2014b). In regions with strong LW background radiation, Pop III star formation is suppressed in halos with virial temperatures up to 10^4 K, where atomic hydrogen cooling becomes efficient. This temperature corresponds to a mass of $M_{vir} \approx 3 \times 10^7((1+z)/11)^{-3/2} M_\odot$ (Barkana & Loeb, 2001).

The lifetime of massive Pop III stars is short, a few Myr (Schaerer, 2002), which leads to the enrichment of the gas with metals via supernova winds and the transition to the formation of lower-mass Pop II stars (Bromm & Loeb, 2003; Schneider et al., 2006; Smith

This section contains text from an article published in the Astrophysical Journal (Kulkarni et al., 2019).

& Sigurdsson, 2007; Maio et al., 2010). This means that Pop III stars are typically not expected to be found in more massive halos because the metal cooling will lead to lower temperatures (and lower mass stars). Although, inefficient metal mixing may lead to Pop III star formation at much lower redshift (Scannapieco et al., 2003; Jimenez & Haiman, 2006).

It has been suggested that, in the presence of a strong ionizing radiation source, Pop III stars can form in much more massive halos (Johnson, 2010; Visbal et al., 2016, 2017; Yajima & Khochfar, 2017; Johnson & Aykutalp, 2018). Previous works have investigated photoevaporation of minihalos because of ionizing radiation (Shapiro et al., 2004; Iliev et al., 2005) and the suppression of star formation in more massive halos because of reionization (Shapiro et al., 1994; Thoul & Weinberg, 1996; Gnedin, 2000; Dijkstra et al., 2004; Hoeft et al., 2006; Okamoto et al., 2008; Sobacchi & Mesinger, 2013; Noh & McQuinn, 2014).

Visbal et al. (2017) studied Pop III star formation in three halos subjected to various background ionizing fluxes. They concluded that, for high fluxes, ionization and photo-heating of the gas can delay cooling and collapse into stars in halos up to masses significantly higher than the atomic cooling threshold. The threshold halo mass for collapse increases with increasing flux, and saturates at a value approximately an order of magnitude above the atomic cooling threshold for very high fluxes. The ionizing flux keeps gas ionized and hot ($> 10^4$ K) until the dark matter halo grows and the gas is compressed to sufficiently high density that self-shielding becomes important. This leads to a dense self-shielded core with an increased fraction of neutral hydrogen, causing the gas to cool and collapse.

In this work, we further study the properties of such massive Pop III galaxies, focusing, in particular, on the fragmentation processes within the central core and the clump mass function in such a galaxy. We present our results for three halos that we have selected to study using zoom-in simulations, exploring their collapse properties, gas fragmentation and discussing the impact of ionizing radiation from the stars that form.

This chapter is structured as follows. In section 3.2, we describe the set up for our cosmological zoom-in simulations, and how we have included background ionizing radiation. We

also detail the sink particle adaption in ENZO that we have used to study the fragmentation. In section 3.3, we describe the properties of collapse as a function of background ionizing flux, radial profiles in halos at the time of runaway collapse and properties of the sink particles such as their masses and accretion rates, and estimates of their corresponding stellar masses. In section 3.4, we discuss the collapse criterion for a halo with a given background ionization flux in more detail, the effect of radiation feedback from the stars formed, as well as the expected frequency of our clusters and observational prospects with JWST. We summarize our conclusions in section 3.5.

3.2 Methodology

3.2.1 Simulation set-up

We study the formation of Pop III stars in these massive halos with simulations using the adaptive mesh refinement (AMR) code ENZO (Bryan et al., 2014). It is an Eulerian mesh-based hydrodynamic code that subdivides cubic cells into 8 smaller cells when certain refinement criteria are met. This allows the code to resolve regions of interest, while not wasting computation time on the large volumes outside of collapsed halos. ENZO includes various gas species - atomic hydrogen, ionized hydrogen, molecular hydrogen, helium etc. It also has multiple hydro solvers; we use the energy conserving, spatially third-order accurate Piecewise Parabolic Method (PPM) here. The code follows the non-equilibrium evolution of 9 species (H, H^+, He, He^+, He^{++}, e^-, H_2, H_2^+ and H^-) and includes radiative processes through the Grackle library (Smith et al., 2017). As the gas temperature in our simulations does not fall below 150 K, we do not expect HD cooling to play a significant role (McGreer & Bryan, 2008) and hence do not include it.

For this work, we run zoom-in cosmological simulations using a modified version of ENZO 2.5. We assume a ΛCDM cosmology consistent with Planck Collaboration et al. (2014) throughout: $\Omega_m = 0.32$, $\Omega_\Lambda = 0.68$, $\Omega_b = 0.049$, $h = 0.67$, $\sigma_8 = 0.83$, and $n_s = 0.96$. We

generate the initial conditions for our simulations using MUSIC (Hahn & Abel, 2013). To identify halos we run 3 sets of zoom-in simulations centered around 3 different halos from a cosmological box of comoving size $2\,h^{-1}$Mpc. We first run a dark-matter only simulation starting at redshift $z = 200$. We identify a halo in a redshift $z = 6$ snapshot and rerun the simulation with hydrodynamics using a refined region around the halo. The halos were selected such that they would be the most massive halo in the refined region, as we want the halo of interest to collapse first. We also make sure that the halo considered here is relatively far away from other similar mass halos. This is to avoid complications from tidal forces of neighboring massive halos. This may seem contradictory to our problem where we need a nearby Pop II star galaxy as a source of ionizing radiation; however, for simplicity, we wish to focus only on the collapsing halo in this work. Future work should aim for a more self-consistent simulation. Halo A was selected from a 128^3 dark matter only simulation with a virial mass of $1.3 \times 10^9\,M_\odot$ at z = 6. We rerun the hydro simulation with a 128^3 grid with 3 added (initial) refinement levels in the zoomed region, giving an effective initial resolution of 1024^3 in the zoomed region. For halos B and C, we select them in a 256^3 dark matter only simulation, so as to be able to select lower mass halos. Halos B and C have virial masses of $1.22 \times 10^8\,M_\odot$ and $3.2 \times 10^8\,M_\odot$. We then rerun hydro simulations zoomed around these halos with a 128^3 grid and 3 added initial refinement levels in the zoomed region. We choose the random seeds for the MUSIC initial condition generator such that the initial conditions are the same for the 256^3 grid dark matter only and 128^3 grid hydro runs. The dark matter particle mass was $836\,M_\odot$ in the zoomed region for all the simulation runs.

We refine the cells in the zoomed region into smaller cells based on the following criteria: baryon mass, dark matter mass and the Jeans length. We refine the cell if the baryon or dark matter density becomes higher than 4×2^{3l} times the corresponding densities on the root grid i.e. the coarsest grid (128^3) in the simulation and l is the refinement level, meaning that cells with more mass than 4 times the initial dark matter particle mass or baryon equivalent will be refined. The Jeans length is resolved by at least 16 cells, and generally controls the

refinement during the later parts of the collapse. Cells are refined down to 18 levels from the root grid, resulting in a best resolution of 0.085 pc comoving.

3.2.2 Ionization implementation

We treat hydrogen ionization radiation in the same way as Visbal et al. (2017). This treatment is based on Rahmati et al. (2013), which provided fitting functions to the photoionization rate as a function of local density that match cosmological simulations of the post-reionization universe with radiative transfer. We assume a uniform photoionzation rate in the box which is modified locally based on the self-shielding factor.

The hydrogen photoionization rate is given as

$$\Gamma = f_{\rm sh}\Gamma_{\rm bg}, \tag{3.1}$$

where $f_{\rm sh}$ is the local self-shielding factor and $\Gamma_{\rm bg}$ is the uniform ionizing background without shielding. The self-shielding factor depends on the temperature and density of hydrogen as

$$f_{\rm sh} = 0.98\left[1+\left(\frac{n_{\rm H}}{n_{\rm H,sh}}\right)^{1.64}\right]^{-2.28} + 0.02\left[1+\frac{n_{\rm H}}{n_{\rm H,sh}}\right]^{-0.84}, \tag{3.2}$$

where

$$n_{\rm H,sh} = 5\times10^{-3}\,{\rm cm}^{-3}\left(\frac{T}{10^4{\rm K}}\right)^{0.17}\left(\frac{\Gamma_{\rm bg}}{10^{-12}{\rm s}^{-1}}\right)^{2/3}. \tag{3.3}$$

We apply the same shielding factor to the hydrogen photo-heating rate as well. We assume a $T_* = 3\times10^4$K black-body spectrum for computing the relative ionization and heating rates for hydrogen.

We use an ionizing flux in units of $F_0 = 6.7\times10^6$ photons s^{-1} cm^{-2}, which is equivalent to having a source emitting 2×10^{54} ionizing photons isotropically at a distance of 50 kpc. According to merger-tree calculations in Visbal et al. (2016), a dark matter halo of mass $M = 6.6\times10^{11}\,{\rm M}_\odot$ at $z\sim7$, with star formation efficiency and escape fraction 0.1, will

produce 2×10^{53} photons per second over a range of redshift $\Delta z \approx 10$, which would correspond to flux of $0.1F_0$ if the source were at a distance of 50 kpc. We do not self-consistently model this source within the box; as discussed later in this chapter, and in more detail in (Visbal et al., 2016), the detailed setup is quite rare and would require a much larger cosmological volume to model self-consistently. In particular, by doing this, we assume that the only impact of the source is radiative.

Ideally, one should ray-trace the photons from the ionizing source to correctly simulate the problem. Visbal et al. (2017) show that the results do not vary significantly if we use an ionization treatment based on Rahmati et al. (2013) instead of ray-tracing photons from an actual source. It is however computationally far less expensive. Hence, we use a uniform and isotropic radiation field (corrected for local extinction) in this work. Some unintended effects of this will be discussed below.

Visbal et al. (2017) showed that the redshift at which ionizing radiation is turned on does not have a large effect on the results, as long as there is enough time for the intergalactic medium to be ionized completely. We start the background ionizing radiation at redshift $z = 30$.

We include a uniform LW background radiation with flux $J_{\rm LW} = 100\times J_{21}$ such that the H_2 photo-dissociation rate $k_{\rm H_2} = 1.42\times10^{-12}J_{\rm LW}/J_{21}{\rm s}^{-1}$. J_{21} here is $10^{-21}{\rm ergs}^{-1}{\rm cm}^{-2}{\rm Hz}^{-1}{\rm Sr}^{-1}$. When ionizing radiation is present, we increase the LW radiation assuming a black-body spectrum corresponding to a temperature of 30,000 K. For ionizing flux F_0, the total LW background flux is $J_{\rm LW} = 175 \times J_{21}$. We modify the photo-dissociation rate by the self-shielding function described in Wolcott-Green et al. (2011).

Our choice of background intensity $J_{\rm LW} = 100J_{21}$, represents what could be found in an overdense region of the Universe (see e.g. Figure 11 in Ahn et al., 2009b). When ionizing radiation from a nearby galaxy is present, we increase the LW radiation as $J_{\rm LW} = (100 + 75 \times F/F_0)J_{21}$, where F is the ionizing flux. This value of the flux assumes the source is a 30,000 K blackbody with an escape fraction in ionizing photons of $f_{\rm esc} \approx 0.2$

3.2.3 Fragment mass and sink particle implementation

We define runaway collapse as the time when the simulation reaches the highest refinement level 18. Continuing the simulation further without refining cells leads to artificial fragmentation (Truelove et al., 1997). To continue the simulation after the runaway collapse, we first used the *MinimumPressureSupport* parameter in ENZO (Machacek et al., 2001). This parameter adds artificial pressure to the most refined cell so that the Jeans length of the most refined cell is resolved by the square root of the *MinimumPressureSupport* number of cells. We set the *MinimumPressureSupport* to 256 to make it consistent with the Jeans refinement parameter of 16 used. We then used YT's (Turk et al., 2011) clump finder to identify clumps at various times. While useful, the clump finder in YT does not connect clumps across snapshots and so returns different locations and properties for clumps in snapshots at different times. Hence, we cannot use the information from the clump finder to accurately find out how particular clumps are evolving in time.

Therefore, in addition to the above estimates, we also used a simple sink particle technique to determine the accretion rates and clump mass evolution. Sink particles have been previously used for simulating first stars in SPH codes (e.g., Stacy et al., 2010, 2012; Greif et al., 2012) and grid-based codes (e.g., Krumholz et al., 2004). The evolution of the protostars depends on the accretion rates onto them. To estimate accretion rates this way, we reran the simulation and used a sink particle implementation in ENZO (instead of the *MinimumPressureSupport* technique described above). When reaching the highest refinement level, we add a sink particle to the most refined cell. This sink particle accretes mass from the cells around it such that the maximum density of any cell in a sphere of radius 5 cell widths is no higher than the density which would exceed the refinement criterion on that (maximum) level of refinement. This insures that the minimum density is accreted such that the Jeans length criterion is not violated, avoiding artificial fragmentation. By comparing the mass of the sink particles at various snapshots, we can calculate their accretion rates, which can be used to estimate the final stellar masses. We merge two sink particles into

one if the distance between them is less than 10 times the width of the smallest cell. The gravitational force on sink particles is calculated at the highest refinement level (i.e. it is not smoothed). More sophisticated sink particle algorithms are possible (e.g., Regan & Downes, 2018b), and recent work (Regan & Downes, 2018a) has explored the fragmentation of atomic cooling halos exposed to a LW background (without the ionizing background adopted here).

3.3 Results

3.3.1 Collapse properties

Collapse is delayed to lower and lower redshifts for increasing background flux values. The collapse occurs when the cooling time and the dynamical time rapidly decrease and the heating time rapidly increases, marking the runaway collapse.

We can understand the physics of the collapse by looking at Figure 3.1. The top panel shows the cooling, heating and dynamical times for the central region of halo A as a function of redshift for a background ionizing flux equal to F_0 and the bottom panel shows H density, H I density and H_2 density as a function of the redshift for the same halo. The background ionizing radiation is turned on at redshift 30, which starts the ionization and heating of the gas. This also decreases the cooling time significantly, as the atomic cooling is most efficient near the temperature of 10^4 K. With time, more gas in the central region gets ionized and we can see that the ionization reaches a peak near redshift $z = 18$. As the potential well of the dark matter halo gets deeper and gas density increases, the gas is able to self-shield itself better from the background radiation. The runaway collapse occurs when the dynamical time and the cooling time become much shorter and cross the heating time which increases rapidly.

As shown in Visbal et al. (2017), the collapse of the halo is delayed further with increasing background ionizing flux. The delays in redshift for a given change of background flux are different for different halos. In particular, halo B does not collapse untill redshift $z = 5$ for background flux higher than $0.01F_0$. This issue is discussed more in section 3.4.

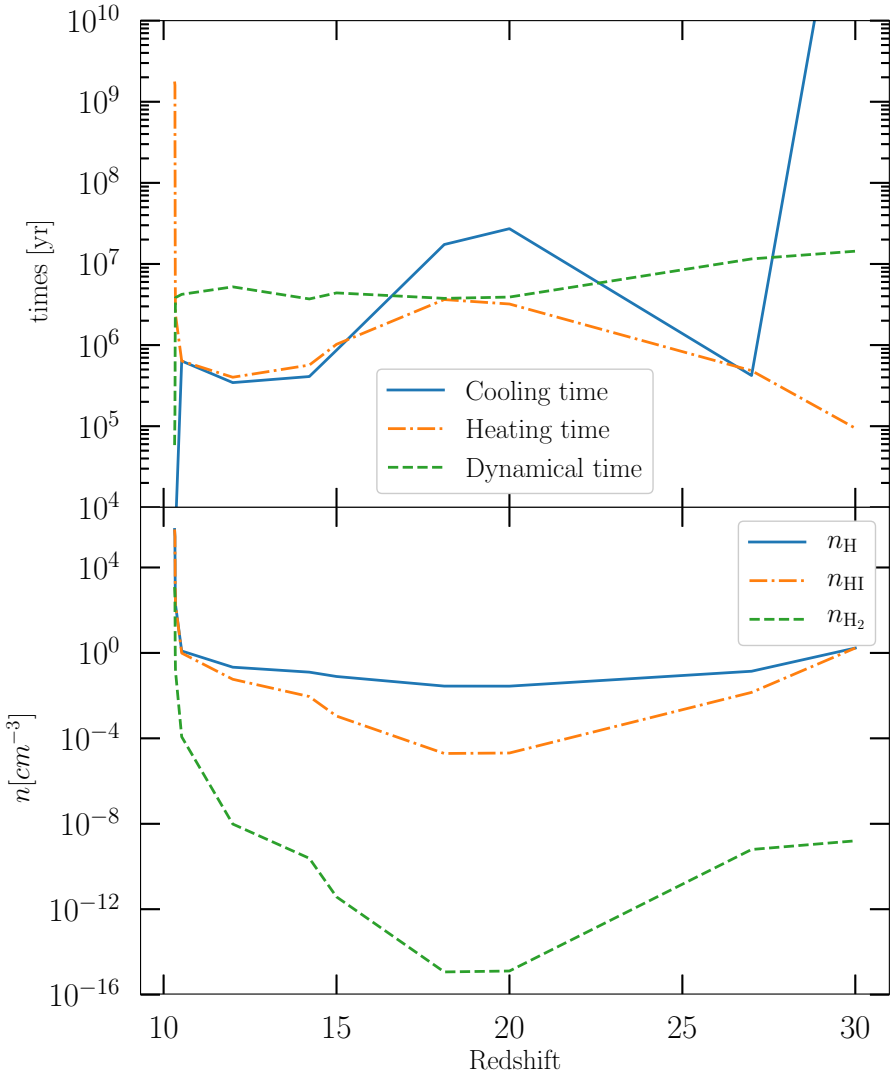

Figure 3.1: Important timescales and densities in the central region of halo A for background flux F_0 as a function of redshift. The top panel shows the cooling, heating and dynamical times in the center of the halo as a function of redshift. The bottom panel shows the densities of the total, neutral and molecular hydrogen densities in the same region. At the point of runaway collapse, the densities increase rapidly which coincides with rapidly falling dynamical and cooling times, and a rapidly increasing heating time.

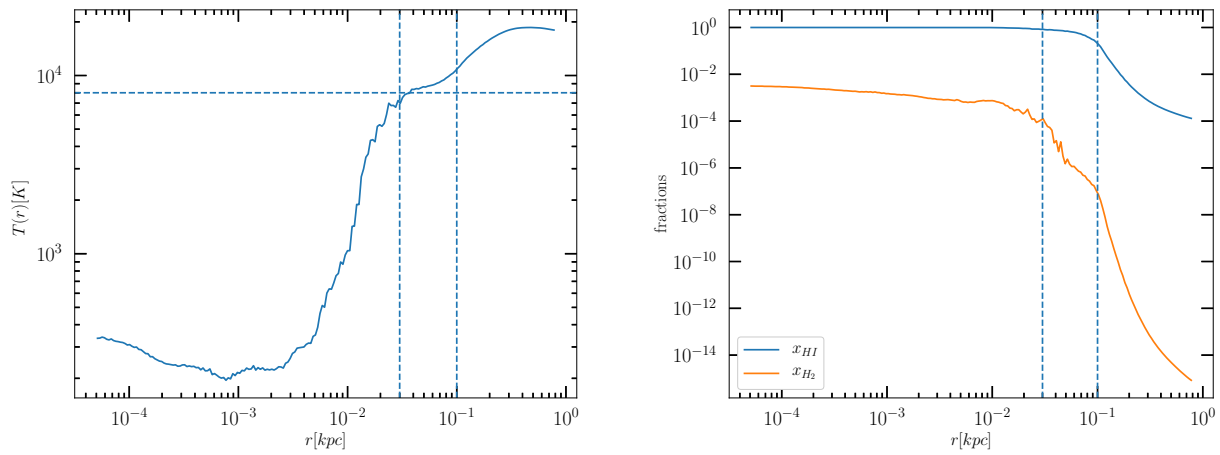

Figure 3.2: Radial profiles of the gas temperature (left) and the neutral and molecular hydrogen fractions (right) for halo A at the point of runaway collapse with a background flux F_0 at $z = 10.33$. In the right panel, we can see that the gas forms a core of molecular hydrogen of radius ~ 30 pc and a neutral core of radius ~ 100 pc (shown with vertical blue dashed lines in both plots). This is consistent with the temperature profile in the left panel where $T < 10^4$ K for $r < 30$ pc because of the molecular hydrogen cooling, $T \sim 10^4$ K for $30\,\mathrm{pc} < r < 100\,\mathrm{pc}$ because of atomic cooling and $T > 10^4$ K for $r > 100$ pc because of the ionizing radiation. The horizontal blue dashed line in the temperature profile corresponds to a temperature of 8×10^3 K.

3.3.2 Radial profiles

The radial gas density profile at the runaway collapse follows an r^{-2} profile consistent with an isothermal profile (Larson, 1969) for all halos. The denser gas in the center can self-shield itself from the background ionizing flux and forms a neutral core. In our simulations, this is reflected through the lower value of the local f_{sh} factor at high densities which reduces the effective ionizing radiation strength as shown in Eq. 3.1. Figure 3.2 shows the temperature as a function of radius in the left panel and the averaged neutral and molecular hydrogen fractions as a function of radius in the right panel, for halo A at the point of runaway collapse for a background flux F_0 at $z = 10.33$. We see a neutral core of size ~ 100 pc and also a smaller core of ~ 30 pc with high molecular hydrogen fraction. These length scales can also be traced in the temperature profile on the left. The temperature of the ionized gas outside 100 pc is higher than 10^4 K because of the background ionizing radiation. In the region from

$r = 30 - 100$ pc, the gas cools via H electronic transitions and hence has a temperature close to 10^4 K. The gas within 30 pc from the center is cooled mostly via rotational-vibrational transition lines of molecular hydrogen and hence the temperature falls from 10^4 K to a few hundred Kelvin. In all of our halos, we see similar temperature profiles which include ionized gas in the outer parts of the halo and cold gas in the self-shielded cores in the centers.

3.3.3 Sink/clump accretion

In this subsection, we explain the properties of the sinks formed and their accretion histories.

The left panel of Figure 3.3 shows the projected density along x-axis for halo A at runaway collapse with background flux F_0 at $z = 10.33$. The contours show the clumps identified by YT's clump finder. The mass of the central dense clump grows as $10^{-3}\,\mathrm{M_\odot yr^{-1}}$. We also calculate accretion on the sphere of radius 1 pc centered around the densest point in the halo as the rate of change of the enclosed mass which is also consistent with the accretion rate of $10^{-3}\,\mathrm{M_\odot yr^{-1}}$.

Sink particles give us a better handle on the accretion rates on protostars not just at the center, but also forming at other locations as explained in the Section 3.2.3.

The accretion rate on to the sink particles are consistent with the expected rate based on the gas temperature, given by $\dot{M} = c_s^3/G$, where c_s is the sound speed and G is the Gravitational constant. This low accretion rate may initially be surprising given that the halo mass is quite large; however, we point out that, due to the self-shielding core, the collapse occurs in what is effectively a low-radiation environment, and the gas cools down to ~ 500 K. The resulting density and temperature structure of the fragmenting clumps appear to be very similar to that produced by the collapse of minihalos. Indeed, that the accretion rates we determine are roughly consistent with those in Regan & Downes (2018b), for similar LW backgrounds.

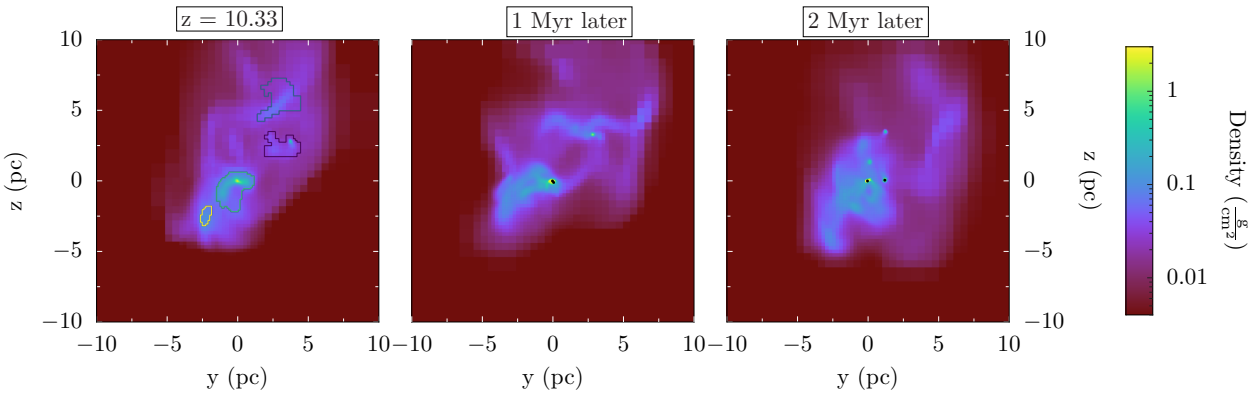

Figure 3.3: Projected densities along x-axis for halo A for the background flux F_0 at the runaway collapse at z = 10.33 (left panel), 1 Myr after the runaway collapse (middle) and 2 Myr after the runaway collapse (right). In the left panel, the contours show the clumps identified by YT's clump finder. The middle and right panels show the location of sink particles formed with black dots.

3.3.3.1 Halo A

We evolve our simulation after the runaway collapse for the background flux of the F_0 case. Even though YT's clump finder identifies 4 clumps at the runaway collapse, not all of them form sink particles at the same time as they have not reached the highest refinement level. At runaway collapse, a sink particle is formed at the densest point in the halo which is at the center in the left panel of Figure 3.3. The middle and the right panels of Figure 3.3 show projected densities at 1 Myr and 2 Myr after the runaway collapse, respectively. Black dots denote the location of the sink particle formed. Nearly 2 Myr after the start of runaway collapse, another clump becomes dense enough to form a sink particle, which can be seen in the right panel of Figure 3.3.

The mass of the most massive sink particle and its accretion rate as function of time is shown in the left panels of Figures 3.4.

3.3.3.2 Halo B

The gas in halo B does not collapse for any background flux equal to or higher than $0.03F_0$. The reasons for this happens are discussed in the discussion section 3.4.1. We select

the halo with the highest background ionizing flux for which gas still undergoes runaway collapse ($F = 0.01F_0$ in this case) to continue its evolution further in time. We add a sink particle in the densest cell at the point of runaway collapse. The total mass and accretion rate of that sink particle are shown in the middle panels of Figure 3.4.

3.3.3.3 Halo C

For halo C, we chose the case with $F = 0.1F_0$ to evolve further after runaway collapse. The runaway collapse occurs at $z = 6.54$. This is the halo in our simulations that shows the most fragmentation. We see multiple clumps forming with possible sites for the formation of sink particles. The left, middle and right panel of Figure 3.5 show projected densities at the point of runaway collapse, and 1 and 2 Myr after the runaway collapse, respectively. In the middle panel, we see 3 sink particles in the densest clumps. In the right panel, we see that some of the sink particles have drifted a bit from the clump in which they formed.

The accretion histories of the three most massive sink particles are shown in the right panels of Figure 3.4. The most massive sink particle accretes with a rate as high as $0.02\,\mathrm{M}_\odot\mathrm{yr}^{-1}$.

3.3.4 Stellar mass estimates

In this subsection, we describe how sink particles are used to estimate the corresponding mass of Pop III stars. Sink particles accrete mass from cells around them and grow in mass. The sink particle routine does not include any radiative feedback from the protostar that would lower the accretion rate and the final mass of the Pop III star formed.

Hirano et al. (2014) studied the evolution of Pop III protostars and their final masses including the relevant stellar physics for a sample of 100 first stars. Their sample is about Pop III star formation in minihalos that mostly form individual stars, a different environment from one we are studying here, however we expect that with similar accretion rates, the feedback impact for gas close to the star would not change. From their large sample, they find a linear relation between accretion rate on the protostar and the final mass of the Pop

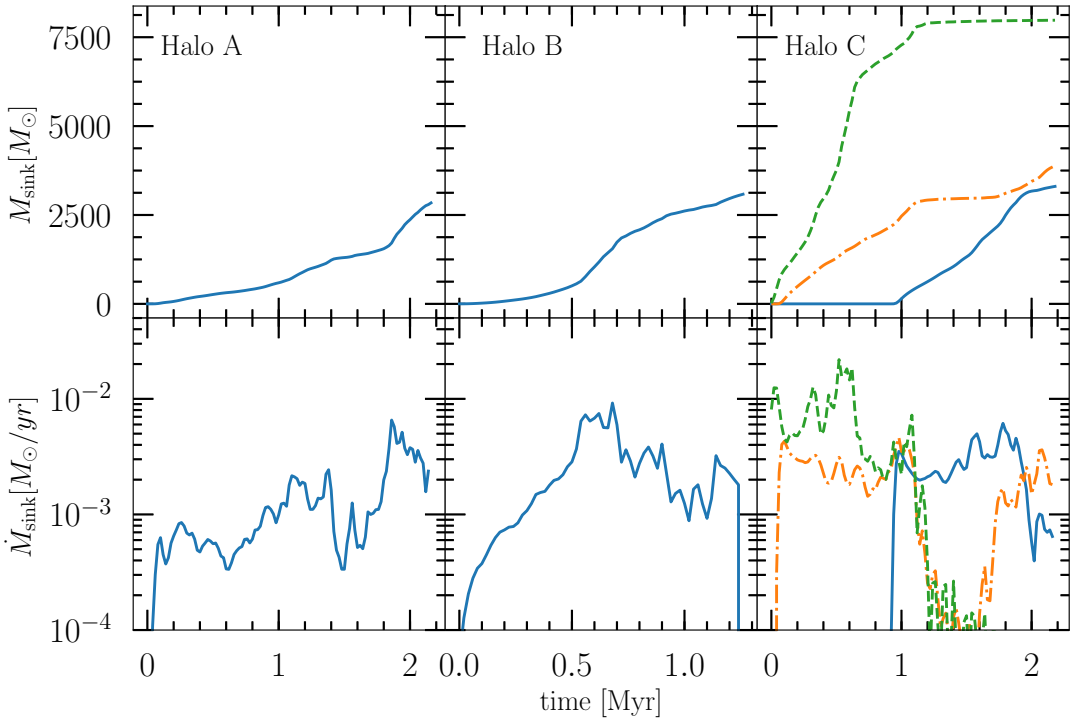

Figure 3.4: The left, central and right panels show the evolution of sink particles for the halos A, B and C respectively. The top panels show the total mass accreted by the sink particles as a function of time. For halo C, it shows the accretion history of the 3 most massive sink particles in the simulation. In the absence of proto-stellar feedback, the mass of the sink particle does represent the mass of the final star formed. The corresponding stellar masses can be estimated using the accretion rate of the sink particle (shown in the bottom panels) and a fitting function given by Hirano et al. (2014). Based on the fit, we estimate the stellar masses for the sinks shown to be $\sim 40\,\mathrm{M}_\odot$ for halo A, $\sim 100\,\mathrm{M}_\odot$ for halo B and 600, 100, 100 $\mathrm{M}_\odot$ for halo C. As all the sink particles have accretion rates lower than $\dot{\mathrm{M}}_{\rm crit} = 0.04\,\mathrm{M}_\odot$ (Hirano et al., 2014), we do not expect any of the sinks to form high mass ($M > 10^4$ $\mathrm{M}_\odot$ black hole seeds.

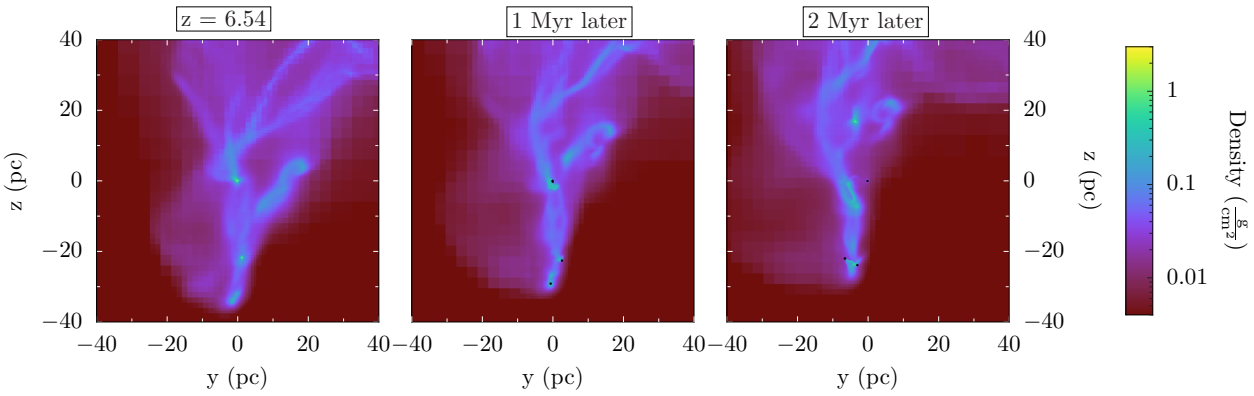

Figure 3.5: Projected densities along the x-axis for halo C for the background flux $0.1F_0$ at the runaway collapse at z = 6.54 (left panel), 1 Myr after the runaway collapse (middle) and 2 Myr after the runaway collapse (right). The black dots in the middle and right panels show the locations of sink particles formed. Accretion histories of the sink particle are shown in Figure 3.4.

III star given as

$$M_{\rm PopIII} = 100 M_\odot \left(\frac{\dot{M}}{2.8 \times 10^{-3} M_\odot {\rm yr}^{-1}} \right). \tag{3.4}$$

Although the accretion rate is defined as the accretion on the cloud and not the sink particle, we assume that both of these accretion rates do not differ significantly and use the accretion rate of the sink particle to calculate the stellar mass. The estimated masses for sink particles in halo A and B are $40\,{\rm M}_\odot$ and $100\,{\rm M}_\odot$ respectively. For halo C, the most massive clump would correspond to a stellar mass of $600\,{\rm M}_\odot$ and the other two sink particles to approximately $100\,{\rm M}_\odot$ each. No other sink particles are formed.

Note that, according to Haemmerlé et al. (2018), the critical accretion rate for the formation of the (high mass) direct collapse black holes could be lower than previously expected. Their calculations suggest an $\dot{\rm M}_{\rm crit}$ below $0.01\,{\rm M}_\odot{\rm yr}^{-1}$ rather than the previously suggested $0.05\,{\rm M}_\odot{\rm yr}^{-1}$. In this scenario, the central most massive sink particle for halo C could be a direct collapse black hole.

3.3.5 Resolution tests

During the collapse stage, the resolution is primarily controlled by our Jeans refinement parameter (as opposed to the gas or dark matter Lagrangian refinement criteria). To explore the impact of varying spatial resolution, we varied the Jeans refinement parameter from 16 to 32 in halo A. The resulting collapse redshift, profile, and overall properties were very similar with the lower-resolution result (although turbulent substructure was better resolved).[2] Because of this similarity, we used Jeans refinement parameter equal to 16 (note that these are both larger than the factor of 4 suggested in the Truelove et al. (1997) paper).

We also checked the effect of resolution on the evolution of the sink particle. For halo C, we did a run where we added the sink particle when the simulation reaches 20 levels of refinement, instead of 18 in the default run. (i.e. 4 times better resolution than the default run.) The accretion histories of the sink particles are similar at early times and show a small difference at the late times. However, as the final mass of the Pop III star depends on the accretion rate rate at early times, the properties of the stars and effect of the feedback does not vary much with increased resolution. This is consistent with Regan & Downes (2018a), who found little signs of fragmentation for a similar, relatively high, LW radiative background.

3.4 Discussion

3.4.1 Collapse criterion

As seen in the previous section, collapse can be delayed to much later times and higher virial mass for strong background ionizing fluxes. Visbal et al. (2017) also show that for very high background flux, the virial mass at the collapse reaches a saturation value, typically

[2]We had to change the starting time of the ionizing radiation to $z = 35$ in the higher-resolution case, otherwise, we found that a minihalo collapse was trigged at $z = 30$ simply by turning on the radiation. This occurred because of the (unrealistically) isotropic nature of the uniform background, and was also seen in Visbal et al. (2017). A better fix would be to include non-isotropic radiative transfer, but we found that a simple tweak of the initial redshift avoided this pathological situation.

about an order of magnitude higher than the atomic cooling threshold. At what background flux is the saturation reached, if reached, depends on the halo properties and history.

For halos A and C, the amount of cold-dense gas and number of clumps at the times of runaway collapse first increases and then decreases with increasing background flux. For low ionizing flux, increasing the background flux delays the collapse and increases the virial mass and the mass of cold-dense gas at the collapse. For high ionizing flux, increasing the background flux does not increase the halo mass at collapse significantly, but decreases the size of the cold neutral core because of stronger ionization. The number of clumps identified using YT at the runaway collapse also follows a similar pattern. Thus, for a given halo, a particular value of the background flux gives the highest mass of cold-dense gas and the highest number of clumps at the runaway collapse. For halos A and C, we continued the simulation after the runaway collapse for those background fluxes with highest number of fragments. This may represent the most Pop III stars that could form in these halos.

In the case of halo B, it collapses for flux $0.001F_0$ and $0.01F_0$. However, for flux equal to or higher than $0.03F_0$, the gas in the halo does not collapse at all (untill redshift 5). The central gas densities in these cases do not seem to increase with time, as it happens in the cases where gas collapses. In some cases, densities even continue to decrease. For halo B, we do not get a saturation background flux value, on the other hand the halo does not collapse at all for high background fluxes.

To be able to predict whether a halo with a given background flux will collapse or not, and at what redshift, we investigated the halo merger history. We generated a dark matter halo merger tree using ROCKSTAR (Behroozi et al., 2013a) and CONSISTENT-TREES (Behroozi et al., 2013b). Figure 3.6 shows the virial mass of main progenitors. Progenitors for halos A and C continue to grow all the way till redshift 6, whereas halo B does not grow after redshift 8. Halo B collapses at redshift 8.85 for the background flux of $F = 0.01F_0$. For higher ionizing fluxes, halo B does not collapse as it is not able to self-shield because of its stalled growth at low redshift. From our small of sample of 3 halos, we speculate that

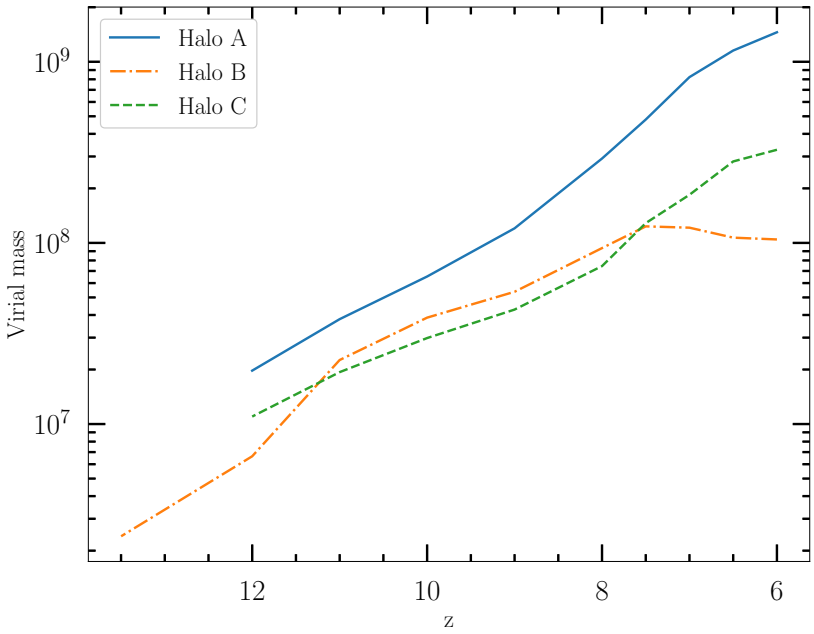

Figure 3.6: Virial mass of the main progenitors of the 3 halos selected with redshift. Halo A and halo C continue to grow untill redshift 6, whereas halo B does not grow after redshift 8. We find that for high ionizing flux halo B does not collapse.

this is the most important reason why gas in halo B does not collapse for high background fluxes. To confirm this hypothesis, we would need do more simulations, particularly ones with stalled halos.

3.4.2 Feedback from stars

Ionizing radiation from the Pop III stars formed would create an HII region around it and also drive an ionization shock. The growth of the HII region and the shock affects the formation of other Pop III stars. We do not include any feedback from the protostar or star in our simulation. To estimate effect of the feedback from the first star formed on the formation of other stars, we estimate the growth of ionization front and shock associated with it using analytic calculations. We give an outline of these calculations using halo C as an example, as this is the halo that has the highest clumpiness and multiple sink particles.

The star corresponding to the central most massive sink particle would have a mass of

$\sim 600\,\mathrm{M}_\odot$. According to Schaerer (2002), this star would emit ionizing photons at a rate of $7.8 \times 10^{50}\,\mathrm{s}^{-1}$. The radial profile of gas density can be well approximated as $n_0(r/r_c)^{-2}$, consistent with the isothermal density profile, with $n_0 = 1.04 \times 10^6\,\mathrm{cm}^{-3}$ and $r_c = 0.1\,\mathrm{pc}$ for $r > r_c$ and n_0 for $r < r_c$. We assume that the shock moves out with a velocity of ~ 10 km/s.

The HII region will grow as

$$4\pi R^2 n(R) dR = \left(\dot{N}_{ion} - 4\pi\alpha \int_0^R n^2(r) r^2 dr \right) dt. \tag{3.5}$$

The right hand side denotes the number of available ionizing photons per unit time and α is the recombination rate B coefficient at $T = 10^4$ K.

Assuming a static density profile mentioned above gives

$$\frac{dR}{dt} = \frac{\dot{N}_{ion}}{4\pi n_0 r_c^2} - \alpha n_0 r_c \left[\frac{4}{3} - \frac{r_c}{R} \right]. \tag{3.6}$$

Initially dR/dt is small, so the evolution of the ionization front is governed by the shock which proceeds as D-type shock just ahead of the ionization front.

As the shock moves forward, the density of the gas in the shocked region decreases. Assuming that the shape of density remains unchanged, the corresponding inner density n_0 decreases as $n_0 = \tilde{n}_0(\tilde{r}_c^2/r_c^2)$, where $\tilde{n}_0$ and $\tilde{r}_c$ are the initial values of n_0 and r_c. With these substitutions, dR/dt becomes faster than the shock front at

$$r_c = \frac{4\pi\alpha \tilde{n}_0^2 \tilde{r}_c^4}{3\dot{N}}. \tag{3.7}$$

This is where the ionization front starts to lead ahead of the shock and the shock front changes from D-type to R-type. (Franco et al., 1990; Whalen et al., 2004; Kitayama et al., 2004; Alvarez et al., 2006) For the given parameters, this happens at $r_c = 4.7$ pc.

For a given density distribution, we can define a critical ionizing photons rate $\dot{N}_{\mathrm{crit}}$ such

that if $\dot{N} > \dot{N}_{\rm crit}$, all gas would be ionized, as follows

$$\dot{N}_{crit} = \frac{16\pi\alpha\tilde{n_0}^2\tilde{r_c}^4}{3r_c}. \tag{3.8}$$

For $\dot{N} = 7.8 \times 10^{50}$ ionizing photons $\rm s^{-1}$, this happens when $r_c \sim 19\,\rm pc$. When the shock front has reached between 4.7 pc and 19 pc, the ionization front leads ahead of the shock, but only by a small distance.

Until reaching 19 pc, the growth of the ionization front is dictated by the growth of the shock. Assuming a shock velocity of 10 km/s, the shock would take nearly 2 Myr to reach 19 pc. After this the ionization front would move very rapidly outwards. This would mean that the formation of two other sink particles at distance $\sim 20\,\rm pc$, would not be affected by the growth of the HII region from the first star, as they form within 1 Myr after the first star. If the shock speed is as high as 30 km/s as Whalen et al. (2004) suggest, the shock would take ~ 3 times shorter time.

For halo C, we also see few dense clumps that have not formed a sink particle yet. A clump of diameter 1 pc and density $10^4\,\rm cm^{-3}$ would have high recombination rate to be ionized completely if it is within $10 - 20$ pc from the center. Such a clump may collapse or be destroyed when the shock front reaches it. If collapse of such clump is triggered, then we may have more star formation fuelled by the radiative feedback from the first star.

The stars formed will also emit LW radiation along with the ionizing radiation. The LW radiation is optically thin and travels close to the speed of light. We estimate the number of LW photons emitted by the first star formed using Schaerer (2002) which corresponds to a LW flux of $\sim 10^5 \rm J_{21}$ at a distance of 20 pc. Of the two other sink particles that form at a distance of $\sim 20\,\rm pc$ from the first sink particle, one forms soon after the first sink, whereas the other one forms nearly 1 Myr later. We expect that the LW radiation from the first star will not affect the evolution of the second star formed, but would alter the evolution of the third sink particle. As $J_{\rm LW}$ of $10^5 J_{21}$ is higher than $J_{\rm crit}$, most of the molecular hydrogen

at the location of the third sink particle would be destroyed and the gas temperature would raise to $\sim 10^4$ K increasing the accretion rate as well. If the accretion onto the third sink particle continues for long time, it may turn into a DCBH, however it is hard to predict if that would happen here.

3.4.3 Observing with JWST

Zackrisson et al. (2011) computed that a Pop III galaxy with a stellar mass of $\sim 3 \times 10^4\,\mathrm{M}_\odot$ and few times $10^5\,\mathrm{M}_\odot$ could be detected at $z = 6$ with maximal and no nebular emission respectively with an integration time of 100 hours. The limits decrease as $t_{\rm obs}^{-1/2}$. This estimate is based on the spectral analysis code YGGDRASIL that can identify Pop III galaxies using photometry based on the presence of strong hydrogen and helium lines and the absence of strong metal lines (e.g. O II, O III, S III).

Here we find that for the halos we simulated, even ones with large fragmentation do not produce enough stars to be observed in this limit. For halo C, we estimate a total stellar mass of $\sim 10^3\,\mathrm{M}_\odot$ which is smaller than the detection limit by an order of magnitude. Visbal et al. (2017) estimate that if all star formation in suppressed in halos up to $10^9 M_\odot$, we would get a comoving number density of $10^{-7}\mathrm{Mpc}^{-3}$ which corresponds to 0.002 per JWST field of view per unit redshift at $z = 6$. Thus, both in terms of brightness and their abundances, Pop III galaxies would be unlikely to be detected in an ultra deep field with JWST. A better strategy would be to look near massive galaxies which would be the source for the ionizing photons to create Pop III galaxies in lensed fields. Another possible strategy would be to look for Pop III galaxies forming in atomic cooling halos exposed to just LW photons at lower redshifts as they would have higher abundances.

3.5 Summary and Conclusion

We performed zoom-in simulations around 3 different halos for various background ionizing fluxes with runaway collapse at $z = 6 - 15$. Our main conclusions can be summarized

as follows.

1. Pop III star formation can be suppressed to much lower redshifts in the presence of ionizing radiation from a nearby galaxy. The collapse finally occurs when the gas is able to self-shield itself from the background radiation.

2. For very high background ionizing flux, the virial mass at collapse can be up to an order of magnitude higher than the atomic cooling threshold. For a given halo, the amount of cold-dense gas first increases, reaches a maximum value and then decreases with increasing background flux. A similar pattern can be seen in the number of clumps formed at the runaway collapse. The location of the peak would depend on the halo history. For a halo that does not grow at all over a large redshift range, increasing the background flux may photo-evaporate the gas and prevent collapse.

3. We use YT's clump finder and a sink particle implementation in ENZO to study fragmentation in these Pop III galaxies. Based on their accretion rates, the estimated masses of the Pop III stars range from $40 - 600$ $\mathrm{M}_{\odot}$.

4. The most interesting point about these systems is their possible observability with upcoming telescopes such as the James Webb Space Telescope. Halos with pristine gas that are exposed to ionizing radiation would be some of the most massive and late forming galaxies with Pop III stars. In our simulations, we form a handful of Pop III stars in the first 2 Myr. The star formation transitions from Pop III to Pop II when a star explodes as a type II supernova ($M_* < 40\,\mathrm{M}_{\odot}$) or as a pair-instability supernova ($140\,\mathrm{M}_{\odot} < M_* < 250\,\mathrm{M}_{\odot}$) (Greif, 2015). With low star formation efficiency, the most massive galaxy in our simulations has $\sim 10^3\,\mathrm{M}_{\odot}$ in stellar mass at $z = 6.54$ which is an order of magnitude lower than the detection limits for an ultra-deep observation using JWST. We therefore conclude that it would be very unlikely to detect such massive late-forming Pop III galaxies with JWST ultra-deep observations and a better strategy could be to look for them in the lensed fields.

Chapter 4: Formation of the first stars and galaxies in a fuzzy dark matter cosmology

4.1 Introduction

The standard model of cosmology includes dark matter in form of "cold" dark matter and dark energy in the form of a cosmological constant. This model has been immensely successful in explaining the statistics of the cosmic microwave background, the large-scale structure in the universe, and cluster abundances (Bennett et al., 2013). Over the last few decades, some apparent inconsistencies have been pointed out between the standard model and observations of the small-scale structure in the universe. A serious concern called "missing satellite problem" (Klypin et al., 1999) refers to the fact that the number of satellite galaxies for a Milky-Way mass galaxy appears to be about an order of magnitude smaller than the number predicted based on satellite halos from N-body simulations. This problem is sharpened by the "too big to fail" problem which claims that some of the predicted satellites are so massive that it is impossible for them to not have any stars (Boylan-Kolchin et al., 2011). The Navarro-Frenk-White (NFW) profile of the dark matter density in ΛCDM halos from N-body simulations has a cusp ($\propto r^{-1}$) near the center (Navarro et al., 1997), whereas many observations of nearby dwarf galaxies suggest a cored profile for dark matter density (Burkert, 1995; Goerdt et al., 2006). It has also been claimed that the dynamical friction because of dark matter in the dwarf spheroidal galaxies would have caused the globular clusters to spiral towards and merge with the central galaxy before the present time (Tremaine, 1976).

One type of solution to these small-scale problems is to include the effects of baryonic physics in the simulations more accurately to see if these problems are alleviated. The

feedback from the central black hole and supernovae can flatten the density profile in the center for many halos (Del Popolo et al., 2014; Oñorbe et al., 2015; Chan et al., 2015). The missing satellite problem can be alleviated to a degree with a combination of mergers, tidal stripping, and ionizing radiation (Simon & Geha, 2007; Brooks et al., 2013).

Another type of solution involves proposing an alternate candidate for the dark matter such as the warm dark matter (WDM) or the fuzzy dark matter (FDM). These models suppress the small-scale structure of dark matter which results in a low-mass end cutoff for the dark matter halo mass function. Warm dark matter is made up of particles with mass $\sim$ keV which remain relativistic for a longer time than CDM. Its thermal velocity wipes out small-scale structure, an effect also known as free-streaming (Bode et al., 2001; Schneider et al., 2013).

The fuzzy dark matter is made up of ultra-light axions of mass $\sim 10^{-22}$ eV. Its extremely small mass makes its de Broglie wavelength of the order of kpc and relevant on astrophysical scales (Hu et al., 2000; Marsh, 2016; Hui et al., 2017). This results in a small-scale cutoff in the matter power spectrum. The fuzzy dark matter has a non-zero quantum pressure and therefore an effective sound speed given as

$$c_{s,eff}^2 = k^2/4a^2m_a^2, \tag{4.1}$$

where k is the comoving wavenumber, a is the scale factor, and m_a is the mass of the ultra-light axion. The presence of this quantum pressure results in a Jeans scale for the fuzzy dark matter, such that only perturbations on scales larger than it grow under the influence of gravity. The Jeans scale is given as

$$k_J = 66.5a^{1/4}\left(\frac{\Omega_a h^2}{0.12}\right)^{1/4}\left(\frac{m}{10^{-22}eV}\right)^{1/2}\text{kpc}^{-1}, \tag{4.2}$$

(Marsh, 2016). A corresponding Jeans mass can be defined as

$$M_J = \frac{4\pi}{3}\rho_0 \left(\frac{\pi}{k_J}\right)^3 \propto a^{-3/4} m^{-3/2}. \tag{4.3}$$

The Jeans mass at $z = 0$ is $\sim 2 \times 10^7\,\mathrm{M}_\odot$. The existence of a Jeans mass for FDM combined with the small-scale cutoff in the power spectrum results in a low-mass cutoff for the halo mass function.

In ΛCDM, the first stars are expected to form in minihalos of mass $\sim 10^5 - 10^7\,\mathrm{M}_\odot$ at $z = 30$ onwards (Haiman et al., 1996; Tegmark et al., 1997; Machacek et al., 2001; Abel et al., 2002). In the absence of such low-mass halos, the first stars are expected to form at much lower redshift and in much more massive halos. As early galaxy formation is significantly delayed in a fuzzy dark matter cosmology, observations of high-redshift galaxies coupled with accurate numerical predictions for their properties might be the best way to constrain the properties of FDM. The *Roman Space Telescope* (formerly *WFIRST*) High Latitude Survey is expected to observe many $z \sim 10$ galaxies (Spergel et al., 2013; Waters et al., 2016), which can be studied in detail with the *James Webb Space Telescope (JWST)*. The *JWST* is also expected to measure the faint-end of the UV luminosity function at high redshift, which can also be used to constrain the properties of the fuzzy dark matter (Corasaniti et al., 2017; Ni et al., 2019). Thus, in this work, we aim to study the properties of first stars and first galaxies forming with high-resolution simulations for FDM.

This chapter is structured as follows. In Section 4.2, we describe our simulation set-up and the method we have used to accurately evolve FDM. In Section 4.3, we describe the properties of the collapsed dark matter halo and the structure of the dense star-forming region in it. In Section 4.4, we describe a simple prescription we have used for star formation and ionization feedback. We summarize our results in Section 4.5.

4.2 Simulation set-up

We perform our cosmological simulations using the adaptive mesh refinement (AMR) code ENZO (Bryan et al., 2014; Brummel-Smith et al., 2019). ENZO accurately evolves the distribution and growth of fuzzy dark matter using the Schrödinger-Poisson equations (Li et al., 2019). We define the scalar field ψ, often called as the wave function, in each cell and evolve it using the Schrödinger equation as

$$i\hbar\left(\partial_t\psi + \frac{3}{2}H\psi\right) = \left(-\frac{\hbar^2}{2ma^2}\nabla^2 + m\Phi\right)\psi. \tag{4.4}$$

Here t is proper time, ∇ is gradient with respect to comoving coordinates, a is the scale factor, H is the Hubble parameter and Φ is the gravitational potential, which obeys the Poisson equation:

$$\nabla^2\Phi = 4\pi G a^2\bar{\rho}\delta, \tag{4.5}$$

where $\bar{\rho}$ is the cosmic mean mass density and δ is the overdensity. The fuzzy dark matter density is related with the wave function as

$$\rho = m|\psi|^2. \tag{4.6}$$

The Schrödinger-Poisson equations can be represented using the fluid-like equations with the Madelung formulation (Madelung, 1927). In this formulation, the wave function ψ is related to the fluid mass density ρ and the fluid velocity $\mathbf{v}$ as follows:

$$\psi \equiv \sqrt{\frac{\rho}{m}}e^{i\theta}, \quad \mathbf{v} \equiv \frac{\hbar}{ma}\nabla\theta. \tag{4.7}$$

To generate the initial conditions for our simulations, we used a modified version of the initial conditions generator MUSIC (Hahn & Abel, 2013). We modify the matter power spectrum for the initial conditions using the redshift-independent transfer function provided

by Hu et al. (2000) as

$$P_{FDM}(k,z) = T_F^2(k) P_{CDM}(k,z), \quad T_F(k) = \frac{cosx^3}{1+x^8}, \tag{4.8}$$

where $x = 1.61 m_{22}^{1/18} k/k_{Jeq}$. Here $m_{22} = m_a/(10^{-22}\,\mathrm{eV})$ and k_{Jeq} is the fuzzy dark matter Jeans scale at matter-radiation equality, given as $k_{Jeq} = 9 m_{22}^{1/2} \mathrm{Mpc}^{-1}$. MUSIC returns a FDM density field with this modified initial power spectrum. By taking the divergence of the velocity field in Equation 4.7 and using mass conservation, we can show that the phase of the wave function θ is directly proportional to the gravitational potential Φ. We use this information and the FDM density returned by MUSIC to calculate the real and imaginary parts of the wave function ψ, to be used as the FDM initial conditions by ENZO.

For the hydro solver in our simulations, we use the energy-conserving, spatially third-order accurate Piecewise Parabolic Method (PPM). ENZO follows the non-equilibrium evolution of nine species (H, H^+, He, He^+, He^{++}, e^-, H_2, H_2^+, and H^-) and includes radiative processes.

We perform our cosmological simulation with a comoving box size of 1.7 h^{-1} Mpc with the fuzzy dark matter mass of 2.5×10^{-22} eV. We use a cosmology consistent with Planck Collaboration et al. (2020) ($\Omega_m = 0.315$, $\Omega_b = 0.0493$, $h = 0.674$, $n_s = 0.965$). Evolving the FDM wave function accurately using the wave perturbation theory requires that the proper scale of interest should be smaller than the de Broglie scale (Li et al., 2019). Not resolving the de Broglie scale results in incorrect structure evolution at small scales as well as very large scales in the box. This results in a much stringent requirement on the resolution for evolving the Schrödinger-Poisson equations. Therefore, we use a unigrid of 1024^3 for our simulation ensuring that the de Broglie scale is always resolved. This results in a cell size of 2.37 comoving kpc which corresponds to 0.215 proper kpc at $z = 10$. With the strict criterion for the resolution of the wave function, we cannot use a very large box given our computational constraints. Therefore, to have sufficient collapsed structure in our box, we

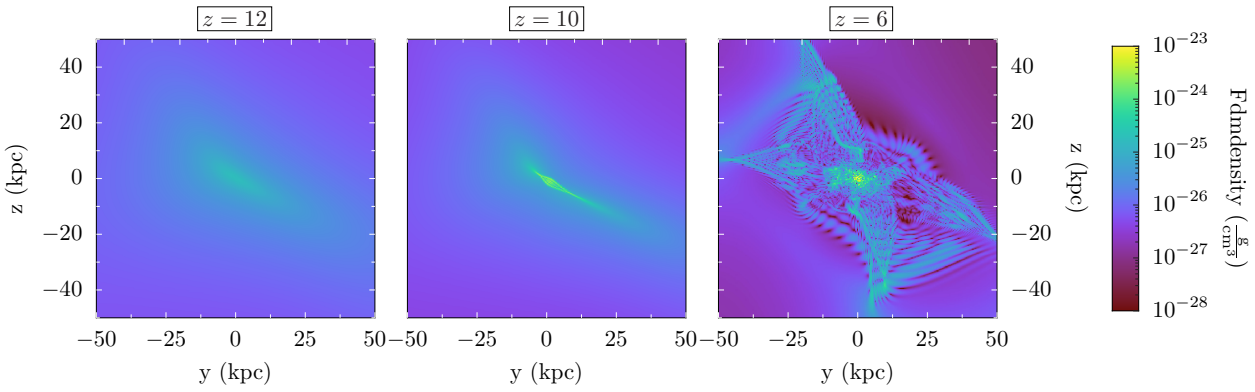

Figure 4.1: Slice plots of FDM density along the yz-plane passing through the densest point in the halo at redshift 12 (left), redshift 10 (center) and redshift 6 (right).

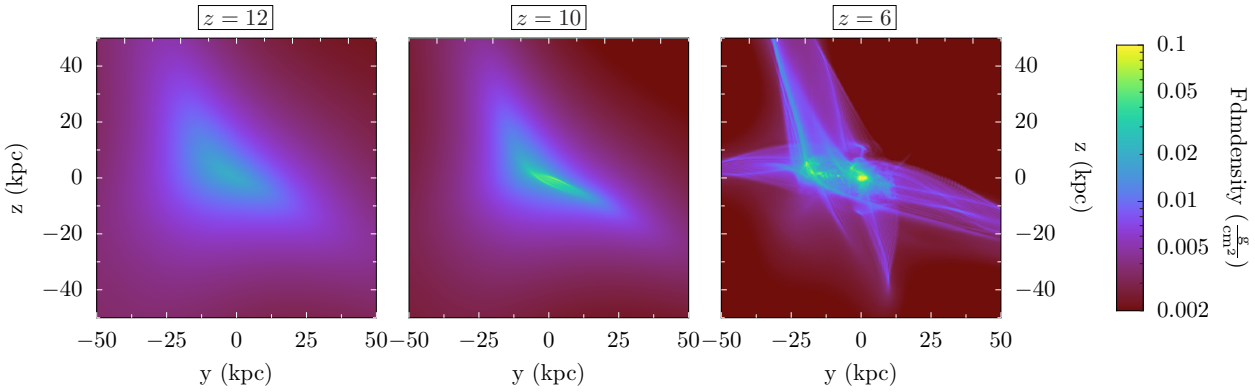

Figure 4.2: Projection plots of FDM density along the yz-plane passing through the densest point in the halo at redshift 12 (left), redshift 10 (center) and redshift 6 (right).

increase σ_8 to 1.4 from 0.811 given by Planck Collaboration et al. (2020). The choice of σ_8, box size, and axion mass is the same as one used by Mocz et al. (2019, 2020). In our simulation, we do not include the adaptive mesh refinement (AMR) for baryons here and we plan to include it in future work.

4.3 Results

4.3.1 Structure of the fuzzy dark matter halo

In our simulation, we followed the evolution of the densest halo region with redshift. We found that the dark matter distribution in the halo is smooth before redshift 10 and it starts to have more internal substructure after that. Figure 4.1 and 4.2 show the slices

and projections in the yz-plane of the fuzzy dark matter density passing through the center of the halo with the left, center, and right panels corresponding to redshifts of 12, 10, and 6 respectively. At redshift 12, the fuzzy dark matter distribution is very smooth. Near redshift 10, the fuzzy dark matter halo started to collapse further, whereas, at redshift 6, we find a completely collapsed massive halo with the characteristic interference pattern expected for the fuzzy dark matter. The projection plot of FDM density at $z = 6$ suggests a complex 3-dimensional structure. We define the virial radius as the radius that has the total average internal density 200 times the critical density at that redshift (r_{200c}). We define the enclosed total mass inside the virial radius to be the virial mass (M_{200c}). The virial mass and virial radius of the halo increase from $1.48 \times 10^9\,\mathrm{M}_\odot$ and 3.2 kpc respectively at $z = 10$ to $1.77 \times 10^{10}\,\mathrm{M}_\odot$ and 11.5 kpc respectively at $z = 6$. We note that at $z = 6$, the fuzzy dark matter structure is extended on much larger scales (up to radius of $30 - 50$ kpc) than the virial radius defined using overdensity, as can be seen from the Figure 4.1 and 4.2.

4.3.2 Gas properties

Similar to the evolution of the FDM density, the gas density also starts to increase near $z = 10$, becoming larger than $1\,\mathrm{cm}^{-3}$ for the first time. Figure 4.3 shows the evolution of gas density (top), gas temperature (middle), and H_2 fraction (bottom) going from $z = 12$ (left), $z = 10$ (center) to $z = 6$ (right). Each panel shows a slice along the yz-plane centered at the point with the highest gas density. At redshift 12 (left panels), the distribution of the gas density, temperature, and H_2 fraction is smooth, similar to the fuzzy dark matter distribution at $z = 12$, as shown in Figure 4.1 and 4.2. At $z = 12$, the gas number density is close to $0.01\,\mathrm{cm}^{-3}$, the gas temperature is $10 - 40$ K, with H_2 fraction being close to 5×10^{-6}. At $z = 10$ (center column panels) for the first time, the gas number density becomes larger than $1\,\mathrm{cm}^{-3}$. The top row center panel shows the dense gas along a filament. The temperature in these dense filaments ranges from 10^3 K - 10^4 K, with the H_2 fraction being close to 10^{-3}. This suggests that at $z = 10$ the gas is cooling via roto-vibrational transitions of H_2 resulting

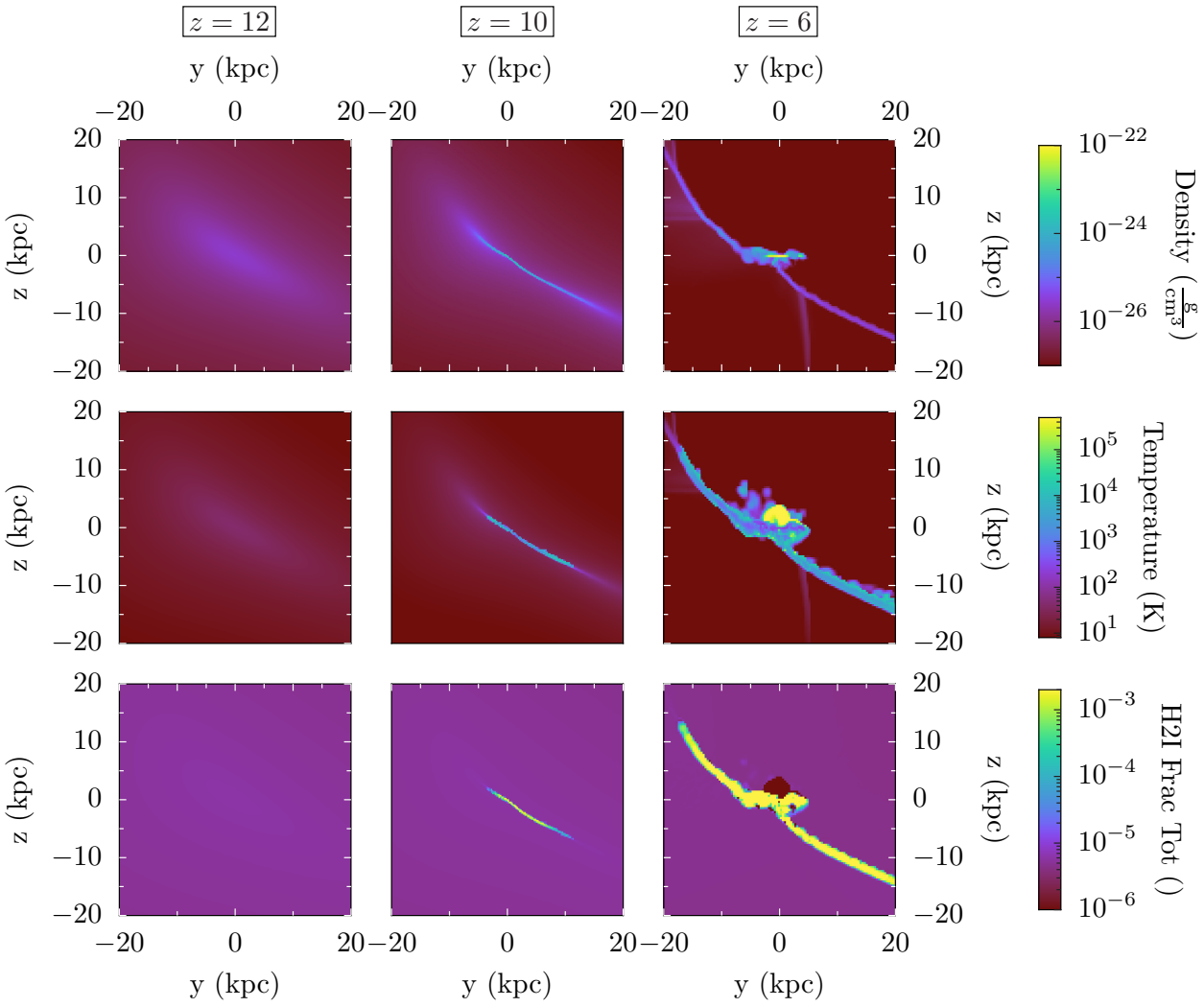

Figure 4.3: Slices in the yz-plane with gas density (top), gas temperature (middle), and H_2 fraction (bottom) at $z = 12$ (left), $z = 10$ (center), and $z = 6$ (right) respectively. The first star in our simulation forms in the dense region shown at $z = 10$ and subsequent star formation is expected to continue along the cold filamentary region and the central region at $z = 6$.

in higher gas densities. This is also the first time when we find a Jeans unstable cell (i.e. with its gas mass being larger than the Jeans mass), suggesting that the first stars in our simulation form very close to $z = 10$.

At $z = 6$ (right panels in Figure 4.3), the halo and the baryonic substructure in it have grown significantly. We find that the central gas number density is larger than $1000\,\mathrm{cm}^{-3}$ and the central dense region keeps accreting the gas through the filamentary structures. The central dense substructure extends to $\sim 5 - 8\,\mathrm{kpc}$ from the center. The temperature in the dense central and filamentary region ranges from $10^3\,\mathrm{K}$ to $10^4\,\mathrm{K}$, suggesting cooling from both molecular and atomic hydrogen. In the central region, we also find a large region shock-heated to a temperature of a few times $10^5\,\mathrm{K}$ which is similar to the virial temperature of the halo $5 \times 10^5\,\mathrm{K}$. This shock-heated region also dissociates and ionizes molecular and atomic hydrogen respectively, leading to H_2 fractions as low as 10^{-15} in the region. This shock-heated region first appears at $z = 7$ in our simulation.

As the central region of the halo starts to cool efficiently with molecular hydrogen, the gas density in the central region starts to increase and dominate over the fuzzy dark matter density. Figure 4.4 shows the density profiles for gas and fuzzy dark matter at z =12, 10, and 6. At $z = 12$, both the gas and fuzzy dark matter densities form a core in the center while maintaining the same baryon-to-dark-matter ratio throughout. At $z = 10$, when the gas cools to become dense and Jeans unstable for the first time, we find that in the central region, gas and dark matter densities match. After $z = 10$, the gas continues to cool efficiently using molecular hydrogen, resulting in a larger central region of the halo being dominated by the gas density. At $z = 6$, in the central $3\,\mathrm{kpc}$, the gas density is higher than the fuzzy dark matter density, which can also be seen in the dense regions from the right panels of Figure 4.3.

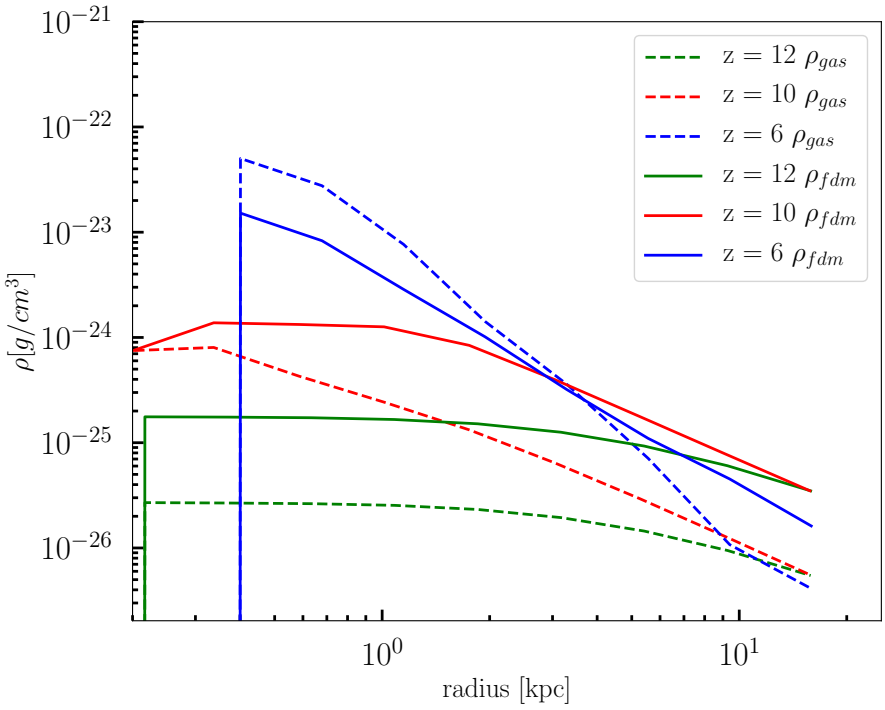

Figure 4.4: Density profiles for dark matter (solid) and gas (dashed) at redshifts 6, 10, and 12.

4.4 Discussion

4.4.1 Star-formation criterion

To accurately estimate the total stellar mass in Pop III stars, we would need to follow the evolution of the dense regions accurately, similarly to Kulkarni et al. (2019). With the adaptive mesh refinement, we can estimate the accretion rates onto proto-stars to infer their stellar masses and also the effect of feedback on the subsequent star-formation. Here, in the absence of AMR, we used a relatively simple criterion based on the Jeans instability to identify the star-forming regions in the halo.

We identified the regions that are Jeans unstable i.e. have their gas cell mass larger than the Jeans mass. At $z = 10$, only the densest cell is Jeans unstable. With time, more and more gas becomes Jeans unstable along the filaments connecting to the central dense region. Figure 4.5 shows a 3D rendition of the surface of the Jeans unstable region at $z = 6$. The colors represent the temperature of the gas, increasing from red to yellow. It suggests that the star-formation starts in the densest region of the halo at $z = 10$ and continues in the central region and the filaments connecting to the central region unless feedback stops it. To estimate the total stellar mass, we use a simple model parameterized as

$$M_* = f_* * M_{\rm gas} \tag{4.9}$$

where $M_{\rm gas}$ is the mass of the gas satisfying the Jeans instability criterion, f_* is the star-formation efficiency, which we assume to be 0.001 similar to the fiducial model used in Visbal et al. (2020), and M_* would be the stellar mass forming. Table 4.1 shows the virial radius, virial mass, total gas mass, gas mass in the Jeans unstable cells, and the gas mass in the densest cell in the center as a function of redshift. At redshift 6 and 7, the gas mass inside the halo dominates over the total FDM mass. In absence of any feedback effects, the total stellar mass can be estimated using the star formation efficiency. The gas mass in the densest

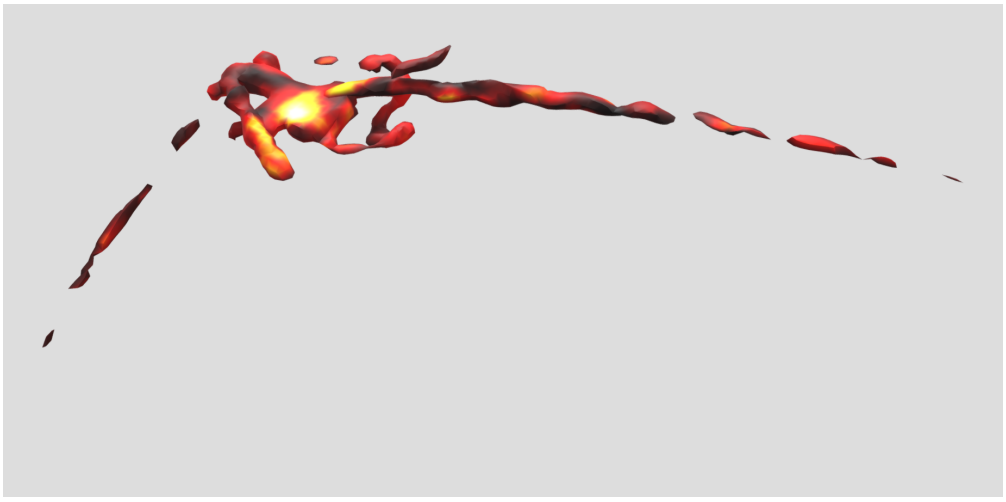

Figure 4.5: 3D rendition of the Jeans unstable gas at $z = 6$ shows that the Jeans unstable regions are in the center of the halo and along a filamentary structure. The color represents the temperature of the gas increasing from red ($T \sim 10^3$ K) to yellow ($T \sim 10^5$ K). The scale here extends to ~ 30 kpc.

cell increases from $7.63 \times 10^5\,M_\odot$ at $z = 10$ to $3.38 \times 10^9\,M_\odot$ at $z = 6$. The gas mass in the densest cell decreases at $z = 7$, which we believe is the result of the shock heating at $z = 7$ and its effects can be seen in the temperature, H_2 fraction slices at $z = 6$ in Figure 4.3.

4.4.2 Ionization feedback

The stars forming in the halo would also start emitting ionizing radiation which would suppress the further star formation. An accurate treatment of the ionization feedback would

z	$R_{\rm vir}$ [kpc]	$M_{\rm vir}[M_\odot]$	$M_{\rm gas}[M_\odot]$	Gas mass in the Jeans unstable cells $[M_\odot]$	Gas mass in the densest cell $[M_\odot]$
10	3.2	1.48×10^9	2.13×10^8	7.63×10^5	7.63×10^5
9	6.1	7.63×10^9	1.42×10^9	7.76×10^8	8.11×10^7
8	7.1	8.92×10^9	3.29×10^9	2.56×10^9	1.29×10^9
7	8.8	1.19×10^{10}	6.11×10^9	5.16×10^9	5.25×10^8
6	11.5	1.77×10^{10}	9.89×10^9	8.30×10^9	3.38×10^9

Table 4.1: The virial radius, virial mass of the halo, gas mass in the halo, and the gas mass in the Jeans unstable cells in the halo as a function of redshift. At $z <= 7$, the total gas mass dominates over the total FDM mass inside the halo and most of the gas mass in the halo is Jeans unstable.

require accretion rates onto various proto-stars forming at different times and the resulting stellar masses. In the absence of the adaptive mesh refinement, we could not follow the collapse of individual proto-stars to estimate their stellar masses and the ionizing radiation from them. Therefore, we use a very simple analytic prescription for it.

As shown in Table 4.1, a large chunk of the Jeans unstable gas mass in the halo remains in the densest cell in the center. We thus use the star cluster in the densest cell as the main source of ionizing radiation. We assume a star formation efficiency of 10^{-3} (Visbal et al., 2020). We consider two cases for ionizing feedback where the low feedback corresponds to 4000 ionizing photons per baryon and the high feedback corresponds to 65000 ionizing photons per baryon. These correspond to the feedback from Pop II stars and Pop III stars as used in Visbal et al. (2020). At each redshift, we calculate the radius of the bubble which would be ionized from the radiation from the central star cluster for the two feedback scenarios. We assume spherical symmetry and also ignore recombination, which would lower the size of the ionized bubbles. At $z = 10$, the size of ionized bubble corresponds to 0.25 kpc and 1.35 kpc for the low and high feedback cases. At redshift 9 and on-wards, the ionization bubble remains larger than the virial radius of the halo for the high feedback case. For the low feedback case, the size of the ionized bubble is 0.75 kpc at $z = 9$ and it becomes larger than the virial radius at lower redshift. At $z = 7$, our method suggests a much smaller ionized bubble of radius 0.65 kpc for the low feedback case. We believe that this is because of the lowered central density, but relatively large gas densities in the nearby cells because of the shock heating of the gas at $z = 7$, whose effects can also be seen in the temperature and density slices at $z = 6$ in Figure 4.3.

Therefore, based on the simple model to estimate the ionization feedback, most of the gas in the halo would be ionized by $z = 6$. In extreme cases, the ionizing radiation can heat up the gas in the filaments and unbind it, suppressing the star-formation along the filament. The gas in the filament is inflowing towards the central region with a velocity magnitude close to 100 km/s. This is larger than the typical thermal velocity of 30 km/s corresponding

to gas temperature $\sim 10^4$ K in the ionized region. Thus, the gas may still be able to infall along the filaments, leading to star-formation later. If we ignore any star formation in the filaments and only consider the central star cluster at $z = 6$, this galaxy would have a total stellar mass of $\sim 3.4 \times 10^6\,\mathrm{M}_\odot$ which can be detected with the *James Webb Space Telescope* (Zackrisson et al., 2011). However, constraining the mass of fuzzy dark matter based on the observability of the first galaxies would require further simulations with more accurate star-formation and feedback prescriptions with different FDM masses, and modeling to include the accurate abundances of these halos.

4.4.3 Comparison with previous works

There have been numerous numerical works studying various aspects of the fuzzy dark matter including the internal structure of halos (Schive et al., 2014a,b), Lyman-α forests (Li et al., 2019). There have also been a few works studying the formation of first stars in the fuzzy dark matter cosmology. Hirano et al. (2018) simulated the formation of first stars using the smooth particle hydrodynamics (SPH) code GADGET-2 and approximated FDM evolution using an N-body solver with modified initial conditions. They find multiple stars forming clouds in sheet-like or filamentary massive structures, but their work does not include the quantum pressure effects of the fuzzy dark matter.

Mocz et al. (2019, 2020) simulated the formation of first stars in a fuzzy dark matter cosmology using the moving-mesh code AREPO and evolved the FDM structures accurately by solving Schödinger-Poisson equations. Mocz et al. (2020) reported that they found first stars forming in filaments much before the virialized halos. In contrast, we found that the first star-forming region in our simulation is the densest region in the virialized halo in our simulation, although we did find star-formation continuing along a filamentary structure. In cosmological simulations using small boxes, the variances based on the different initial conditions result in vastly different outcomes in terms of geometry. Therefore, the geometric structures in our work cannot be assumed to be representative and require further investigation with different

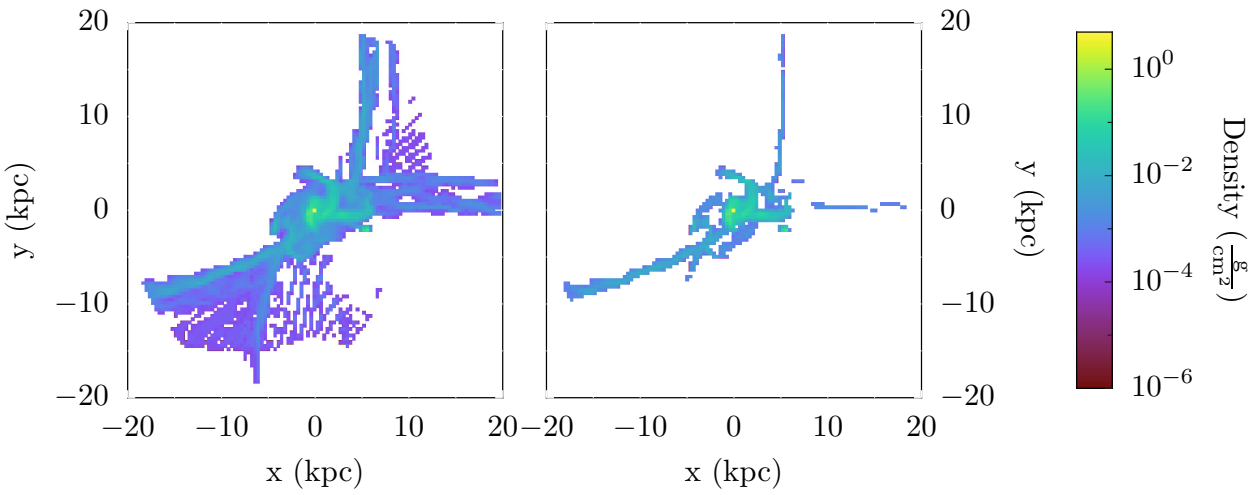

Figure 4.6: The left panel shows a projection the xy-plane of gas density for only those cells that satisfy the star-formation criterion in Mocz et al. (2019) ($n > 0.13\,\mathrm{cm}^{-3}$) at $z = 6$. The right panel shows a similar projection for the cells that satisfy the Jeans instability criterion for the same region. This suggests that the Jeans instability criterion for star-formation is stricter the one used in Mocz et al. (2019) and would result in star-formation happening in a smaller region.

initial conditions. We also note that the star-formation criterion used by Mocz et al. (2020) ($n > 0.13\,\mathrm{cm}^{-3}$) does not always satisfy the Jeans instability criterion. Figure 4.6 shows a projection of the gas density satisfying the star-formation criterion used in Mocz et al. (2020) (left) and a similar projection for the gas in the Jeans unstable region (right). This suggests that some of the low-density star-forming regions in Mocz et al. (2020) may not be Jeans unstable and may not lead to star formation. To accurately predict the locations of star-forming regions, we need to track the evolution of gas to a much higher density, which we leave for future work with the implementation of the adaptive mesh refinement (AMR) in ENZO.

4.5 Summary

The formation of the first stars and galaxies depends significantly on the nature of dark matter. Understanding how and when first stars and galaxies form in the fuzzy dark matter cosmology can be used to put very strong constraints on the mass of the ultra-light axion. In

this chapter, we performed high-resolution cosmological hydrodynamical simulations which evolve the fuzzy dark matter distribution accurately using the Schrödinger-Poisson equations using ENZO. In our simulation, we find the first stars forming in the central region of the collapsed halo of mass $1.4 \times 10^9\,\mathrm{M}_\odot$ at $z = 10$. With time, the star-forming region extends along a filamentary structure connecting the central dense region, extending up to $30-40\,\mathrm{kpc}$ in length at $z = 6$. To study the fragmentation processes in the clouds, and to estimate the final masses of the stars forming and their feedback effects, we need to follow the evolution of gas density using the adaptive mesh refinement (AMR) which we plan to do in the future work.

Conclusion

Population III (Pop III) stars remain a topic of great interest for their role in metal enrichment, reionization, and early galaxy formation, particularly today, given the possibility of their detection using upcoming observing facilities. Therefore, it is very important to explore the various possible formation mechanisms for the formation of Pop III stars and if they can improve their observability.

In Chapter 2, we used cosmological hydrodynamical simulations to provide the critical halo mass for the formation of Pop III stars and its dependence on the Lyman-Werner radiation, baryon-dark matter streaming velocity, and redshift. The critical halo mass connects the sites of Pop III star formation with the underlying dark matter halo distribution and is particularly important for the semi-analytic models to make observational predictions for the cosmological21-cm signal and the early galaxy formation.

In Chapter 3, we explored a possible formation scenario for massive Pop III clusters where the star-formation is suppressed by the presence of the ionizing radiation. These would be some of the most massive structures made up of Pop III stars forming at low redshift. We studied the fragmentation of gas in these systems to estimate the total mass in Pop III stars before star formation transitions to Pop II stars. We concluded that the detection of these Pop III galaxies would be unlikely in a blind field search with the *James Webb Space Telescope*.

In Chapter 4, we studied the formation of the first stars and galaxies in a fuzzy dark matter cosmology. The fuzzy dark matter has its small-scale power suppressed, thus Pop

III stars would form in much more massive halos at lower redshifts. This makes the first stars and galaxies an excellent way to constrain the properties of the fuzzy dark matter based on the observation of high redshift galaxies. We performed cosmological simulations to accurately evolve the fuzzy dark matter distribution and used simple prescriptions for star formation in it.

In the future, we plan to include the adaptive mesh refinement for the fuzzy dark matter simulations, which can be used to follow the gas collapse to a much higher density and accurately estimate the total stellar mass in these systems. Combined with the further simulations with different fuzzy dark matter particle masses and statistics of the fuzzy dark matter halos, we can put very strong constraints on the mass of the fuzzy dark matter.

We believe that the work in this thesis studying the effects of various processes delaying the formation of Pop III stars would be useful for the community. Building upon the results of the numerical simulations in this thesis and semi-analytic modeling, we will be better equipped to interpret the direct and indirect signatures of first stars with the upcoming observations.

References

Abel T., Bryan G. L., Norman M. L., 2002, Science, 295, 93

Agarwal B., Smith B., Glover S., Natarajan P., Khochfar S., 2016, MNRAS, 459, 4209

Ahn K., Shapiro P. R., Iliev I. T., Mellema G., Pen U.-L., 2009a, ApJ, 695, 1430

Ahn K., Shapiro P. R., Iliev I. T., Mellema G., Pen U.-L., 2009b, ApJ, 695, 1430

Alvarez M. A., Bromm V., Shapiro P. R., 2006, ApJ, 639, 621

Barkana R., Loeb A., 2001, Phys. Rep., 349, 125

Barkana R., Loeb A., 2005, ApJ, 626, 1

Behroozi P. S., Wechsler R. H., Wu H.-Y., 2013a, ApJ, 762, 109

Behroozi P. S., Wechsler R. H., Wu H.-Y., Busha M. T., Klypin A. A., Primack J. R., 2013b, ApJ, 763, 18

Bennett C. L., et al., 2013, ApJS, 208, 20

Bode P., Ostriker J. P., Turok N., 2001, ApJ, 556, 93

Boylan-Kolchin M., Bullock J. S., Kaplinghat M., 2011, MNRAS, 415, L40

Bromm V., Loeb A., 2003, Nature, 425, 812

Bromm V., Yoshida N., 2011, ARA&A, 49, 373

Bromm V., Coppi P. S., Larson R. B., 2002, ApJ, 564, 23

Bromm V., Yoshida N., Hernquist L., McKee C. F., 2009, Nature, 459, 49

Brooks A. M., Kuhlen M., Zolotov A., Hooper D., 2013, ApJ, 765, 22

Brummel-Smith C., et al., 2019, The Journal of Open Source Software, 4, 1636

Bryan G. L., et al., 2014, ApJS, 211, 19

Burkert A., 1995, ApJ, 447, L25

Chan T. K., Kereš D., Oñorbe J., Hopkins P. F., Muratov A. L., Faucher-Giguère C. A., Quataert E., 2015, MNRAS, 454, 2981

Chen K.-J., Heger A., Whalen D. J., Moriya T. J., Bromm V., Woosley S. E., 2017, MNRAS, 467, 4731

Clark P. C., Glover S. C. O., Smith R. J., Greif T. H., Klessen R. S., Bromm V., 2011, Science, 331, 1040

Corasaniti P. S., Agarwal S., Marsh D. J. E., Das S., 2017, Phys. Rev. D, 95, 083512

Del Popolo A., Lima J. A. S., Fabris J. C., Rodrigues D. C., 2014, J. Cosmology Astropart. Phys., 2014, 021

Dijkstra M., Haiman Z., Rees M. J., Weinberg D. H., 2004, ApJ, 601, 666

Dijkstra M., Haiman Z., Mesinger A., Wyithe J. S. B., 2008, MNRAS, 391, 1961

Dodelson S., 2003, Modern cosmology

Fialkov A., 2014, International Journal of Modern Physics D, 23, 1430017

Fialkov A., Barkana R., Visbal E., Tseliakhovich D., Hirata C. M., 2013, MNRAS, 432, 2909

Fialkov A., Barkana R., Pinhas A., Visbal E., 2014, MNRAS, 437, L36

Field G. B., 1958, Proceedings of the IRE, 46, 240

Franco J., Tenorio-Tagle G., Bodenheimer P., 1990, ApJ, 349, 126

Frebel A., Norris J. E., 2015, ARA&A, 53, 631

Glover S. C. O., 2015a, MNRAS, 451, 2082

Glover S. C. O., 2015b, MNRAS, 453, 2901

Gnedin N. Y., 2000, ApJ, 542, 535

Goerdt T., Moore B., Read J. I., Stadel J., Zemp M., 2006, MNRAS, 368, 1073

Greif T. H., 2015, Computational Astrophysics and Cosmology, 2, 3

Greif T. H., White S. D. M., Klessen R. S., Springel V., 2011a, ApJ, 736, 147

Greif T. H., Springel V., White S. D. M., Glover S. C. O., Clark P. C., Smith R. J., Klessen R. S., Bromm V., 2011b, ApJ, 737, 75

Greif T. H., Bromm V., Clark P. C., Glover S. C. O., Smith R. J., Klessen R. S., Yoshida N., Springel V., 2012, MNRAS, 424, 399

Haemmerlé L., Woods T. E., Klessen R. S., Heger A., Whalen D. J., 2018, MNRAS, 474, 2757

Hahn O., Abel T., 2013, MUSIC: MUlti-Scale Initial Conditions, Astrophysics Source Code Library (ascl:1311.011)

Haiman Z., Thoul A. A., Loeb A., 1996, ApJ, 464, 523

Haiman Z., Rees M. J., Loeb A., 1997, ApJ, 476, 458

Haiman Z., Abel T., Rees M. J., 2000, ApJ, 534, 11

Hartwig T., et al., 2018a, MNRAS, 478, 1795

Hartwig T., Bromm V., Loeb A., 2018b, MNRAS, 479, 2202

Hirano S., Hosokawa T., Yoshida N., Umeda H., Omukai K., Chiaki G., Yorke H. W., 2014, ApJ, 781, 60

Hirano S., Sullivan J. M., Bromm V., 2018, MNRAS, 473, L6

Hirata C. M., 2006, MNRAS, 367, 259

Hoeft M., Yepes G., Gottlöber S., Springel V., 2006, MNRAS, 371, 401

Hu W., Barkana R., Gruzinov A., 2000, Physical Review Letters, 85, 1158

Hui L., Ostriker J. P., Tremaine S., Witten E., 2017, Phys. Rev. D, 95, 043541

Iliev I. T., Shapiro P. R., Raga A. C., 2005, MNRAS, 361, 405

Inayoshi K., Visbal E., Haiman Z., 2020, ARA&A, 58, 27

Ishigaki M. N., Tominaga N., Kobayashi C., Nomoto K., 2018, ApJ, 857, 46

Jimenez R., Haiman Z., 2006, Nature, 440, 501

Joggerst C. C., Almgren A., Bell J., Heger A., Whalen D., Woosley S. E., 2010, ApJ, 709, 11

Johnson J. L., 2010, MNRAS, 404, 1425

Johnson J. L., Aykutalp A., 2018, arXiv e-prints, p. arXiv:1806.07901

Kinugawa T., Nakamura T., Nakano H., 2020, arXiv e-prints, p. arXiv:2009.06922

Kitayama T., Yoshida N., Susa H., Umemura M., 2004, ApJ, 613, 631

Klypin A., Kravtsov A. V., Valenzuela O., Prada F., 1999, ApJ, 522, 82

Krumholz M. R., McKee C. F., Klein R. I., 2004, ApJ, 611, 399

Kulkarni M., Visbal E., Bryan G. L., 2019, ApJ, 882, 178

Kulkarni M., Visbal E., Bryan G. L., 2020, arXiv e-prints, p. arXiv:2010.04169

Larson R. B., 1969, MNRAS, 145, 271

Latif M. A., Bovino S., Van Borm C., Grassi T., Schleicher D. R. G., Spaans M., 2014, MNRAS, 443, 1979

Li X., Hui L., Bryan G. L., 2019, Phys. Rev. D, 99, 063509

Liu B., Bromm V., 2020, arXiv e-prints, p. arXiv:2009.11447

Loeb A., Furlanetto S. R., 2013, The First Galaxies in the Universe

Machacek M. E., Bryan G. L., Abel T., 2001, ApJ, 548, 509

Madelung E., 1927, Zeitschrift fur Physik, 40, 322

Magg M., Hartwig T., Glover S. C. O., Klessen R. S., Whalen D. J., 2016, MNRAS, 462, 3591

Magg M., Hartwig T., Agarwal B., Frebel A., Glover S. C. O., Griffen B. F., Klessen R. S., 2018, MNRAS, 473, 5308

Maio U., Ciardi B., Dolag K., Tornatore L., Khochfar S., 2010, MNRAS, 407, 1003

Marsh D. J. E., 2016, Phys. Rep., 643, 1

McGreer I. D., Bryan G. L., 2008, ApJ, 685, 8

McQuinn M., O'Leary R. M., 2012, ApJ, 760, 3

Mocz P., et al., 2019, Phys. Rev. Lett., 123, 141301

Mocz P., et al., 2020, MNRAS, 494, 2027

Naoz S., Barkana R., Mesinger A., 2009, MNRAS, 399, 369

Navarro J. F., Frenk C. S., White S. D. M., 1997, ApJ, 490, 493

Ni Y., Wang M.-Y., Feng Y., Di Matteo T., 2019, MNRAS, 488, 5551

Noh Y., McQuinn M., 2014, MNRAS, 444, 503

Oñorbe J., Boylan-Kolchin M., Bullock J. S., Hopkins P. F., Kereš D., Faucher-Giguère C.-A., Quataert E., Murray N., 2015, MNRAS, 454, 2092

O'Leary R. M., McQuinn M., 2012, ApJ, 760, 4

O'Shea B. W., Norman M. L., 2006, ApJ, 648, 31

O'Shea B. W., Norman M. L., 2007, ApJ, 654, 66

Okamoto T., Gao L., Theuns T., 2008, MNRAS, 390, 920

Planck Collaboration et al., 2014, A&A, 571, A16

Planck Collaboration et al., 2020, A&A, 641, A6

Rahmati A., Pawlik A. P., Raicevic M., Schaye J., 2013, Mon. Not. Roy. Astron. Soc., 430, 2427

Regan J. A., Downes T. P., 2018a, MNRAS, 475, 4636

Regan J. A., Downes T. P., 2018b, MNRAS, 478, 5037

Rydberg C.-E., Zackrisson E., Lundqvist P., Scott P., 2013, MNRAS, 429, 3658

Safarzadeh M., Haiman Z., 2020, arXiv e-prints, p. arXiv:2009.09320

Scannapieco E., Schneider R., Ferrara A., 2003, ApJ, 589, 35

Schaerer D., 2002, A&A, 382, 28

Schauer A. T. P., Whalen D. J., Glover S. C. O., Klessen R. S., 2015, MNRAS, 454, 2441

Schauer A. T. P., et al., 2017, MNRAS, 467, 2288

Schauer A. T. P., Glover S. C. O., Klessen R. S., Ceverino D., 2019, MNRAS, 484, 3510

Schauer A. T. P., Glover S. C. O., Klessen R. S., Clark P., 2020, arXiv e-prints, p. arXiv:2008.05663

Schive H.-Y., Chiueh T., Broadhurst T., 2014a, Nature Physics, 10, 496

Schive H.-Y., Liao M.-H., Woo T.-P., Wong S.-K., Chiueh T., Broadhurst T., Hwang W. Y. P., 2014b, Phys. Rev. Lett., 113, 261302

Schneider R., Omukai K., Inoue A. K., Ferrara A., 2006, MNRAS, 369, 1437

Schneider A., Smith R. E., Reed D., 2013, MNRAS, 433, 1573

Shang C., Bryan G. L., Haiman Z., 2010, MNRAS, 402, 1249

Shapiro P. R., Giroux M. L., Babul A., 1994, ApJ, 427, 25

Shapiro P. R., Iliev I. T., Raga A. C., 2004, MNRAS, 348, 753

Sharda P., Federrath C., Krumholz M. R., 2020, MNRAS, 497, 336

Simon J. D., Geha M., 2007, ApJ, 670, 313

Skinner D., Wise J. H., 2020, MNRAS, 492, 4386

Smith B. D., Lang M., 2019, Journal of Open Source Software, 4, 1881

Smith B. D., Sigurdsson S., 2007, ApJ, 661, L5

Smith B. D., et al., 2017, MNRAS, 466, 2217

Sobacchi E., Mesinger A., 2013, MNRAS, 432, L51

Spergel D., et al., 2013, arXiv e-prints, p. arXiv:1305.5425

Stacy A., Greif T. H., Bromm V., 2010, MNRAS, 403, 45

Stacy A., Greif T. H., Bromm V., 2012, MNRAS, 422, 290

Sullivan J. M., Hirano S., Bromm V., 2018, MNRAS, 481, L69

Tegmark M., Silk J., Rees M. J., Blanchard A., Abel T., Palla F., 1997, ApJ, 474, 1

Thoul A. A., Weinberg D. H., 1996, ApJ, 465, 608

Tremaine S. D., 1976, ApJ, 203, 345

Trenti M., Stiavelli M., 2009, ApJ, 694, 879

Truelove J. K., Klein R. I., McKee C. F., Holliman II J. H., Howell L. H., Greenough J. A., 1997, ApJ, 489, L179

Tseliakhovich D., Hirata C., 2010, Phys. Rev. D, 82, 083520

Tumlinson J., Venkatesan A., Shull J. M., 2004, ApJ, 612, 602

Turk M. J., Smith B. D., Oishi J. S., Skory S., Skillman S. W., Abel T., Norman M. L., 2011, ApJS, 192, 9

Visbal E., Haiman Z., Bryan G. L., 2014a, MNRAS, 442, L100

Visbal E., Haiman Z., Terrazas B., Bryan G. L., Barkana R., 2014b, MNRAS, 445, 107

Visbal E., Haiman Z., Bryan G. L., 2015, MNRAS, 450, 2506

Visbal E., Haiman Z., Bryan G. L., 2016, MNRAS, 460, L59

Visbal E., Bryan G. L., Haiman Z., 2017, MNRAS, 469, 1456

Visbal E., Haiman Z., Bryan G. L., 2018, MNRAS, 475, 5246

Visbal E., Bryan G. L., Haiman Z., 2020, ApJ, 897, 95

Waters D., Di Matteo T., Feng Y., Wilkins S. M., Croft R. A. C., 2016, MNRAS, 463, 3520

Whalen D., Abel T., Norman M. L., 2004, ApJ, 610, 14

Whalen D. J., Fryer C. L., Holz D. E., Heger A., Woosley S. E., Stiavelli M., Even W., Frey L. H., 2013, ApJ, 762, L6

Windhorst R. A., et al., 2018, ApJS, 234, 41

Wise J. H., Abel T., 2007, ApJ, 671, 1559

Wolcott-Green J., Haiman Z., 2019, MNRAS, 484, 2467

Wolcott-Green J., Haiman Z., Bryan G. L., 2011, MNRAS, 418, 838

Wolcott-Green J., Haiman Z., Bryan G. L., 2017, MNRAS, 469, 3329

Wollenberg K. M. J., Glover S. C. O., Clark P. C., Klessen R. S., 2020, MNRAS, 494, 1871

Wouthuysen S. A., 1952, AJ, 57, 31

Yajima H., Khochfar S., 2017, MNRAS, 467, L51

Yoshida N., Abel T., Hernquist L., Sugiyama N., 2003, ApJ, 592, 645

Yue B., Ferrara A., Salvaterra R., Xu Y., Chen X., 2014, MNRAS, 440, 1263

Zackrisson E., Rydberg C.-E., Schaerer D., Östlin G., Tuli M., 2011, ApJ, 740, 13

de Souza R. S., Ishida E. E. O., Johnson J. L., Whalen D. J., Mesinger A., 2013, MNRAS, 436, 1555

de Souza R. S., Ishida E. E. O., Whalen D. J., Johnson J. L., Ferrara A., 2014, MNRAS, 442, 1640